Dielectric Networks from Solution-Processed 2D Nanomaterials

Yashaswi Nalawade
under the supervision of
Professor Jonathan Coleman

A thesis presented for the degree of
Doctor of Philosophy

School of Physics
Trinity College Dublin
Ireland
January 2022

Declaration

I declare that this thesis has not been submitted as an exercise for a degree at this or any other university and it is entirely my own work.
I agree to deposit this thesis in the University's open access institutional repository or allow the library to do so on my behalf, subject to Irish Copyright Legislation and Trinity College Library conditions of use and acknowledgement.
Elements of this work that have been carried out jointly with others or by collaborators have been duly acknowledged in the text wherever included.

Yashaswi Nalawade

Abstract

Shortly after the demonstration of the existence of free-standing graphene, the need for large scale production of two-dimensional nanomaterials was met by the emergence of a solution processing method called liquid phase exfoliation. The versatile and easily scalable nature of this technique made the manufacturing of various nanomaterials instantly more accessible. Furthermore, it wonderfully complimented the growing industry of printed electronics where flexible circuitry required that novel materials be discovered to support increasingly improving device architecture and performance. This synergy has led to numerous published reports where 2D nanomaterial inks are prepared through liquid-phase exfoliation and subsequently printed into devices using various deposition methods developed in parallel. The devices are generally heterostructures made up of stacked nanosheet networks. However, problems arise when attempting to insulate the conducting and semiconducting networks from each other and this is where dielectric films play an important role.

For the successful fabrication of stacked heterostructure devices, such as thin-film capacitors or thin-film transistors, it is vital that dielectric networks are uniform and pin-hole free to effectively insulate the various films that make up the device. Discontinuities in the dielectric film can lead to unwanted contacting and shorting of the overall device. Generally, dielectric networks are investigated by incorporating the material in question into a parallel-plate capacitor geometry and analysing its performance. To date, the majority of work on dielectric nanosheet networks has been with hexagonal boron-nitride, mainly due to its structural similarity to graphene, low toxicity and abundance. However, it presents several difficulties in that it suffers from a low dielectric constant and forms brittle, highly porous films making it challenging to fabricate an all-printed device. In this vein, we introduce bismuth oxychloride ($BiOCl$) as a new candidate for dielectric nanosheet films. We report the liquid phase exfoliation of $BiOCl$ into nanosheets for the first time through existing techniques and environmentally friendly solvents. Using aerosol-jet printing (AJP), we fabricate all-printed stacked capacitors of varying thicknesses and identify a minimum insulating thickness of $1.6\,\mu m$. With the help of impedance spectroscopy, we model our devices as a Randles circuit in order to extract capacitance values and ultimately the permittivity of the $BiOCl$ nanosheet networks. We obtain areal capacitances ranging from 40 to 110 $\mu F/m^2$ and a permittivity of $\epsilon_r = 41 \pm 3$, a significantly higher value than those previously reported for printed dielectric networks. Through breakdown voltage analysis, we deduce a dielectric breakdown strength of $0.67\,MV/cm$. Thus, we present a new dielectric layered material that is easily exfoliated and can be a good contender for insulating nanosheet networks in printed electronics.

Combining different substances to create a composite material has been widely used as a way of enhancing the properties of a system. In particular, conductor-insulator composites have been of interest in the past as a means of improving permittivity. Such

composites exhibit a colossal increase in permittivity near the percolation threshold of the conductive filler which is attributed to the formation of several microcapacitors within the system. Motivated by this, we aim to make composite films from 2D nanomaterial inks. While it was demonstrated that an all-printed heterostructure device was achieved through aerosol-jet printing of $BiOCl$ nanosheet ink to obtain a permittivity of 41, AJP is a recent development that involves a vast parameter space, thus lacking a full understanding of the deposition process. Considering the difficulty involved, it is prudent to continue to explore printed dielectric nanosheet networks via a more straightforward deposition method, such as spray coating. We therefore fabricate spray-coated parallel-plate capacitors using $BiOCl - Ag$ nanoplatelet composite inks of varying volume fractions of Ag nanoplatelets. A percolative behaviour was observed as the conductive filler was steadily increased from 0% to 40% with a percolation threshold measured at $\approx 18 vol\%$. This was accompanied by a two-fold increase in the permittivity that illustrated the formation of microcapacitors in the composite system. Although this is a relatively low increase compared to previous theoretical predictions, it can serve as a test-bed for future 2D nanomaterial conductor-insulator composites.

An ideal dielectric material is one that displays high electrical resistivity, large dielectric constant and a high dielectric breakdown strength. Unfortunately, instances have shown that the strong electric field created in high-κ dielectrics weakens the polar molecular bonds within the material, which reduces the enthalpy of activation required for dielectric breakdown. Furthermore, dielectric breakdown in thin films is difficult to measure since breakdown first occurs in localised "weak" regions of the film, making it challenging to discern the material's intrinsic breakdown strength. To adrress this, we present dielectric composites made from 2D nanomaterials. Having established that $BiOCl$ films exhibit significantly higher permittivity than previously reported 2D nanomaterial dielectric networks, we look towards hBN for its high breakdown strength. By forming a composite using $BiOCl$ and hBN, we aim to produce films that have both large permittivity, and high breakdown strength. The composite inks were deposited into films using a spray-coating method to form an array of capacitors with increasing volume fractions of $BiOCl$. Impedance spectroscopy was used to extract the permittivity of these composite capacitors. A linear increase in permittivity of the composite films was observed upon the addition of $50\, vol\%$ $BiOCl$ reaching a maximum value of 19. While dielectric breakdown measurements posed a logistical challenge, we were able to conclude with preliminary data that the breakdown strength of $BiOCl$ films was improved by the addition of hBN. The highly disordered nature of these films made it challenging to accurately characterise their electrical properties, nonetheless, a proof-of-concept was achieved.

Publications

1. Yashaswi Nalawade et al. "All-Printed Dielectric Capacitors from High-Permittivity, Liquid-Exfoliated BiOCl Nanosheets". In: ACS Applied Electronic Materials 2.10 (2020), pp. 3233–3241

2. Jose M. Munuera, Juan I. Paredes, Marina Enterria, Silvia Villar-Rodil, Adam G. Kelly, Yashaswi Nalawade, Jonathan N. Coleman, Teofilo Rojo, Nagore Ortiz-Vitoriano, Amelia Martinez-Alonso, Juan M. D. Tasco,"High Performance Na-O Batteries and Printed Microsupercapacitors Based on Water-Processable, Biomolecule-Assisted Anodic Graphene". In: ACS applied materials interfaces 2019 v.12 no.1, pp. 494-506

To Ma and Papa

Acknowledgements

I'd like to start off by thanking Johnny for giving me this opportunity - the transition from sitting in a lecture theatre listening to you draw parallels between graphene and the Pav to actually sitting with you at the Pav over warm cans of Dutch Gold discussing graphene, has been a seamless one. In all seriousness, the guidance and support I have received from you in the last four years has been irrefutable. Your ability to cultivate a culture of curiosity and discussion while also being approachable is extremely admirable and unique. Even down to the language you use while talking about science makes it refreshing and most importantly, accessible. There's no shortage of socially blundering physicists in the world so you really are doing God's work. I've learnt a lot from you in the last four years but the time has come, the metaphorical Sunday evening is here, and we all know that on Monday morning - the Trash goes out.

If there is one thing that can be said about me, it is that I make up for any lack in my scientific proficiency by freeloading off my fellow colleagues. It really is amazing how educational pints can be when you're surrounded by the right people. Adam - there's no playing down the impact you've had on me and my work. It'll take me a lot of unlearning to not reach for my phone to text you every time I have a question about physics or the opening times of Fibbers. Thank you for playing the role of teacher and friend so very effortlessly. Cian – dare I say anything nice about you at all? Despite your constant efforts to repel me, you've gone and made yourself a valuable friend. So get yourself something to bite down on while you read this next bit. Thank you for the constant unconditional and round-the-clock help and support. You're the carbon nanotube to my nanosheet network. I'd also like to thank the Colepeople who have seen me through these four years – Dave, Andrew, JB, Conor, Dan, Aideen, Sonia and Domhnall – I have stolen so much knowledge from you all.

Lastly, I want to express my gratitude for my family and friends. Mum and dad - you have somehow taught me to be both inquisitive and kind, to value knowledge and to respect people but above all, to truly believe that I can do anything. It's the greatest gift of all for it means that I'm not afraid to fail. To my brother Akarsh, shut ur face (thank you). To James, I am forever in disbelief that I bagged you. Your unbroken support by bringing equal measures of sense and silliness has been a constant source of strength for me. Thank you also for showing me that self-care during stressful times doesn't have to just be cups of tea and blankets, but is often best in the form of long jogs and breaking a sweat! Finally, to the rest of my close friends that are unfortunately scattered all around the world, thank you thank you thank you - in the wise words of Ilana Wexler "In da clerb, we all fam" (who am I if I don't quote Broadcity in my thesis).

Contents

Chapter 1

Introduction

In December 1959, the great American physicist Richard Feynman appealed for us to think smaller. In a talk titled "There's plenty of room at the bottom" [1], he effectively showed us where lies the new frontier of physics research. During a time when a computer filled an entire room, he had the audacity and foresight to ask "What would happen if we could arrange the atoms one by one the way we want them" – a future where we are able to manipulate and control things at the smallest of scales.

Half a century later, Feynman's musings have more than come to reality. As predicted, the advancement of imaging technology seen in the emergence of the Scanning Tunnelling Microscope and the Atomic Force Microscope in the 1980s propelled forward scientific research in the atomic scale. Thus grew the field of Nanoscience. Nanomaterials on the other hand, were already being used in ancient times. As early as 400 CE, the Lycurgus cup manufactured by Roman glasswork makes use of metallic nanoparticles that leads to a dichroism effect depending on how light is shone at it [2]. Dating further back to 1300-1400 BCE, nanomaterials were often used as colourants for glass making and ceramics in Egypt and Mesopotamia [3].

During the 20^{th} century, material science research on the nanoscale was peppered with reports on fullerenes and carbon nanotubes [4, 5]. However, the hallmark publication from Geim and Novosolov in 2004 definitively paved the way for a whole world of possibilities that led to rapid progress in the field of 2D materials [6]. A demonstration of that calibre was sure to be followed by a myriad of discoveries of new 2D nanomaterials. So understandably, the years following the discovery of free-standing graphene involved identifying and characterising the properties of the ever-growing family of 2D nanomaterials [7]. While there are methods of synthesis to produce pristine, high quality low dimensional materials, nanoscience research has become axiomatically accessible with the emergence of solution processing methods. It has allowed for flexibility in developing potential applications based on 2D materials. Among the solution processing methods, Liquid Phase Exfoliation (LPE) is a highly versatile and low-cost technique of producing nanomaterials. It presents the perfect gateway into exploring the full breadth of what nanoscience has to offer [8].

Modern technological advancement is innately associated with the improved performance of electronic circuits. In this way, printed electronics presents a promising avenue for developing smaller circuitry that is cheaper to produce and compatible with growing technologies such as the Internet of Things. The technique of manufacturing electronics using text/graphic printing allows for thin, lightweight, and flexible electronic products – a key piece in furthering our society's symbiotic relationship with technology. While

printed electronics was initially limited to organic polymers, the appearance of solution processed nanomaterials allows us to take a new direction. The family of nanomaterials encompass the electronic properties necessary for device fabrication, enabling us to revisit applications such as energy storage as well as active circuit elements such as transistors and sensors.

Many modern electronics devices can be viewed as heterostructures that are made up of stacked layers or films. Oftentimes this structure is some combination of conducting, semi-conducting and insulating films of materials. In order to fabricate a high performing device, we must ensure that the involved films are uniform and without defects. Understanding the morphology of such films, i.e. how the nanomaterials arrange themselves to form a network, and the corresponding electronic properties it exhibits is therefore non-trivial. With respect to printed electronics using solution processed nanomaterials, we aspire to produce continuous and thin, yet compact and mechanically robust films on flexible substrates. If successful, heterostructures made from nanomaterials can be achieved at high throughput and cheaper production to enable applications in memory, sensing and energy conversion devices.

While conducting and semiconducting networks of nanomaterials allow for charge transport within a device, dielectric films provide insulation between the circuit elements. Particularly as the move is made from planar to vertically stacked heterostructure devices, unwanted contacting between the different layers can lead to shorting. Moore's law predicts that the density of devices on integrated circuits doubles every two years [9], emphasising the need for effective insulation between circuit elements. In addition to this, the currently used dielectric films of SiO_2 fall short of this downward scaling of device architecture since its low permittivity (3.6) would require the films to be of the order of 1 nm to match gate lengths going down to $\approx 60\,nm$ in field-effect transistors [10]. Dielectric materials that exhibit higher permittivity would not only improve charge separation and insulation within circuits but would also allow for thicker films while still yielding a high capacitance. This would enable potential improvements in a whole host of devices such as thin-film capacitors, transistors, tunable electronic devices, energy storage and random-access memory devices.

The motivation of this thesis lies in exploring dielectrics in the realm of low-dimensional materials that can be used in printed electronics. Following the undeniable progress made in recent years on developing composite structures such as transistors, batteries and other energy storage devices, a parallel unveiling of new dielectric materials is necessary. Unfortunately, investigation with regards to dielectric nanomaterials has been quite limited, with a disproportionate number of reports on a single material – hexagonal boron nitride (hBN). The reason for this is obvious. Boron nitride is easily available and cost-effective to produce. Its low toxicity and reputation as graphene's insulating counterpart makes it a likely candidate for use in low-dimensional based devices. Rather ironically however, the high volume of reports on hBN also exposes its many apparent shortcomings. Films of hBN display low permittivity and often require thick films to form continuous networks. Fabricating an all-printed heterostructure with hBN films without the use of additives or binders can be quite challenging. With this in mind, we aim to introduce a new layered dielectric crystal, bismuth oxychloride ($BiOCl$). The exfoliation of $BiOCl$ to produce nanosheets and the subsequent analysis of its dielectric properties will be presented in Chapter 5. A relatively new method of deposition called aerosol-jet printing will be introduced to fabricate printed capacitors, an appropriate medium through which to evaluate the efficacy of dielectric films in insulating vertically

stacked heterostructures.

Since the genesis of material science itself, material researchers have been combining substances to enhance and control the properties of the resultant mixture. Emboldened by the "$1+1>2$" composite effect, we aim to look beyond a blanket "wonder material" and explore what combinations of materials could be used to improve the permittivity of dielectric films. In this respect, composites in the form of conducting particles embedded in an insulating matrix have shown tremendous promise in displaying permittivities that are orders of magnitude higher than that of the stand-alone insulating material. This enhancement can be attributed to the interfacial polarisation induced by the increased local electric field at the interface between the conductive and insulating phases. The evolution of such a composite with increasing amounts of conductive filler particles is neatly described by percolation theory, a tool that has already made several appearances in studying nanomaterial networks. Encouraged by this, in Chapter 6 we explore composite films made from $BiOCl$ nanosheets and silver nanoplatelets ($AgNP$) in a hope to mimic the spike in permittivity previously reported in other materials. A parallel-plate capacitor geometry is employed to investigate the dielectric properties of the composite films, this time using a well-established spray coating method to reduce the complexity of the study.

The ability of dielectric films to maintain charge separation within a device has knock-on effects for example, on charge carrier mobility and switching voltages in thin-film transistors. Although high-κ dielectrics effectively separate charge, a high permittivity in and of itself is not the sole requirement. Oftentimes, a high-κ material will undergo dielectric breakdown more easily when subjected to strong electric fields. An ideal dielectric material is one that displays large permittivity while also maintaining high dielectric breakdown strength. Furthermore, it must form mechanically robust films that are flexible and without defects. In an attempt to achieve this, we turn again towards composite materials. Chapter 7 will research the properties of $BiOCl$ and hBN composite networks in the hope to couple the former's high permittivity with the latter's high dielectric breakdown strength. The printed composite networks are investigated with the same parallel-plate capacitor protocol.

The analysis and characterisation of the printed dielectric networks presented in this work heavily rely on impedance spectroscopy. This is a tool we have seen fit to use recurringly for the investigation of network morphology through parallel-plate capacitor devices. The approach to the impedance spectroscopy measurements have themselves matured in the assembling of this body of work. In many ways, this thesis is as much about learning to use impedance spectroscopy to unravel the morphological properties of nanosheet networks as it is about improving their dielectric properties.

Chapter 2

Low Dimensional Nanomaterials

Layered crystals were in use for hundreds of years before they were properly structurally identified and characterised. The use of naturally occurring compounds for dyes and lubricants dates as far back as 400 C.E. showing that layered crystals were being exploited for their unique properties far before they reached mainstream science. Research into low dimensional materials was brewing in the mid–1970s [11] when carbon nanotubes were first found. They were later fully characterised in 1991 [12]. Meanwhile in the late 1980s and into the following decade, fullerenes and nanoparticles were also being intensely studied [13]. Add to this the isolation of graphene in 2004, and what followed was the emergence of several nanomaterials that were being synthesised from bulk crystals. The research that ensued made it clear that these nanomaterials display an almost exhaustive range of physical and chemical properties which allows for several applications ranging from electronics to energy storage and sensing.

The first instances of nanomaterial synthesis in the mid-19th century were from that of Thomas Webb with vermiculite and chemists such as Schafhaeutl, Brodie and Staudenmaier [14] on production of graphite intercalation compounds and graphite oxide. The confirmation of dimensionality and structure of these materials however was limited by the lack of proper instrumentation at the time. It was only around 1948, that Transition Electron Microscopy (TEM) was starting to be used to analyse and image possible single layer materials [14][15]. Interestingly, this early TEM characterisation consisting of intensity analysis and shadowing would not meet today's standards of imaging proof of a single layer of atoms. In the 1960s, several TMD crystals were cleaved to produce nanosheets that approached monolayer thickness [16]. This was shortly followed by the demonstration of two dimensional sheets of inorganic layered compounds [17]. By the 1980s, advances in imaging technology led to the development of the Scanning Tunnelling Microscope (STM) and the Atomic Force Microscope (AFM) making analysis of possible new nanomaterials more thorough. Fast forward to 2004 to the hallmark publication from Geim and Novosolov in which they mechanically cleaved graphite to form free standing single atom layers of graphene and demonstrated atomically thin devices. This work caused the revision of previous theoretical studies that raised concerns that monolayer graphite, or that any 2D material is thermodynamically unstable and could not physically exist [18][19][20]. Since then however, several two dimensional nanomaterials have come to the forefront of material science.

This chapter will detail the structure and properties of the nanomaterials that are used in this body of work. It will be followed by descriptions of methods of synthesis of 2D nanosheets, with an emphasis on a particular solution processing technique called Liquid Phase Exfoliation.

2.1 The 2D Material Family

Crystals that are layered consist of atoms that are covalently bonded in-plane but display weak van der Waal's bonding out of plane as shown in Figure 2.1A. This allows for the separation of the layers within the crystal to form planar sheets which can be micrometres wide but atomically thin. Thus, we can define 2D nanomaterials as materials where at least one dimension is of the order of 1 nm. Realistically, 2D nanomaterials are not atomically thin but often consist of flakes comprising < 10 stacked monolayers. Furthermore, 2D materials can be produced from means other than layered crystals through growth process or by cleaving various other bulk parent crystals.

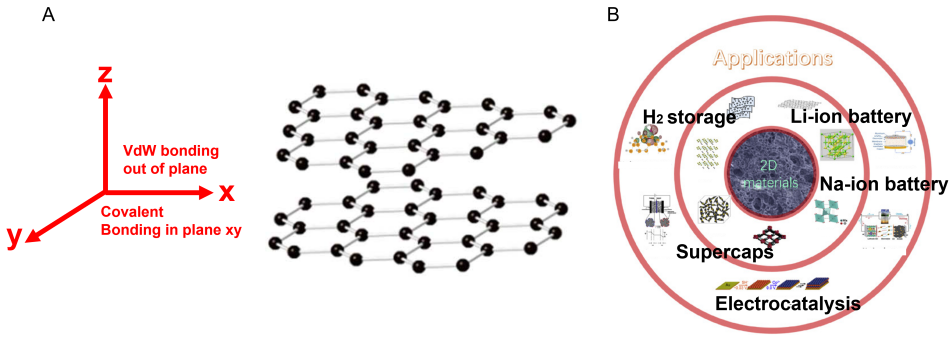

Figure 2.1: A: Bonding in-plane and out-of-plane in a layered bulk crystal of graphite [21]. B: A graphic depicting several potential applications of 2D materials [22].

The 2D material family is large as well as diverse. The introduction of graphene has led to a flurry of discoveries of other two-dimensional materials with varied properties and applications as depicted in Figure 2.1B. A group of compounds, some 40 strong called Transition Metal Dichalcogenides (TMD) [23–25] that consist of a transition metal and a group VI element have made up an important section of nanomaterials. Black phosphorous (BP), a puckered hexagonal allotrope of phosphorous has been demonstrated as a 2D material in transistors [26]. Hexagonal boron nitride (hBN) [23], the electrically insulating counterpart to graphite has shown promise in 2D material electronics as an electrical separator or an atomically thin insulator. MXenes or MAX phases are artificially produced layered ternary carbides and nitrides. These can be engineered through chemical functionalisation to be either metallic or small band-gap semiconductors [27] and are an attractive option for optoelectronics and thermoelectric power generation. Group III-VI materials such as indium selenide ($InSe, In_2Se_3$), gallium selenide and copper indium selenide have also recently emerged as potential 2D materials for optoelectronic applications [28–31].

1D materials also play an important role in the growing family of nanomaterials. For

example, carbon nanotubes are well known for their electrical and mechanical properties [12]. They have been comprehensively studied and show great potential for materials engineering. Their insulating counterpart, boron-nitride nanotubes albeit not as extensively studied [32] also show many desirable properties [33]. This work however deals mainly with 2D nanomaterials and their composites.

2.1.1 Conducting Layered Materials

Identifying new conducting layered materials is essential in the development of printed electronics. With graphene at its centre, the family of conducting layered materials is expanding and few other emerging metallic alternatives such as VS_2 and VSe_2 [34–36] and the 1T polymorphs of some TMDs such as MoS_2 [37–39] are being investigated. The most growth however is seen in the family of transition metal carbide and nitride ceramics - Mxenes [40, 41]. They display network conductivity values that are much higher than graphene and have shown potential in applications such as transparent electrodes and electromagnetic interference (EMI) shielding [42, 43]. Other options for conducting nanomaterials are single-crystal metal nanoparticles or nanoplatelets such as those made from cobalt, nickel, copper and silver [44, 45]. Graphene however still has the advantage of being easily synthesised and is therefore the focus of this work.

Graphene

Carbon has allotropes in one, two and three dimensions. Graphite consists of stacks of sheets of carbon atoms weakly bonded to each other via van der Waals forces. A single one of these sheets in which the carbon atoms are arranged in a honeycomb lattice is called graphene. Carbon nanotubes are achieved by rolling graphene along a given direction and reconnecting the carbon bonds. Fullerenes are molecules in which carbon atoms are arranged spherically and hence are considered to be zero dimensional objects. This is depicted in Figure 2.2A.

Two-dimensional graphite or graphene was investigated academically for over 60 years [46–48] and was used to describe the properties of carbon-based materials. Furthermore, theoretical studies showed graphene to be an excellent condensed matter analogue of (2+1) dimensional quantum electrodynamics [49–51]. The results from these studies however remained purely abstract as it was theorised that free standing 2D materials could not exist apart from a 3D base due to thermodynamic instability [18][19][20]. It was thought that the thermal fluctuations occurring within the crystal would be comparable to interatomic distances and that with the decrease in thickness, the atomically thin films would disintegrate. These notions however were precipitously disrupted when in 2004 Geim and Novosolov successfully demonstrated monocrystalline graphitic films that were stable under ambient conditions [6]. They were able to observe these monolayers with an ordinary optical microscope due to the subtle optical differences it creates on top of an SiO_2 substrate [6]. This was a major breakthrough as although graphene is relatively straightforward to synthesise, it is not easy to identify. It was isolated 400 years after its discovery, partly due to the absence of sophisticated imaging tools that could identify flakes that are one atom thick [52].

Each carbon atom in graphene is sp^2 hybridised and forms three σ bonds in the plane of the lattice, each of length 1.42 $\mathring{A}$. These extremely strong bonds are what makes graphene so mechanically robust in the basal plane, thus preventing crystal dislocations and defects. Perpendicular to this is a π electron cloud formed by the electron in the

p_z orbital. This unbound electron is free to move in the lattice and contributes to the extremely high carrier concentration n_c seen in graphene [53].

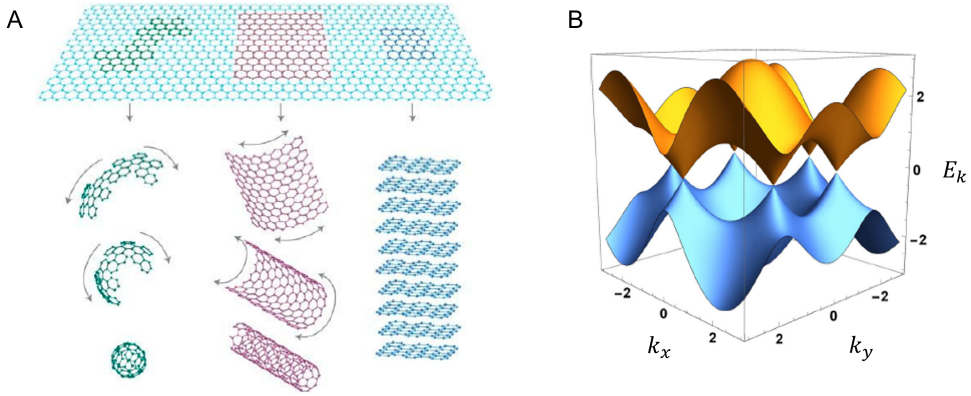

Figure 2.2: A: A visualisation of 0D, 1D and 2D allotropes of carbon being constructed from a sheet of graphite [54]. B: The dispersion relation in graphene π bands via the tight-bonding model considering only nearest neighbour hopping. E_k is energy and k_x and k_y are the x and y components of the wave-vector [55].

Graphene is considered to be a zero band-gap semiconductor or a zero overlap semimetal. The electronic band structure of graphene was first described by Wallace through a tight-bonding model [53] and is shown in Figure 2.2B. The electronic properties of graphene make it unique among other 2D electronic systems. The freely moving electron corresponds to the low energies close to the Fermi energy and as this electron can be in a spin-up or a spin-down state, the valence band is completely filled while the conduction band is completely empty. Furthermore, the periodic potential in the honeycomb lattice gives rise to degenerate levels in the valence and conduction bands of graphene. This means that that the valence and conduction bands touch without overlapping at the Dirac point of the Fermi energy making graphene a zero band-gap semiconductor. While the charge carriers in condensed matter physics are generally described by the Schrodinger equation as having an effective mass m^*, in graphene the charge carriers are considered to be mass-less Dirac fermions. This is due to the linear E- k relation in the vicinity of the Dirac point and leads to a very high carrier mobility $\mu_c > 15000\ cm^2/Vs$ [56]. Graphene exhibits high crystal quality which brings to attention yet another significant feature - the electrons while moving through the lattice can cover submicrometer distances without scattering, even in samples on atomically rough substrates and at room temperature.

The optical properties of graphene can be calculated from its electronic properties, showing that for visible light monolayer graphene is 97.7 $\%$ transparent. This combined with its high carrier mobility makes for great potential in device applications such as transparent conducting electrodes, ultracapacitors, field effect transistors and sensors [57, 58]. Graphene is also structurally flexible, allowing its electronic, optical and phonon properties to be modified by strain and deformation [59]. The reported mechanical and

thermal properties of graphene show high breaking strengths that reach the theoretical limit [60]. Record values for room temperature thermal conductivity [61] and Young's modulus [60] have been achieved. Graphene can be stretched elastically by as much as 20 $\%$ more than any other crystal [59, 60]. It has been nearly two decades since graphene was first produced and since then the progress has been rapid with several published articles investigating its remarkable properties and finding numerous wide-ranging applications. Having established its significance consistently through the years, the potential implications it could have on the future are indisputable.

2.1.2 Insulating Layered Materials

The group of insulating layered materials is quite limited with the focus historically being mostly on boron nitride [62–65]. Some natural minerals such as talc [66] and montmorrillonite [67] have shown potential as dielectrics used in printed electronics however, the reports are minimal. The two insulating materials that are the focus of this work will be described below.

Hexagonal Boron Nitride

Boron nitride (hBN) is widely used in industry as an ingredient in skin products, as a lubricant and thermoconductive filler due to its high thermal stability. It is an inorganic compound that exists in cubic, wurtzite and hexagonal lattices. Before the discovery of free standing hBN monolayers, single layers of BN were epitaxially deposited and studied on surfaces of transition group metals [68, 69]. A free standing hBN monolayer was first found in the mechanically milled residue of boron nitride in 2005 shortly after the rise of graphene [70]. However, it was Pacile et al. that first reported hBN nanosheets and Han et al. that produced double layer and monolayer hBN in 2008 [71]. The yields produced were quite low due to the limitations in production method nonetheless, since then several works have been published on large-scale production of hBN nanosheets via a wide range synthesis methods. Mechanical cleavage [72] and high energy electron beam irradiation [73] are some of the techniques used to produce two dimensional sheets of hBN.

Often times called "white graphene", boron nitride is similar to graphene in many ways. It has a hexagonal lattice as shown in Figure 2.3A and is made up of boron and nitrogen atoms arranged in the AAA stacking sequence with boron atoms directly above the nitrogen atoms. For comparison, in graphene the carbon atomic planes display Bernal stacking (AB). The properties of boron nitride however are quite distinct from graphene. There is significant charge transfer from boron to nitride atoms so the partially ionic $sp2$ hybridised B-N bonds display notably different properties from the C-C bonds in graphene for optics and electronic applications. Much the opposite to graphene, BN is white in colour and has a large band-gap of 5.5 eV as described in Figure 2.3B. It has a dielectric constant of 3-4 [63, 64, 76] and breakdown voltage between 1.9-2.5 MV/cm [77, 78]. Two-dimensional hBN has an atomically smooth surface with no dangling bonds or charge traps and is therefore a good candidate in electronic devices as a dielectric separator [79, 80]. It is often used in UV light emitters [81, 82] and as a thermoconductive filler in composites due to its exceptional thermal conductivity and stability.

Boron nitride nanotubes ($BNNT$), the 1D allotrope of hBN also have profound chemical and thermal stabilities [83]. The B and N atoms are superimposed in succession

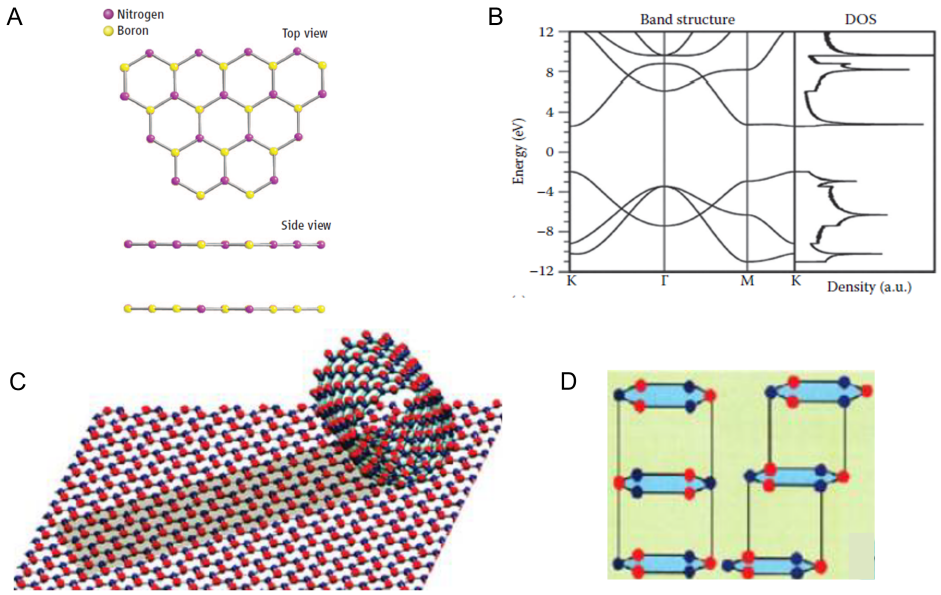

Figure 2.3: A: The top and side view of the chemical structure of hBN [21]. B: The band structure and density of states of hBN showing a band-gap of $\approx 6\ eV$. Here the x axis is shown in terms of crystal lattice points [74]. C: A depiction of a sheet of boron nitride and a boronnitride nanotube [75]. D: The stacking geometry seen in hexagonal and rhombohedral boron nitride nanotubes and nanosheets [75].

along a particular axis to form mostly multi-walled 1D structures [33] as shown in Figure 2.3C. Boron nitride nanotubes however are more challenging to prepare than CNTs since the B-N bonds are partially ionic in nature, whereas the C-C bonds are purely covalent [84–86]. This leads to lip-lip interactions between neighbouring BN layers. In a typical multi-walled nanotube, the sheet layers are ordered with an inter-layer distance of 0.33 - 0.34 nm. There are two main types of stacking in $BNNT$s as seen in Figure 2.3D - hexagonal and rhombohedral. $BNNT$s have been shown to be among the stiffest insulating fibres ever known [87]. This implies they could be valuable for reinforcement and/or used to increase thermal conductivity [62, 87, 88] of insulating polymeric films and fibres.

It is clear that boron nitride displays several desirable properties such as a wide band-gap, good thermal conductivity and non-toxicity. However, it has a low dielectric constant [63, 89] and hBN nanosheets have been shown to form brittle and highly porous networks. This poses a challenge to device fabrication through printed electronics and limits performance. For example, films of boron nitride in printed transistors would necessitate high gate voltages to modulate the transistor current given the low dielectric constant [64]. Hence there is a requirement for other dielectric materials to be explored.

Bismuth Oxychloride

Bismuth oxychloride comes in a white powder and is highly stable in air at room temperature, non-toxic and corrosion resistant. It is a member of V-VI-VII ternary layered compounds consisting of $[Bi_2O_2]^{2+}$ slabs interleaved with double chlorine atom slabs

as shown in Figure 2.4A. The crystal lattice dimensions within $BiOCl$ are $a = b = 3.91\,\mathring{A}; c = 7.4\,\mathring{A}$. The conduction band minimum and valence band maximum are located at the M and Γ points in the crystal's Brillouin zone respectively. This makes $BiOCl$ an indirect band-gap semiconductor as seen in Figure 2.4B, with a calculated band-gap of $2.65\,eV$ which is slightly lower than experimental results of $3.1 - 3.4\,eV$. The valence band of $BiOCl$ is fully occupied by $2p\ Cl$ and $2p\ O$ orbitals whereas the Bi $6p$ orbitals contribute to the empty conduction band. This unique atom-plane correlated band structure is the reason for the electric field between the $[Bi_2O_2]2+$ layer and the Cl atom layer that allows for efficient charge separation. There is a tendency toward cross-gap hybridisation between the cation-p states from the Bi atoms and anion-p states from the Cl atoms. This indicates a covalency in otherwise ionic materials, and results in a large Born effective charge and static dielectric constant. The large dielectric constant is favourable for effective screening of charged defects and high mobility [90]. These properties make $BiOCl$ an ideal candidate for electronics as a charge separator and dielectric material.

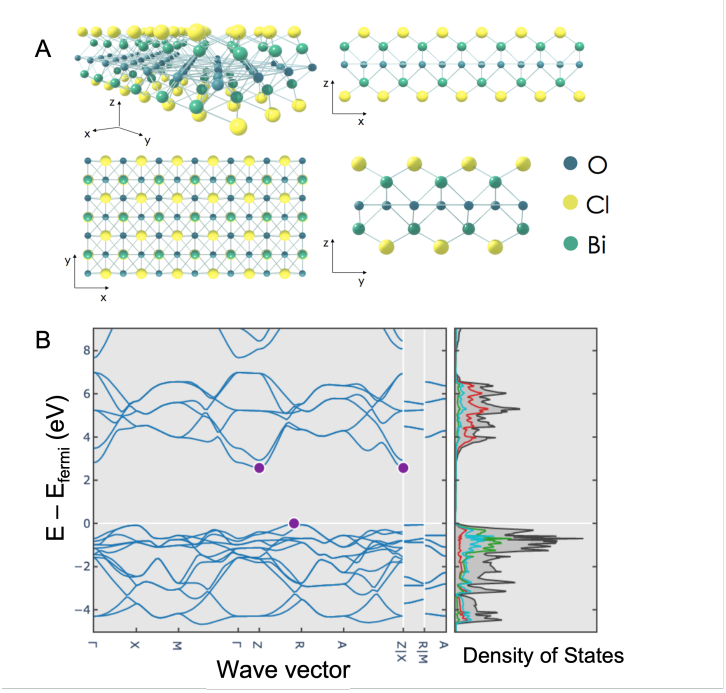

Figure 2.4: A: The chemical structure of $BiOCl$ showing halogen atoms between slabs of $[Bi_2O_2]2+$ from different directions. B: The band structure of $BiOCl$ showing a band-gap of $\approx 3\,eV$. Here the x-axis is the wave-vector at crystal lattice points in the first Brillouin zone.

Bismuth oxychloride ($BiOCl$) has been researched extensively mainly as a photocatalyst in pollutant degradation, water-splitting and waste-water purification [91–97]. It has been shown to have superior photocatalytic activity under UV irradiation, however it displays poor catalytic performance under visible light. It has the advantage of a wide band-gap which ensures high separation efficiency of photogenerated carriers and powerful oxidation abilities. In $BiOCl$, the internal static E-field generated between the B_2O_2 and halogen layer is thought to induce efficient separation in the charge carriers to allow good photocatalytic activity. It shows a deflourination rate constant of perfluorooctanoic acid (PFOA), a persistant organic pollutant, that is 14.6 and 1.7 times higher

than commercial TiO_2 and In_2O_3, respectively [91]. These properties, along with its ease of availability and non-toxicity, make $BiOCl$ a good candidate to be used in 2D nanomaterial based printed electronics.

2.2 Synthesis of 2D Materials

Two-dimensional materials are different to their bulk counterparts in that they have a high aspect ratio i.e. their surface area to volume ratio is large. This allows for more surface atoms to be exposed and hence they display different properties. In these low dimensional materials, the electrons are confined in one direction which produces changes in the electronic properties and thus modifies their electronic band structure. For example, graphene shows exceedingly high carrier mobility when compared with graphite [56]. The band-gap of semiconductor MoS_2 changes from 1.3 eV in bulk state to 1.9 eV in the monolayer state and has been shown to change monotonically with monolayer number [21]. Therefore, to explore the different properties of nanomaterials, several techniques have been developed to go from bulk powder to 2D nanosheets that will be discussed below.

2.2.1 Synthesis Techniques

In the mid-19th century, exfoliation of layered crystals with low reductive potential was performed by oxidation followed by dispersion in a suitable solvent [14]. Graphite upon being oxidised would lead to weakening of the bonds by addition of a hydroxyl group making it easier to delaminate. Recently however, more sophisticated and diverse techniques have been developed to synthesise nanomaterials. Low dimensional material synthesis can be broadly divided into two approaches. The bottom-up approach involves layers of atoms grown epitaxially. For example, chemical vapour deposition (CVD) as shown in Figure 2.5A involves molecules in the gas phase reacting with substrates and thereby building up thin films upon it. This method is widely used in semiconductor microfabrication. The other is the top-down approach (i.e. exfoliation), where bulk layered crystals are delaminated to give few-layer thick nanosheets. For example, in mechanical exfoliation atomically thin flakes are separated from their parent bulk crystal by rubbing the face of the crystal against a solid surface such as a silicon wafer or by cleaving with adhesive tape as shown in Figure 2.5B. The obvious advantage of this method is that the flakes are chemically unaltered and are of exceptionally high quality. However, their yield is low and the process cost is high. The trend between yield and production cost for various synthesis techniques is shown in Figure 2.5C. Low yields are a limiting factor for production of nanomaterials for application purposes where gram-scale quantities are sometimes needed.

This brings us to solution processed nanomaterials which consists of three main methods - ion intercalation, ion exchange and liquid phase exfoliation (LPE). These techniques usually involve dispersing a powder of the bulk crystal in a suitable liquid medium and then generating a force sufficient to exfoliate nanomaterials within the solution. Solution processing has several advantages. Firstly, liquid processing eliminates such complications as material transfer and demanding production conditions such as high temperature. Dispersion in a solvent allows for characterisation of the nanomaterials through spectroscopic methods.The nanosheets produced in solution can be sorted according to size and thickness, and can be easily chemically modified by the addition

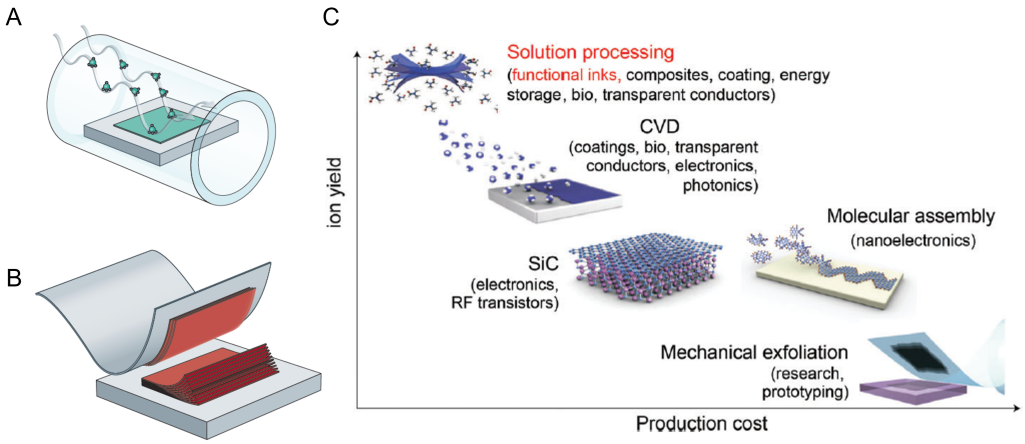

Figure 2.5: A: Nanomaterial synthesis by chemical vapour deposition [98]. B: Mechanical exfoliation depicted by the scotch tape method [98]. C: The production rates and costs compared for key synthesis methods along with applications for each [99].

of reagents. The formation of composite dispersions consisting of two or more nanomaterials becomes easier since they can be readily mixed. Finally, solution processing techniques also allow for the dispersions to be deposited into films and coatings, enabling the field of printed electronics. Emerging methods such as ion intercalation, shear exfoliation and ball milling will be briefly described below, followed by a detailed explanation of ultrasonication which is the technique used in this work.

Ion Intercalation and Ion Exchange

In this technique that dates back to Schaffautl et al. in the mid-19th centuary [102], the material is dispersed in a liquid medium and an ion species is introduced. As shown in Figure 2.6A, the ions intercalate the layers within the crystal and weaken the bonds as a result. Upon agitation these layers split apart forming nanosheets. Ion exchange exfoliation is applicable only to a limited few 2D materials that contain an interlayer of cations that can be exchanged. Intercalation often yields large flakes with a high percentage of monolayer flakes [103–107]. This process however has some disadvantages – it requires a harsh chemical environment and inert gas conditions. The synthesised nanosheets may come with unwanted functional groups, which modify the properties of the original material. They also often require post-processing which can cause defects and structural altercations.

High Shear Mixing

High shear mixing is a method of exfoliating bulk powder dispersed in a liquid medium through mechanical forces generated by rotating blades. Rotary blades apply shear forces causing the liquid to delaminate the layered crystals to produce nanosheets as depicted in Figure 2.6B. The shear mixer consists of a rotor and stator. The forces generated by

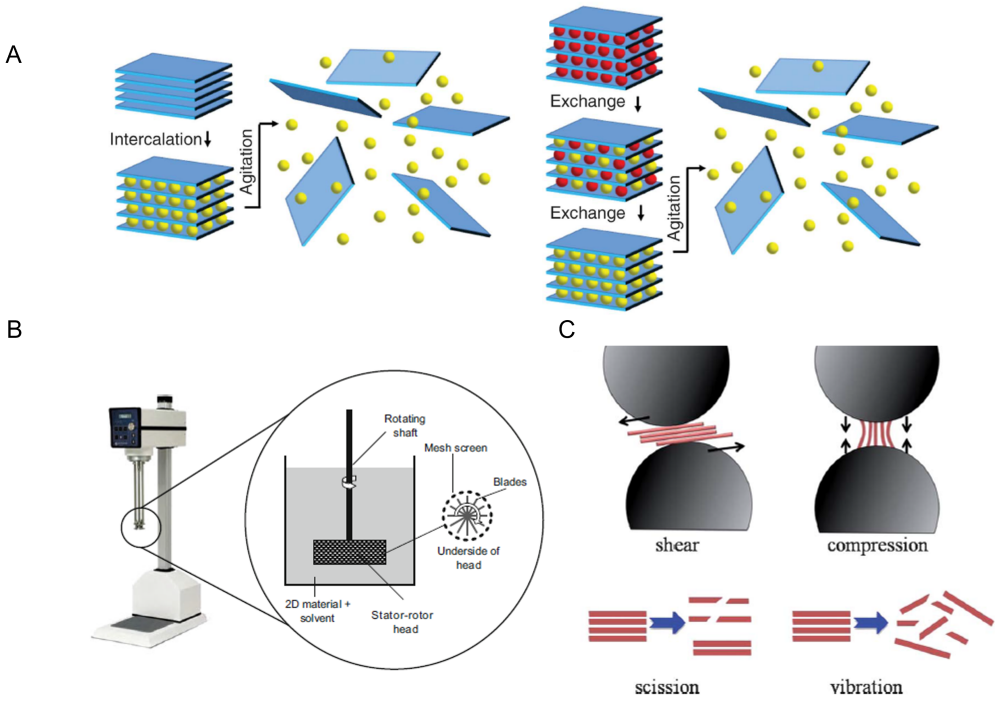

Figure 2.6: A: Mechanism of exfoliation by ion intercalation and ion exchange[21]. B: Exfoliation by high shear mixing using a stator-rotor head [100]. C: Mechanism of exfoliation during ball milling showing how the rotating balls exert shear and compression forces. Large forces can lead to fragmentation [101].

the rotating blades cause the weakly bound layers within the crystal to split apart, as long as the interaction between the liquid medium and layered material is energetically favourable. Most of the exfoliation occurs in the gap between the rotor and stator and in the holes in the stator suggesting a well-defined region of high shear rate. The blade diameter, liquid medium, shear rate all play a role in the quality of exfoliation. This is a highly scalable technology and is extensively used across a wide range of industries. The resultant nanosheets are usually thick, ranging from 10 nm to 100 nm. The clear advantage of this method is that large volumes of dispersed materials can be produced. In the case of graphene, up to hundreds of litres with a production rate of 1.44 g/hr [108] can be achieved.The downfall however is that the dispersion concentrations are low, < 0.1 mg/ml and the specifics of the scalability of this method are still unclear [109, 110].

Ball Milling

Ball milling is a method of grinding down particulate matter via shear and compression forces exerted by metal balls rotating in a hollow cylindrical shell. It has been used to produce mono- and few-layer graphene in 2010 [111]. During rotation the balls generate shear forces perpendicular to the walls of the cylinder impacting the material in question and grinding it down to a fine form. The forces generated by the balls on the powder are depicted in Figure 2.6C. There are planetary ball mills and stirred media mills [112–114], with the latter usually used to grind down powders to ultrafine particles. The nanostructure of the material can be controlled by varying the number and size of the

balls, the material out of which the balls are made up of and the material used for the surface of the cylinder. The rotational speed and choice of material itself also play an integral role in the quality and quantity of exfoliation. Since this is quite a violent process, the operation parameters need to be optimised to prevent fragmentation of the nanosheets or any defects introduced during milling [115]. Ball milling is a relatively new technique for production of nanomaterials but due to its intrinsic scalability, it can be very useful in industrial based applications. There are now several studies investigating the effect of ball milling process parameters on the exfoliation of graphene [116, 117] and the quality of the resulting nanosheets. However, little work has been done in ball milling of other layered crystals outside of graphene [101].

Ultrasonication

The concept of using sonication to produce graphene from graphite was derived directly from the research done in dispersing carbon nanotubes into solvents [8]. Through a combination of experimental data and thermodynamical modelling, Bergin et al. showed that carbon nanotubes are successfully dispersed in a solvent which has a surface energy close to that of the tubes. Since graphite has a similar surface energy to carbon nanotubes it was supposed by Coleman et al. that powdered graphite sonicated in the solvents established for carbon nanotubes could result in exfoliation. This paved the way for more materials to be exfoliated this way and eventually a general protocol was formulated for ultrasonication as a means to produce nanomaterials.

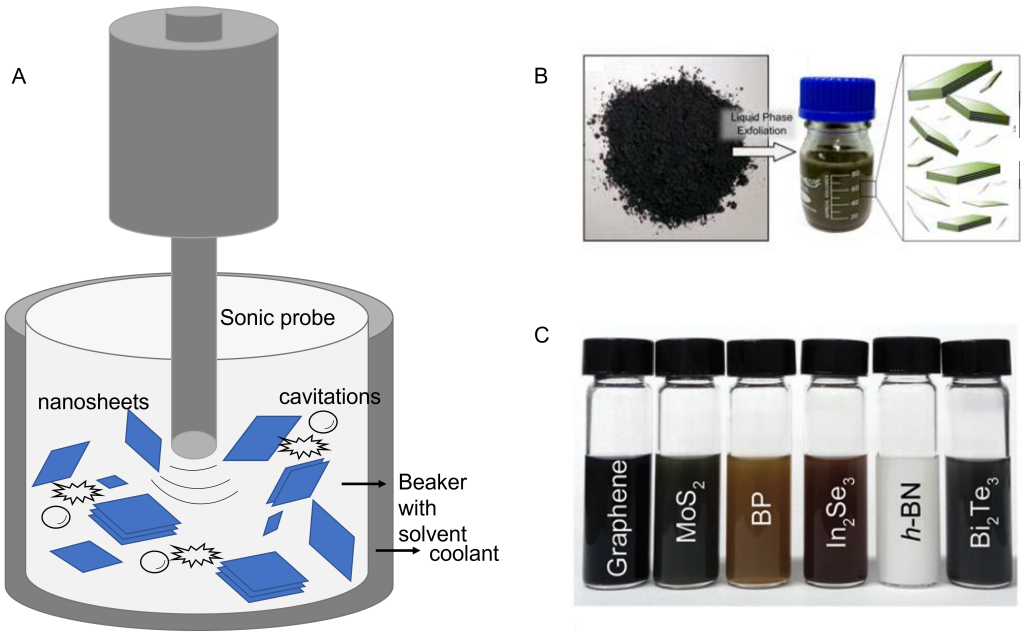

Figure 2.7: A: Graphical representation of exfoliation via ultrasonication. B: From powder to nanomaterial dispersion [118]. The formation of cavitations in the liquid medium is shown. C: An array of nanomaterial dispersions synthesised by ultrasonication [119].

Ultrasonication is a method of solution processing nanomaterials that involves generating shear forces by applying ultrasonic waves through the medium. This process is depicted in Figure 2.7A. The ultrasonic waves are propagated out of a probe that

is placed within the liquid. Rapid probe oscillation creates bubbles or "cavitations" within the volume of the liquid, which on bursting release large amounts of shear force that is sufficient to overcome the interlayer van der Waals attraction within the crystal. This method yields nanosheets of a wide range of sizes and layer numbers dispersed in volumes up to 100 ml. The concentrations of the resulting dispersions can vary from anywhere between 0.1 mg/ml to 1 mg/ml. In some cases it can be higher depending on the specific method of production [120]. The nanosheets are unfunctionalized unlike in ion-intercalation methods and are generally defect free. This approach for synthesising nanomaterials is fairly straightforward with very little variation between exfoliation protocols of different materials. The frequency and amplitude of the sonic waves generated affects exfoliation as ultrasonic LPE causes delamination as well as fragmentation of the nanosheets [121]. Moreover, the initial concentration of bulk powder and sonication time play a role in the outcome of exfoliation and quality of nanosheets. The shape of the vessel is also a contributing factor as the power from the sonic probe decreases both axially and radially, which limits the volume that can be exfoliated [118]. The choice of liquid medium is important as the delaminated sheets have to be stable in the dispersion to avoid reaggregation. As will be detailed in the following section, the liquid medium is selected by the matching of Hansen solubility parameters of the solute and solvent.

2.2.2 Stabilisation

It is necessary for the nanosheets formed in solution to be stable against reaggregation during exfoliation as well as after, particularly for application purposes. A well stabilised mixture can produce a high percentage of nanosheets that are monolayers and is one that does not undergo coagulation or reaggregation for long periods of time [122]. The time scale for which a dispersion needs to be stable depends on the device fabrication method. Stabilisers reduce the net energy cost of exfoliation by binding onto the nanosheet surface and preventing reaggregation. There are three main types of stabilisers – solvents, surfactants and polymers. The choice of stabilisers is made with the printing/deposition method and target application in mind. For example, use of surfactants and polymers although effective could potentially change the rheological properties of the dispersion. Furthermore, to remove them from a printed network they would require post processing methods which could damage or compromise the quality of the flakes. Solvents would then be the ideal candidate for developing application-based dispersions, however they too have advantages and disadvantages which will be discussed below.

Solvents, surfactants and polymers, each have slightly different mechanisms for stabilising colloidal mixtures. Solvents achieve stabilisation through minimising the total free energy of the system, which in turn depends on the enthalpy and entropy of mixing. Surfactants on the other hand, stabilise colloidal particles through forming an electrical double layer which is explained through DLVO theory. Here, the van der Waal attraction between the particles is counteracted by the electrostatic repulsion due to the electrical double layer. In the case of polymers, stabilisation is established through steric hindrance. The bulky polymer molecules take up space within the mixture and prevent aggregation. All three of these stabilisers have been used in 2D nanomaterial dispersions, depending on the target application. Below, these will be discussed in detail.

Solvents

Theoretical models designed to predict stability of small molecules in solution can be modified to account for low dimensional materials [8, 123]. In solution, small molecules and extended objects such as 2D materials interact via dispersive, dipole-dipole and dipole-induced dipole forces. However, it is the dispersive forces that are usually critical to understanding stability. First it is important to establish that the solubility of solids or any mixing of solids in a liquid medium is determined by the free energy of the system, ΔG_{mix}. This quantity represents the free energy difference between the mixture of the components and the two components in their unmixed states, as follows

$$\Delta G_{mix} = \Delta H_{mix} - T\Delta S_{mix}$$

Here, ΔH_{mix} is the enthalpy of mixing and ΔS_{mix} is the entropy of mixing carried out at temperature, T. The entropy of mixing is generally calculated statistically for a random mixture. For a successful mixing outcome, ΔG_{mix} must be negative. Small molecules often have a large entropy which implies mixing is generally allowed even for large ΔH_{mix} values. Large molecules however have a lower entropy which means if ΔH_{mix} is below a critical value, mixing is energetically favourable. One can then pick a solvent so as to minimise ΔH_{mix} and facilitate dissolution. This brings us to the Hildebrand-Scatchard equation [124–126] which can be used to approximate ΔH_{mix}

$$\frac{\Delta H_{mix}}{V_{mix}} = \phi(1-\phi)(\delta_{T,S} - \delta_{T,N})^2$$

where $\frac{\Delta H_{mix}}{V_{mix}}$ is the enthalpy of mixing per unit of volume being mixed, ϕ is the solute volume fraction and $\delta_{T,S}$ and $\delta_{T,N}$ are the Hildebrand solubility parameters of a given solvent (S) and solute (N). The Hildebrand parameter is a single parameter, δ that is made up of the Hansen solubility parameters which consist of three components as, $\delta^2 = \delta_d^2 + \delta_p^2 + \delta_h^2$ where δ_d^2 represents energy due to dispersion forces, δ_p^2 is energy from dipolar forces and δ_h^2 is from the hydrogen bonding between the molecules. The Hildebrand equation is minimised for values of $\delta_{T,S} \approx \delta_{T,N}$ i.e. if the solubility parameters of solvent and solute are close in value. This approach dates back to the 1930s and is a simple guide for choosing a solvent for a given solute. While it is common to use this equation empirically for polymers in solutions, the work of Coleman et al. outlines equations that are modified versions of the Hildebrand equation for extended objects i.e. rods and platelets in solution [123]. For dimensionalities of 1 and 2, the derived equation only differs to the original Hildebrand expression by a numerical constant.

Figure 2.8A shows data that compares the resulting concentration of nanosheets with the surface energy of the solvents used for its exfoliation [127]. As seen, the solvents deemed to be within the critical range of surface tensions (40 mN/m for graphene and WS_2) tend to be toxic with high boiling points [8, 21, 127, 128]. Solvents such as N-Methyl-2-Pyrrolidone (NMP), Dimethylformamide (DMF) and N-Cyclohexyl-2-pyrrolidone (CHP) are highly dangerous and have been shown to have teratogenic effects [129, 130]. In addition, the low volatility means that rapid device processing is challenging. An alternative to such solvents are low-boiling point and environmentally friendly substances such as IPA and ethanol but the surface tensions of these are too low 25 mN/m for exfoliation purposes and yield a low concentration of dispersed flakes.

The problem with using solubility parameters is that solubalisation of solutes in solvents is a result of several forces in play such as London dispersive forces, polar forces

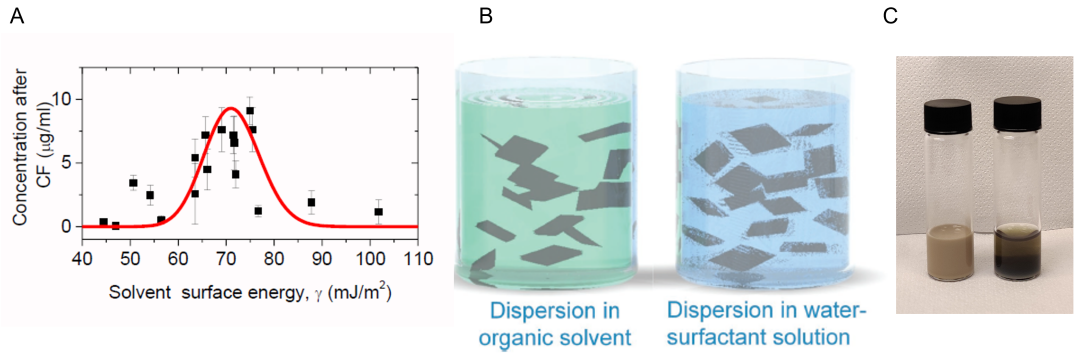

Figure 2.8: A: Concentration of graphene dispersion as a function of solvent surface tension from [127]. B: Stabilisation in organic solvent and stabilisation via formation of electrical double layer by surfactants [131]. C: Comparison of a stable well-dispersed silver nanoplatelet solution in water and a badly dispersed silver nanoplatelet dispersion where the nanomaterial has coagulated and sedimented to the bottom of the vial.

and dipole-dipole interactions. The work of Shen et al. shows that all contributions of solvent and solute need to be matched i.e. the total surface tension as well as the ratio of polar and dispersive forces of the nanomaterial and solvent must be matched [132]. Several strategies have been developed in an attempt to overcome these issues. Tuning the surface tension by changing the temperature or by adding salts has been shown to improve stabilisation in solvents as an alternative to toxic high boiling point solvents [21, 128, 132, 133]. The use of co-solvents to tailor rheological properties such as surface tension, viscosity and density of the resulting mixture has been attempted by adjusting relative concentrations of the substituent solvents [129, 134, 135]. However, it must be said that the yield of the resultant dispersions is still inferior to those exfoliated in high-boiling point solvents such as NMP and DMF which have the suitable solubility parameters. With regards to co-solvents, there are issues with the stability of water-alcohol mixtures [129, 134–137] as the surface tension of the mixture changes exponentially after addition of alcohols to water. The rheological properties of alcohol based co-solvents are also very sensitive to temperature changes.

An approach that was shown by Zhang et al. has been adopted by our group to get around this issue involves one of solvent exchange or solvent transfer. The exfoliation, since it is done under controlled conditions and with safety precautions, is carried out in the aforementioned high-boiling point solvents which have the appropriate surface tension values. After exfoliation, the resultant dispersion is centrifuged at high speed to separate out all the solvent and the sediment is redispersed in a low boiling point, less toxic solvent such as IPA or acetone. The idea is that there is still some of the initial solvent from the exfoliation adsorbed onto the surface of the nanosheets that keeps the sheets from aggregating in the poorly matched solvent that they are redispersed in [138].

Surfactants

Surfactants work as a stabilising agent by coating the nanomaterial in dispersion through collision and diffusion mechanisms. Surfactants can be ionic (anionic, cationic, zwitterionic) or non-ionic [139, 140]. Most effective ionic surfactants are facial amphiphiles i.e.

molecules with a quasi-flat molecular structure with hydrophobic and hydrophilic faces, for example bile salts such as sodium cholate (SC) or sodium deoxycholate (SDC). They are used in nanotechnology to stabilise nanomaterials in water. Typical non-ionic surfactants include Trition and the Tween and Brij series. Here we will focus on stabilisation through ionic surfactants.

Ionic surfactants consist of a head group that is polar and a tail group that is non-polar, usually an alkyl chain. The polar head group interacts with other ionic groups electrostatically whereas the tail group interacts with non-polar molecules via London forces. In solution at room temperature, the surfactant molecules dissociate i.e. they undergo ionisation. They are still in the vicinity of each other as they are attracted via electrostatic forces but are moved away from each other via Brownian motion. So when the surfactant molecules coat the nanosheet in question, the tail groups are bound to the surface of the sheet but the head groups float further away forming a diffuse cloud of ions. This is known as the electrical double layer. The nanosheets in this case have an effective negative charge Q_{eff}. This effect is not quantified through the amount of charge but through the potential at the edge of the bound tail group ions because of the electrical double layer. This potential is termed Zeta potential, $|\zeta|$. If $|\zeta| > 30\ mV$, the dispersion is considered to be stable against reaggregation [141, 142]. The physics of the double layer was described independently by Derjaguin $\&$ Landau and Verwey $\&$ Overbeek and therefore is known as DLVO theory. Broadly, it describes the attractive and repulsive forces experienced by nanomaterials in a dispersion – the attraction is described by van der Waal's forces and is dependent on nanomaterial size and the distance between them. The repulsive force is described by DLVO theory as being related to the zeta potential and inversely to the thickness of the layer of mobile counter ions, among other factors [143]. The total potential experienced by any nanomaterial in a dispersion stabilised via surfactants then, is the sum of these two forces.

Polymers

Polymers such as sodium carboxymethyl cellulose (CMC), Polyvinylpyrrolidone (PVP) and ethyl celluose are commonly used to stabilise nanomaterial dispersions against reaggregation [144–146]. The polymer chains adsorb onto the surface of the nanosheet at several sites forming loops that protrude into the solvent. The movement of the nanosheets are hindered as they approach each other in the liquid medium due to the space occupied by the long polymer chains. As a result, the number of chain conformations decline resulting in an increased free energy in the system [147] which acts as a repulsive force between the nanosheets, preventing coagulation or aggregation. In order for this to happen, the combination of the loop-tail entropy of the polymer and the energetics of adsorption of the polymer onto the surface of the nanosheet must result in a favourable free energy [148]. May et al. have analysed this balance of energies and developed a set of rules to predict successful nanosheet polymer-solvent combinations. Adding polymers allows formulation of composites [149] as well as control over the viscosity of the resulting dispersion, which can be beneficial while tailoring physical properties to suit the deposition methods.

Polymers however are lacking in some ways despite good stabilisation. For one, the resultant dispersions are still lower in final concentration and have fewer single layer sheets than those exfoliated in surfactants. This is due to bulky polymers being unable to easily insert themselves between partially exfoliated sheets. Polymers also sometimes

dope the nanosheets resulting in a change of properties of the material [150], although this can sometimes be beneficial [151]. In cases where this is undesirable, post processing is required to remove the polymers which often involves high temperatures or chemical intervention.

2.2.3 Sorting 2D Crystals

The nanosheets produced in dispersion after ultrasonication are extremely polydisperse and generally consist of sheets 100 nm – 1 μm in size and 1 to 10 monolayers in thickness [118]. The mean size distribution of the nanosheets differs according to the material being exfoliated and the specific process parameters. Therefore certain methods have been developed to isolate nanosheets of different sizes. Sorting the 2D nanosheets in the dispersion is an essential precursor to device fabrication as nanosheet size affects film morphology and hence its properties. There are broadly two methods of sorting liquid dispersed nanosheets – sedimentation based separation (SBS) and uniform or density gradient medium separation (DGM). The former is what is commonly used in this work to separate out nanosheets of different sizes. This technique exploits the centrifugal force generated when dispersions are spun at high speeds. The Svedberg equation [152] determines the sedimentation rate during centrifugation,

$$S = m(1 - \rho\nu)/f$$

where S, the sedimentation coefficient is the time needed for the nanomaterial to sediment $(1S = 10^{-13}s)$. The coefficient depends on morphological properties of the material. m and ρ are the mass and density of the nanomaterial being centrifuged and ν is the volume taken up by each gram of the nanomaterial. f is the frictional coefficient which depends on the nanosheet lateral size and thickness as well as the viscosity of the liquid medium it is dispersed in. Large or elongated nanoparticles experience more frictional drag than spherical ones and so have higher f values. According to the above equation then, it is clear to see that thick and large nanosheets which have a higher mass, sediment faster with respect to thin and small sheets which have a lower mass. Single layer nanosheets have very low sedimentation coefficient values and hence are difficult to isolate using SBS.

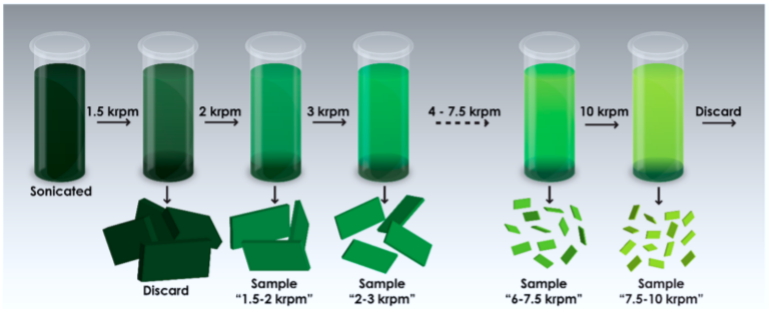

Figure 2.9: Size-selection by consecutive centrifugation steps. At each step, the nanomaterial sedimented is of smaller size and results in a less concentrated dispersion [122].

Liquid cascade centrifugation is a technique developed to isolate nanosheets of different sizes through incremental increases in centrifugation speeds. It is depicted in Figure 2.9. This procedure is termed as size selection and is a vital step after exfoliation.

We have established above that lower the frequency of rotation, larger the nanosheets that are dragged out of the dispersion and sedimented. The first step in size selecting nanosheets in dispersion is to spin at a low frequency, typically $\approx$ 250g. The sediment from this round consists of unexfoliated bulk material that can be discarded, or put through to another round of exfoliation if the bulk powder is valuable. The supernatant from this first round of centrifugation is spun at a slightly higher frequency, say 425g. The sediment from this run now consists of nanosheets of sizes trapped between frequencies 250g - 425g. The supernatant from this second run can be further centrifuged at a higher frequency, say 960g and the sediment collected will consist of nanosheets of sizes corresponding to frequencies 425g-960g. This can be continued until the supernatant is clear meaning that all material has been extracted from the dispersion.

The choice of stabiliser and size selection of nanosheets are non-trivial steps in developing a nanomaterial dispersion. The stabiliser affects properties such as viscosity and surface tension. The nanosheet size dictates how they will be arranged when deposited into a film. The chapter that follows will describe how to tailor nanosheet dispersions for optimisation in application purposes.

Chapter 3

Functional 2D Materials Inks

Historically the printing industry has used substances like soot, plant and earth additives as pigments and dyes for colour in graphic inks. This has allowed large-scale production of newspapers, magazines and packaging material at very low costs. With the advent of printed electronics, functional inks are being developed where these pigments are replaced by utile particles and deposited through well-established printing methods. This enables the inks to perform certain tasks, for example to conduct or insulate against electric current by using conducting, semi-conducting and insulating materials respectively. Some examples of active inks used in the past contain metallic particles [119] such as gold and copper. Organics [153] and carbon-based materials like carbon black and carbon nanotubes [154] were also widely used in applications such as biosensors, novel gas sensors and voltammetry [155, 156].

With the emergence of nanotechnology in the last 20 years, solution processed nanomaterials are being deposited and patterned onto substrates for functional device applications [131]. The commonly used printing or deposition methods used are screen printing [157–160], flexographic and gravure printing [161–164], spray coating [149, 165, 166] and digital deposition processes such as ink-jet [167, 168] and aerosol-jet printing [169–172]. The first instance of a printed transistor was reported in 2012 when graphene produced through liquid phase exfoliation was ink-jet printed to fabricate field-effect transistors [173]. Several other printable inks have since been formulated using reduced graphene oxide (rGO) [174–177], TMDs [77, 178], hexagonal boron nitride and black phosphorous [64, 179–181]. Each printing method requires the ink to have a specific set of rheological properties to produce a successful print. Thus, understanding ink rheology and ink drying mechanisms is non-trivial in the progress of functional device fabrication. This chapter will first detail principles of ink systems such as viscosity, surface tension and composition. This will be followed by a description of the two deposition methods used in this work i.e. spray coating and aerosol-jet printing.

3.1 Principles of Ink systems

The physical properties of an ink are dictated by its precise composition. In the case of functional inks the composition has to be carefully constructed, keeping in mind the method of deposition and the target application. For example, screen printing or flexographic and gravure printing requires a highly viscous and concentrated ink [153, 182, 183] whereas ink-jet printing and aerosol-jet printing require only low viscosity and dilute inks [169, 171, 184–187]. Additives and binders used in the ink need to be

compatible with the printing method but also not interfere with the properties of the ink or require rigorous post-processing. Furthermore, the substrate-ink affinity plays a major role in ink drying and film formation. After establishing some important rheological properties of inks, we will discuss ink spreading and drying mechanisms that ultimately affect morphology and hence performance of the functional films.

3.1.1 Ink Rheology

The deposition of inks often involves processes such as atomisation and fluid transfer, which require an understanding of the rheology of liquids i.e. how they behave under deformation and flow. Properties such as viscosity, density and surface tension of liquids must be well-defined and controllable. Viscosity is a fundamental characteristic property of all fluids that describes the measure of resistance to flow or shear. It is a function of pressure and temperature and is described mathematically as the ratio of shear stress, τ to shear rate $\dot{\gamma}$: $\tau = \eta\dot{\gamma}$ where η is the dynamic viscosity. This is represented graphically in Figure 3.1A. Based on this definition, liquids can be broadly divided into Newtonian and non-Newtonian liquids. When the viscosity of a liquid is constant and independent of the applied shear stress, it is a Newtonian liquid. In the case of non-Newtonian liquids, the viscosity changes with applied shear force and time. Among non-Newtonian liquids, there are pseudoplastic and dilatant behaviours. As seen in Figure 3.1B, pseudoplastic is a type of liquid that shows decreasing viscosity with increasing shear rate, whereas a dilatant liquid displays increasing viscosity with increasing shear rate. For nanoparticle ink systems, their behaviour can deviate from Newtonian flow due to the associated chemical bonds and physical interactions between the components.

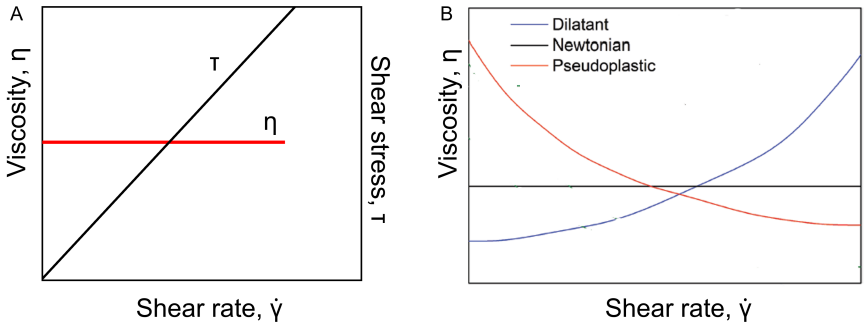

Figure 3.1: A: Flow and viscosity curves for a Newtonian liquid. B: Newtonian and non-Newtonian flow behaviours of functional inks [131].

Rheology of such inks is largely influenced by the nanoparticle volume fraction, ϕ as well as their shape and spatial arrangement [188]. The nanoparticles dispersed in a flowing liquid experience fluid-particle and/or particle-particle interactions which results in an increase in energy dissipation [189, 190]. These interactions increase with volume fraction, restricting particle diffusion to small clusters or "domains" formed by the nearest neighbours. This causes the viscosity, η to diverge according to the generalised Stokes relation [191]: $D = k_B T/6\phi\eta r$ which relates the diffusion coefficient, D of the particle to the viscosity, η of the fluid in which it is dispersed. Here, k_B, T and r are the Boltzmann constant ($k_B = 1.38 \times 10^{-23}\, JK^{-1}$), the absolute temperature (K) and the particle radius (m) respectively. In the case of 2D nanosheets with plate-like geometry,

the variation in viscosity is strongly affected by the high aspect ratio of such objects [192–196]. The increase in contact area and surface interaction between elongated and plate-like nanoparticles when compared to spherical nanoparticles at similar conditions of loading level and density, results in an increase in viscosity of the dispersion [197]. There have been several studies to determine viscosity values of fluids with dispersed nanomaterials [198–200], however they fall short of a precise theoretical model due to complexity of the system.

3.1.2 Ink Composition and Processing

We have established that developing nanomaterial inks for specific printing processes involves control over their rheological properties since they determine if the printing results are consistent and reproducible [201, 202] . An ink generally consists of a pigment, a solvent vehicle to carry the pigment and any necessary additives or binders to enhance the final ink properties. Typically, the basic role of a pigment is to give colour to an ink. In this context however, we talk of active pigments which possess functionality. Consider solution processed nanomaterials that have electrical properties that are conducting, semiconducting or dielectric [131, 203]. Rheology and surface tension modifiers in the form of additives and binders can be added to prevent aggregation and/or precipitation [201] of the nanomaterials. The vehicle that carries these components is usually in the form of a solvent and is responsible for the viscosity, surface tension and ultimately drying characteristics of the ink.

The compounds commonly used as binders are polymers, such as acrylics, cellulose and rubber resins [204–206]. Their function is to bind the pigment particles to each other and to facilitate adhesion to substrates. Upon deposition, binders can dry and solidify in the film or if necessary be removed by post-processing methods such as annealing or exposure to UV radiation. In addition, the choice of binder can impart specific properties to the film such as adhesion or resistance to certain ambient conditions [207–209], for example using water insoluble polymers to protect films from moisture [119]. Additives are substances that are included in the ink system to tailor the properties of the dispersion. They can be used to improve the wetting properties of either the pigment or the substrate. For example, surfactants are typically added to reduce the surface tension of water-based inks. Defoamers may be used to avoid bubble formation during the deposition process. They can also be used to alter the chemical properties of the ink for example, addition of alkalis results in a mildly basic pH making it easier to dissolve polymeric binders. The common formulation rule is that additives are supplemented in amounts not exceeding 5 wt$\%$ of the ink [210] to avoid it affecting the final network properties.

Solvents are the instrument through which pigments, binders and additives are carried. Its primary function is to provide a liquid medium so that the components within it can be transferred to a substrate via a printing method. Generally, an ideal solvent is one that dissolves most chemicals. Water comes closest to this as it dissolves more substances than any other solvent. A good solvent choice while preparing solution processed 2D material inks however, abides by the solubility parameter matching detailed in the previous chapter. Matching of Hildebrand solubility parameters ensures a well dispersed ink of nanosheets. The solvent of choice must not dissolve or degrade the dispersed material. It must evaporate at a rate compatible with the printing method and deliver the required ink viscosity. Typical solvents used in 2D material inks include

water, other polar solvents such as alcohols and ethers and organic solvents. The solvent is selected conidering the deposition method, the substrates, drying conditions and the product destination. For example, gravure and flexographic printing require that the ink drying is prompt [211, 212]. Common solvents for this type of printing are IPA and ethyl acetate which have high evaporation rates. Screen printing on the other hand requires less volatile solvents such as butoxyethanol to avoid clogging of the screen mesh associated with fast drying [213]. However, the choice of solvent for each deposition method is not always straightforward as there are several factors in play. It will be later discussed how morphology and therefore functionality of the film are also affected by the choice of solvent.

3.1.3 Ink spreading and Drying

In addition to ink processing, it is important to understand surface properties of the substrate since it is the inter-play between the two that decides the quality of the resulting printed pattern. The key properties of substrates to consider for a good print are substrate porosity and surface free energy. Structural and dimensional considerations include thickness, smoothness and flexibility. It is also important that the substrate is durable. Other factors like optical transparency and resistance to moisture can be taken into account depending on how relevant it is to the target application.

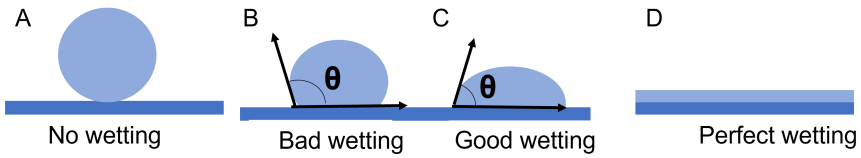

Figure 3.2: A schematic showing different substrate wetting conditions with respect to contact angle, θ. A: The case where the surface tension of the liquid is higher than the surface free energy of the substrate leading to beading and no wetting. B: The case of poor wetting where $\theta > 90°$. C: The case of good wetting where $\theta < 90°$. D: The case of perfect wetting corresponding to $\theta = 0°$.

The porosity of the substrate determines the absorption of the ink or paste. For example, absorption will be higher in the case of uncoated paper compared to plastic due to higher porosity. On absorbent substrates, adhesion is influenced by the degree of ink penetration. The pigment remains on the surface while the solvent is drawn into the substrate. If too much solvent is absorbed it could leave the pigment dry and unbound causing poor adhesion. On non-absorbent substrates, adhesion is primarily controlled by the film coating ability of the solvent and molecular affinity of the substrate. This is where surface energies need to be considered. Surface tension can be defined as the attractive force of the molecules present at the surface of a liquid towards each other. Surface free energy, albeit used interchangeably with surface tension, is the equivalent attractive force present between the molecules at the surface of a solid substance. Thus, for ideal wettability, the surface tension of the ink must be lower than the surface energy of the substrate. The surface tension of inks is decided by its composition i.e. solvent,

pigment or any binders and additives present. Polar inks have a higher surface tension than non-polar inks [214, 215]. For example, water has a higher surface tension than IPA. The surface free energy of substrates can be defined based on measurements of the contact angle obtained for different liquids according to Young's equation:

$$\gamma_{i-v} \cos\theta = \gamma_{s-v} - \gamma_{s-i}$$

Where γ_{i-v}, γ_{s-v} and γ_{s-i} represent the respective interfacial tensions between the solid surface (s), the ink (i) and the vapour (v) and θ is the contact angle as depicted in Figure 3.2. The correct blend of solvents can influence adhesion by creating better wetting of substrate and flow out. Contact angle values, $\theta > 90°$ suggests no or poor wetting whereas, $\theta < 90°$ suggests good wetting. A contact angle of $\theta = 0°$ represents perfect wetting and spreading. Good wetting is achieved in the case where $\gamma_{i-v} < \gamma_{s-v}$. This suggests that substrates with low surface energies are difficult to wet. In such cases, the ink cannot remain in contact with the surface and tends to retract and form beads leading to a discontinuous film. Generally, good wetting is seen when the surface tension of the ink is 7 -10 mNm^{-1} lower than the surface energy of the substrate [216]. This would mean for functional printing on substrates commonly used in electronics and optoelectronics such as Si/SiO_2, glass and plastics such as polyethylene terephthalate (PET), the surface tension of the inks must be sufficiently low (eg. $< 30\, mNm^{-1}$) [181, 217, 218].

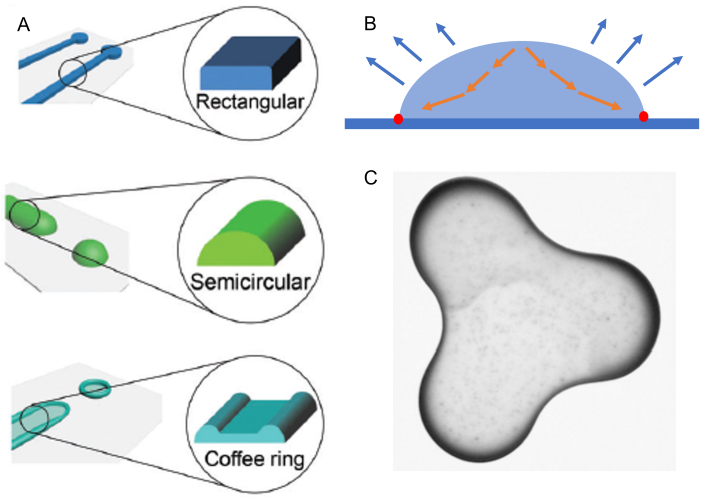

Figure 3.3: A: Different drying profiles of printed lines with highly viscous inks resulting in a rectangular cross-section and low viscosity inks leading to the coffee ring effect [119]. B: A schematic showing the mechanism of droplet drying with the blue arrows representing solvent evaporation at the surface and the red arrows representing material flow within the droplet.C: A photograph of a droplet of coffee containing 1 wt% solids dried to form the ring effect [219].

Considering reliable ink spreading, the morphology of the printed pattern is further influenced by the ink viscosity as shown in Figure 3.3A. High viscosity inks like those used in gravure and flexographic inks contain a high concentration of pigments and binders. These types of inks tend to form lines that have a rectangular shaped cross section when deposited. This is representative of a uniform distribution of material and follows that

the resulting film will show desirable properties such as high conductivity and mobility of charge carriers through the film. The ideal cross-section of a medium viscosity ink such as those used in ink-jet or aerosol-jet printing is semi-circular in shape. This pattern is due to low solid content for example, the amount of binder or pigment in the ink [220]. A common unwanted feature seen in medium and low viscosity ink deposition is the "coffee-ring" effect [219]. This is a highly non-uniform deposition result where most of the material dries to be concentrated on the periphery of the print, leaving a concave central area. This effect was explained by Deegan et al. and is related to non-uniform solvent evaporation across the droplet during ink drying. As shown in Figure 3.3B the evaporation rate is usually highest at the edge of the droplet-substrate interface i.e. at the contact line. This is due to the high surface area to volume ratio at that point. During drying, the contact lines pin the droplet to the substrate such that an outward convection flow is induced from the droplet centre to its edges, moving material as it does so. This is depicted in Figure 3.3C and is a process that is largely dependent on the drying conditions and surrounding environment [221].

3.2 Printing Technologies

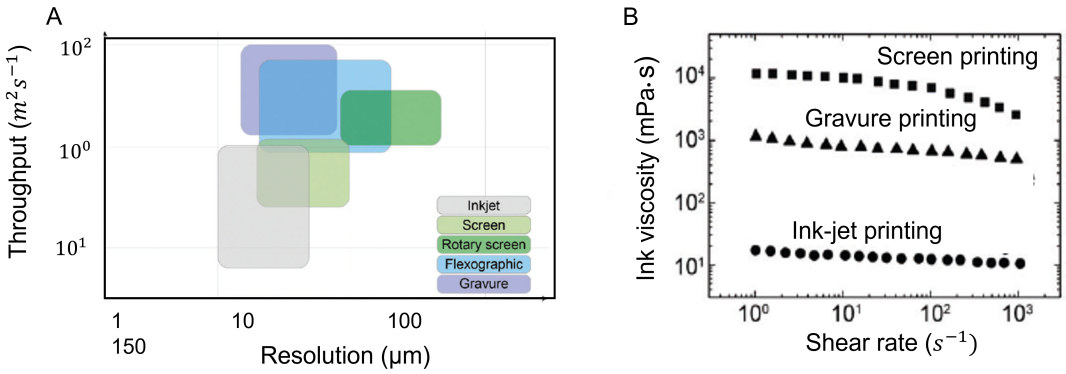

Figure 3.4: A: Throughput and printed feature resoltion for various printing methods. B: Comparison of graphene ink viscosities for screen printing, gravure printing and ink-jet printing respectively [119]

We have discussed above how solution processed dispersions can be formulated into functional inks ready to be printed. The printing processes differ mainly in throughput and resolution, often compromising one for the other as seen in Figure 3.4A. They can be broadly divided into non-digital processes such as screen, gravure and flexographic printing and digital, non-contact processes such as spray coating, ink-jet and aerosol-jet printing. The former has the advantages of being an inexpensive, scalable and reliable method of device manufacturing [218]. They require inks of high loading levels (>10 wt% 2D material concentration) and volumes (> 1L) [119, 222]. Digital printing processes on the other hand have the advantage of being non-contact, high-resolution and mask-less printing processes that require minimal volume (typically 1-2 ml) inks of low loading levels (<0.1 wt% of 2D material concentration) [64, 173, 179, 223]. This is

ideal for investigating new materials that are difficult to synthesize and yield low masses. An example of this is shown in Figure 3.4B where the ink viscosity varies for different printing methods. Therefore, it is essential to select the printing process based on the target printed feature size and fabrication throughput [222]. In the following sections, the two main printing processes used in this work – spray coating and aerosol-jet printing will be introduced

3.2.1 Spray Coating

Spray coating is a method of depositing inks that is widely used in graphic art [224] and industrial coatings [149, 166]. It allows the deposition of inks over rigid and flexible large area substrates [225, 226]. Recently, there have been significant advances in spray coated functional films using solution processed nanomaterials. The versatility of this method has been shown through fabrication of flexible printed gas sensors [227, 228], conductive patterns [226, 229] and even in pharmaceutical applications [230–232]. Casaluci et al. [233] have demonstrated the printability of graphene inks in DMF on large area transparent conductive oxide (TCO) by spray coating. An ultrasonic spray coating method has been reported by Lin et al. [234] to produce transparent conducting films from a hybrid of graphene and conductive nano-filaments. This has several potential applications such as in solar cells, LEDs, touch screens and displays.

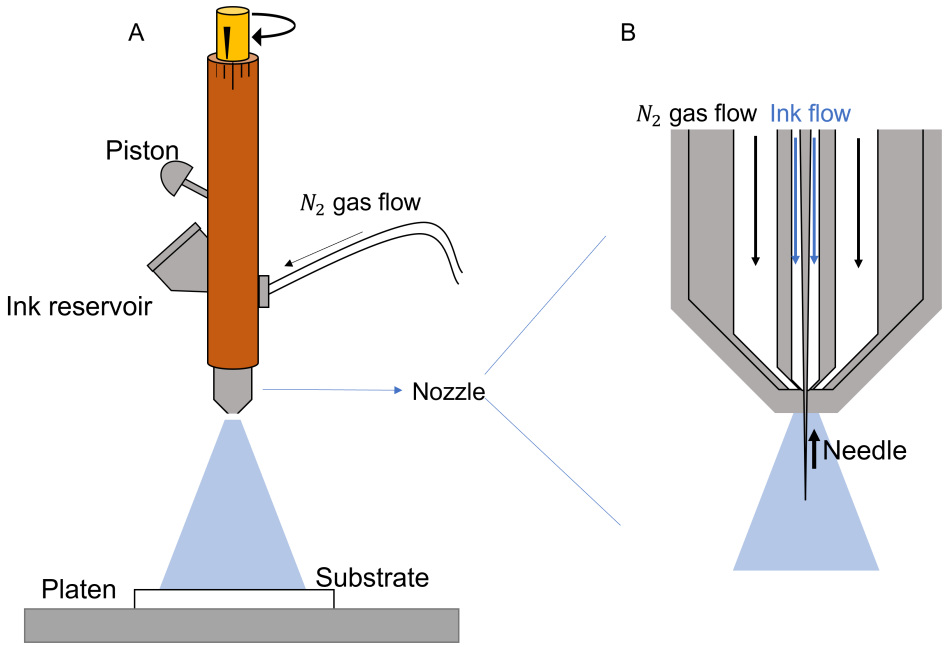

Figure 3.5: A: Schematic of the spray coating process showing the ink flow from the spray gun on to the substrate. B: Zoomed in diagram of the nozzle showing movement of the needle upward allowing the ink to spray out.

Although the mechanism is quite straightforward, spray coating is not a simple process and has several parameters that affect spray. An aerosol of the ink is formed via a back-pressure of N_2 gas or by using electricity, in which case it is termed "electro-spray". Here we will be describing the air-assist spraying technique where the ink is sprayed out

of a nozzle as a fine aerosol formed from the pressure applied by a transporting gas. As seen in Figure 3.5A, N_2 gas flows through the line and into the main body of the airbrush spray-gun where it is met with the ink in the reservoir. As the piston is pushed, the needle (shown in Figure 3.5B) moves up, allowing the ink to spray out. The solvent nature (i.e. polarity, solvent pressure) [235], viscosity [236], flow rate [235], substrate-nozzle distance [225, 237] are some of the parameters that need to be controlled to obtain a uniform film [238].

The nature of the solvent and the platen temperature together determine the evaporation rate at the substrate surface. Low vapour-pressure solvents such as NMP ($0.00045\,atm$ at room temperature) promote long crystal formation by allowing structural arrangement before drying [235]. High vapour pressure solvents like IPA ($0.043\,atm$ at room temperature), toluene ($0.031\,atm$ at room temperature) promote faster solvent evaporation which substantially reduces the ability of functional particles to organise themselves into an ordered fashion, decreasing the final device performance. For example, the work of Owen et al. investigated the effect of solvents on the performance of spray coated organic TFTs. Field effect transistors were sprayed using inks made of three different solvents. Since the semiconductor does not incorporate solvent into its crystal packing, the difference in the value of mobility comes from the fact that the three solvents present different evaporation rates, leading to different morphologies within the film, which is mirrored in its electronic properties. However, just selecting low vapour pressure solvents does not guarantee a uniform sprayed film, the flow rate has to also be adjusted to the solvent. For example, if the flow rate is high while using a solvent such as NMP, it could cause pooling on the substrate. This allows material to flow within the film leading to uneven material distribution and ultimately a non-uniform film. Furthermore, high flow rate with a high vapour solvent could lead to redispersion of any underlying printed films, as is the case while printing stacked heterostructures.

There are several other factors to be considered during spray coating. One such important parameter is the substrate-nozzle distance, d. For small d values, the ink on the substrate can be blown away by incoming flow whereas for large d values, the solvent can evaporate before the droplets reach the substrate. Optimal d values have been cited in the 10–$15\,cm$ range [226, 235]. Yu et al. [239] therefore, have reported a relationship between droplet size and spray height

$$D_{av} = \frac{v_d \Delta H_{vap}}{2\pi\kappa_d \Delta T}$$

where D_{av} is the average droplet diameter, v_d is the average drying rate $(mass/time)$ of the droplet, $\Delta Hvap$ is the latent heat of vaporisation (Jg^{-1}), κ_d is the thermal conductivity of the liquid droplet ($Wm^{-1}K^{-1}$) and ΔT (K) is the mean temperature difference between the droplet surface and the surrounding air [240]. Spray coating is also affected by properties such as surface free energy of the substrate and wettability by the solvent. Film formation during spray coating is therefore a complex process, but has the advantage of being solvent agnostic. it allows for deposition of inks with practically any solvent, considering the viscosity is low enough, unlike in IJP or AJP which are highly sensitive to viscosity and surface tension of inks.

3.2.2 Aerosol-jet Printing

Aerosol-jet printing (AJP) is a non-contact, direct-write digital process for depositing patterns. It can be used to produce conductive traces [170, 241, 242] but also has gained traction in applications involving other functional [243–245] and structural inks [246–248]. Allowing for control over several parameters such as ink flow and focusing during deposition and design flexibility [249], this method is an attractive option for functional ink printing. The opportunity for the functionality of AJP beyond passive patterns and packaging applications was recognised in the DARPA-funded MICE (Mesoscale Integrated Conformal Electronics) project in the late 1990s, which aimed to develop manufacturing processing capable of depositing a range of materials onto various substrates [250]. Aerosol-jet systems were born from this project and have since been commercialised by Optomec Inc. Being relatively new to the printing toolbox, the first research publications featuring AJP began to emerge only in the early 2000s [251].

As was detailed in the previous section, understanding rheological properties of inks is vital in tailoring it to the printing method. The material surface tension, viscosity, volatility, and density introduce a high degree of process variability between different inks. This highlights an obvious drawback of this technique in that determining the optimal printing parameters is a sensitive process [170, 252, 253] because there are several factors at play. This makes consistency and reproducibility challenging as optimal parameters for one ink do not necessarily translate to new materials. Thus analyses of this method have largely been focused on a single aspect of the overall process [252, 254–257].

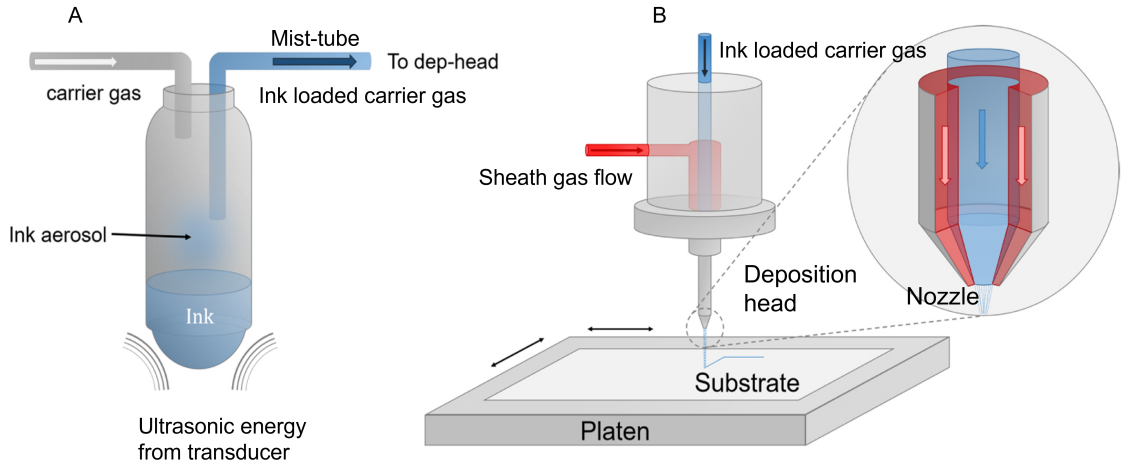

Figure 3.6: A & B: A schematic of the AJP process where the ink is first converted into an aerosol. This is transported by the carrier gas flow through a mist tube to the deposition head where it is virtually focused by a sheath gas flow [258].

Although AJP is often compared with traditional ink-jet printing (IJP) techniques since they are both digital, non-contact printing methods, they have some key differences. Ink-jet printers make use of piezoelectric crystals which expand or shrink depending on the current passed through them, thus allowing ink to flow out of the nozzle. In AJP however, the ink is first converted into a mist through an atomisation process, before it is transported to the nozzle. The printer head of an ink-jet printer consists of an array of nozzles which eject ink to form the printed feature, whereas in AJP, there is

only one nozzle out of which the aerosol-jet mist flows. This gives AJP printed features a far cleaner line edge and highly controllable low resolution patterns. Another main advantage of AJP over IJP techniques is that it is less sensitive to ink rheology, allowing for various types of inks to be easily deposited. In the following paragraphs, we will detail the working of AJP.

The first step of the AJP process as shown in Figure 3.6A is atomisation of the ink into an aerosol. This can be done through ultrasonication or by pneumatic atomisation. The former, which will be the focus in this work generates a more monodisperse aerosol but is only compatible with small volumes of inks of viscosity 1 – 10 cP. Pneumatic atomisation on the other hand can print inks upto 1000 cP [171] but creates more polydisperse droplets in the aerosol. An ideal aerosol is one that is monodisperse and highly dense while the droplets are not too large that they affect minimum feature size or clog the nozzle. In ultrasonic atomisation, a transducer is submerged within a transfer medium (usually DI water) where it is operated at high frequency (MHz). These waves propagate through the transfer medium to a vial containing ink suspended above the transducer. A standing wave is generated within the vial on the surface of the ink and the superposition of consecutive waves results in formation of large peaks. The local shear at the top of the peaks results in small droplets with fairly well-defined size distributions [259, 260] being ejected from the bulk of the ink. The droplets formed are generally between 2 – 5 μm in size [261] and are related to the ultrasound frequency, the ink density and ink surface tension [262]. Higher atomisation power is shown to produce larger droplets [263]. The ink viscosity and volume determine the critical power required for atomisation since the wave must propagate through the liquid surface with limited damping [264].

The generated aerosol is transported through the mist tube to the deposition head via the carrier gas flow. This process typically occurs in the order of 10 s. The droplets colliding with the walls of the tube are lost leading to material build up and possible clogging or contamination. In general, material loss during transport is due to two physical mechanisms – gravitational settling and diffusion. Large droplets are susceptible to gravitational settling while the smaller droplets display increased diffusion away from the beam trajectory. This defines a window of droplet sizes useful for uniform deposition. Thomas et al. [265] have investigated gravitational settling of droplets by calculating the survival probability i.e. the fraction of droplets that remain suspended in the aerosol, as a function of droplet size, gas flow rate and geometry of the mist tube. Loss of material through diffusion occurs by small droplets colliding with the walls of the mist tube and impinging. It is therefore important to control the system geometry in this case as a longer mist tube will lead to increased diffusion losses. However, a longer mist tube will necessitate a higher flow rate.

Another factor to consider is the boiling point of the solvent used in the ink. Since the droplets formed after atomisation are only microns in size, they lose solvent quickly upon contact with the dry carrier gas [266–268]. This results in a reduction of droplet size and leaves the carrier gas flow saturated. This in turn leads to a stable droplet volume during transport. In addition, low boiling point solvents can evaporate in flight resulting in the deposition of dry, discrete particles. This would form features with high surface roughness and porosity. To prevent this, the ink is usually mixed with 10% of a low volatility cosolvent [269] so that it keeps the aerosol wet during transport. Thus, transport efficiency is a non-trivial factor in the AJP process since if nearly constant aerosol density is assumed, any non-linearity in deposition with varying aerosol flow rate

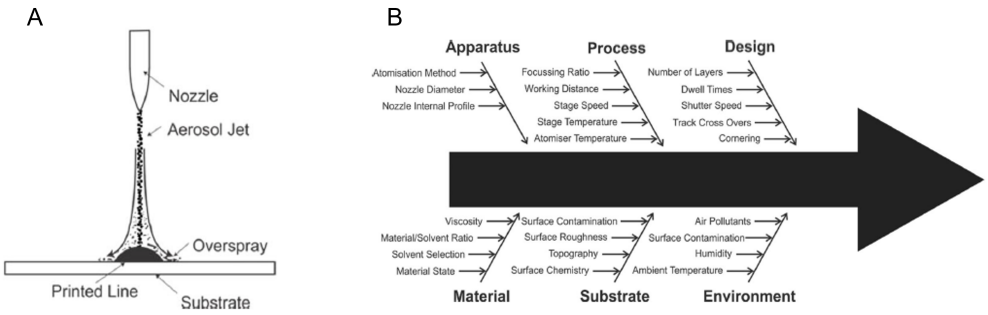

Figure 3.7: A: Over-spray during AJP by caused by drifting small droplets. B: Parameters affecting the AJP process [171]

can be attributed to material loss during transport.

Upon reaching the deposition head, the carrier gas flow is met with a secondary gas flow that constrains and constricts the aerosol within an annular sheath as seen in Figure 3.6B. Termed as sheath gas flow, this air stream creates an interlayer between the aerosol and the physical components of the deposition head, reducing the chances of clogging. It collimates the aerosol to allow for high precision patterning and enables the user to manipulate the aerosol beam without any changes in the hardware. This combination of virtual focusing by the sheath gas flow and physical focusing by the nozzle allows deposition beams that are $1/10^{th}$ the size of the nozzle orifice [248]. By considering a baseline focusing of the aerosol beam as a simple non-mixing volume displacement and modelling a parabolic velocity profile for a fully developed laminar pipe flow, Binder et al. have investigated the collimation of the beam with respect to the nozzle diameter and the focusing ratio i.e. the ratio of the sheath flow rate and carrier flow rate [270]. An important feature of their results is that the collimation is independent of droplet size which means it can be generalised for different inks.

The focused aerosol beam upon leaving the nozzle travels towards the substrate in an impinging jet. The small droplets, lacking enough inertia are carried away from the axis of deposition with the smallest droplets not impacting the surface at all [271]. The droplets of critical size upon impacting will deposit in a broadened pattern [254]. Small droplets could add to overspray around a central thick line as seen in Figure 3.7A. Assuming the critical droplets have the same range of density and velocity, any inertial differences arise from variation in volume of droplets which can be controlled somewhat through ink composition and atomisation parameters. This raises the need for a parameter such as the Ohnesorge number used in ink-jet printing which dictates the rheological properties an ink must have for a successful print [272]. As shown in Figure 3.7B, the AJP process is quite complicated with the apparatus, process and design readily configurable but leaving aspects such as environmental factors, substrate, material and ink formulation challenging to control.

Chapter 4

Printed Networks and their Applications

Flexible electronics are a rapidly expanding research area [273] with the most common fabrication strategy involving direct deposition of functional inks on the target substrate by various coating or printing methods [273–276]. Of late however, printed devices made from solution processed 2D nanomaterials have come to the forefront of nanotechnology research in the form of directly assembled heterojunctions [277–279]. Printed devices are generally a heterostructure made of films that are arranged in-plane or stacked one above the other. The underlying vdW interactions between these films to a large extent removes the conventional lattice matching that constrains traditional compound semiconductor heterostructures [280]. This enables the assembly of relatively strain-free and charge-free heterointerfaces for most 2D materials in the form of photodetectors, photovoltaic cells and other intricate digital circuits [281–285].

These devices are constructed to demonstrate the potential applications of printed electronics, but also can be used as a means to characterise the printed network itself. For example, to investigate properties of printed dielectric films we employ them as the separator in the geometry of a parallel plate capacitor. By analysing the performance of the capacitor, it allows us to describe and detail properties such as the permittivity of that particular dielectric film [63, 78, 286, 287]. Thus, the investigation of the network morphology and its effect on electrical properties such as mobility and conductivity is vital in expanding the potential of printed electronics. In the coming chapter, nanosheet network properties will be discussed with an emphasis on percolation theory and porosity. This will be followed by a discussion on simple parallel-plate capacitors, and the characterisation of their properties using electrical impedance spectroscopy. Finally, a literature review on printed dielectric films will be presented at the end of this chapter.

4.1 Printed Network Properties

In Chapter 3, we have established how solution processed 2D nanomaterials can be tailored into functional inks and deposited via various printing techniques. The components of the ink, its concentration and rheological properties, along with the printing method influence the resulting film. For example, high-concentration inks that are used for contact deposition techniques result in thick films, $> 10\,\mu m$, and are limited by a low pattern resolution of $\approx 100\,\mu m$ [288–290]. More complex printing methods for example, non-contact deposition techniques use low concentration inks for fabricating thin

films. These result in higher resolution features, down to $\approx 10\,\mu m$ features and allow for more intricate patterning [63, 172, 180]. The morphology of these printed films i.e. the arrangement of the nanosheets within the network, directly affect its electrical and mechanical properties [291]. Therefore, it is important to understand the architecture of the printed films in order to fabricate functional devices.

A printed network consists of an array of nanosheets organised randomly, with some degree of in-plane alignment [292]. Nanosheet arrangement, connectivity and porosity are some of the properties that delineate a network. These are the parameters that need to be controlled for optimal functionality of the printed film. An important property of such networks are nanosheet junctions. They can be defined as the locations where nanosheets are in close proximity and are separated only by narrow vdW gap. These junctions play an important role especially in charge transport mechanisms through the film. For instance, reports by Kelly et al. [64] show the conductivity of a network is significantly inferior to the values displayed by single nanosheets. Consequentially, individual nanosheet devices far out-perform nanosheet network-based devices and this is largely due to the presence of nanosheet junctions. This implies that the presence of nanosheet junctions creates a resistance to the flow of charge. This junction resistance depends on the properties of the nanosheet and the network morphology, which in turn is contingent on the deposition method and post treatment, as we will discuss below. In most cases, the junctions introduce resistances orders of magnitude higher than the individual components. An example of this discrepancy is seen in reported MoS_2 film conductivity values which range across five orders of magnitude [64, 179, 293, 294].

Further analysis of the effect of nanosheet junctions can be made by modelling a single current path through the network as being comprised of a series of resistor pairs: the resistance within the nanosheet and junction resistance. The former is an intrinsic material property which means the scope for altering the network resistance lies in controlling the junction arrangement. Although this might be a simplification of the mechanism of charge conduction through the network, it can be said with some confidence that the quality of charge transport through a film is chiefly dependent on network morphology. Below we will discuss percolation theory in the context of conductive nanosheet networks and porosity and packing in the context of dielectric networks.

4.1.1 Conductive Networks

Charge transport in printed electronics is facilitated through conductive networks. Several applications of graphene networks as static electrodes [179, 293, 295, 296], flexible electrodes [297–299], transparent conductors [217, 300], antennae [301, 302], electromagnetic shields [303, 304], supercapacitors [305, 306] and gas sensors [34, 35, 307] have been reported. The difference in morphology of various printed films results in a variation of reported values of mobility of charge carriers across the film and hence conductivity. This disparity is due to the arrangement of nanosheets within the film and ultimately can be related to junction resistances within the network. To further elucidate this point, reported values of graphene film conductivities can be compared for different deposition techniques. Graphene films printed via screen printing, blade coating or flexographic and gravure printing display conductivities of $\approx 10^4 S/m$ [288, 290, 308, 309], which is two orders of magnitude lower than the graphite basal plane conductivity, $\approx 10^6 S/m$ [309]. Ink-jet printed graphene films show a wider range of conductivity values with a mean of $\approx 5.5 \times 10^3 S/m$. Initial reports on AJP graphene

films present conductivities in the range of $\approx 10^3 S/m$ [172, 206, 310, 311] but the results are too few to display a conclusive trend. This is also the case with spin-coated [312, 313] and vacuum filtered films [108, 314] of graphene where conductivity values can range anywhere between $\approx 500 S/m$ to $\approx 2000 S/m$.

The arrangement of graphene nanosheets within the network hence majorly affect film conductivity. The reason for the difference in arrangement and alignment of the nanosheets with different printing methods is largely due to the type of inks used. For example, screen-printable inks that consist of nanosheets with a broad range of sizes and are of a high loading level $(> 50\, g/L)$ [315, 316] generally produce films with nanosheets that are highly aligned in-plane. Inks for IJP and AJP generally consist of nanosheets smaller than $400\, nm$ [179, 180, 293] and use dilute inks $(< 3\, g/L)$ [291, 302, 317] where material migration during solvent evaporation could cause misalignment and more disordered networks. In addition to the arrangement of the nanosheets, conductivity is also seen to depend on nanosheet size. Some studies have observed a nanosheet size dependence on conductivity for graphene oxide [318, 319], graphene [320] and WS_2 [321]. Analogous to work done on mobility in carbon nanotube (CNT) networks where the longer tubes lead to higher mobility due to fewer junctions [321], it can be assumed that larger sheets lead to conductive paths with fewer junctions and thus should have a higher network conductivity. However, the data does not show an obvious trend in favour of this. It is largely observed that the highest conductivities can be achieved with either large or small nanosheets. This suggests that it is the quality, and not the quantity of these inter-nanosheet junctions that is the key factor, at least in the case of graphene networks.

Another significant difference between the various printing techniques is the deposited mass. Screen printed networks are usually tens of microns thick whereas IJP or AJP networks are tens of nanometres thick. As we will discuss below, the thickness of networks plays a role in the connectivity of the nanosheets within it and can be described using percolation theory.

Percolation Theory

Printed networks of LPE nanosheets are severely disordered systems. They require a well-defined model that describes the varying interconnectivity as the network is built up through successive layers. Previously used to describe the evolution of electrical characteristics of CNT networks [322–324], percolation theory provides an intuitively satisfying model that outlines this spatially random process.

Considering AJP as an example for printing dilute inks, we observe that the network formed after a single print is not a continuous one but one that is sparse and poorly connected as shown in Figure 6.4A. The objects, or nanosheets in this case, form discrete islands. As more prints (or passes) are made over it, more material is deposited and eventually a connected path is formed within the network as shown in Figure 6.4C. This path allows for the first amount of current to flow through the film. Known as the percolation threshold, it is the point at which long range connectivity suddenly appears with increasing density/occupation/concentration of nanosheets. As more print passes are made, more connected paths are formed in the network as shown in Figure 6.4D and conductivity increases until it saturates at a bulk value. This scaling law has the form $P \propto \mid t – t_c \mid^n$ [325] where P is the electrical property being investigated, t is the thickness of the network, t_c is thickness at which first conductive path is formed and

n is the exponent describing the system. The exponent n reflects a remarkable aspect of percolation theory as it shows that the material property around the percolation threshold scales independently of the property being measured and is only dependent on the dimensionality of the system [325].

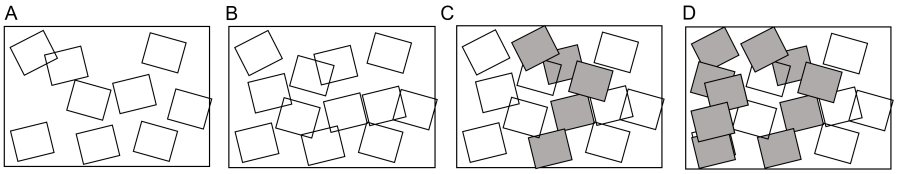

Figure 4.1: Network of nanosheets as more material is deposited after each printing pass, leading to percolative behaviour. Percolative pathways through the network are denoted by the shaded regions.

Percolation theory can also be applied for composite systems where for example, a conductive filler is increasingly added in volume fractions, ϕ. In that case, the equation takes on the form $P \propto| \ \phi–\phi_c \ |^n$ where ϕ_c is the critical volume fraction where percolation threshold is reached. The behaviour of networks in the vicinity of the percolation threshold is of great interest, however it is a highly sensitive and elusive region to examine.

4.1.2 Dielectric Networks

Dielectric materials are often used as part of the passive components of integrated electronic circuits. Typically, these would be polymers or inorganic ceramics. However, polymers have the disadvantage of low permittivity ($\approx 2-5$) and producing crystalline films of inorganic ceramics often requires high temperatures, in excess of $500°C$ [326–328]. With the recent development in flexible, printed electronics, solution processed thin-film dielectrics have piqued an interest. Of late, there have been reported works on the use of hBN [63, 286, 329], montmorillonite [67], titania [330] and $BiOCl$ [172] as part of fully printed electronic circuitry. The key role of dielectric films is in vertically stacked heterostructures as electrical separators for electrolytically gated transistors [64] and lithium ion batteries [331]. They are generally explored by incorporating them into parallel-plate capacitors [63, 78, 223, 286].

It is vital that dielectric films form a continuous network as gaps in the film can cause shorting. These discontinuities are called pin-holes and they present a challenge to the construction of such stacked structures. To a great extent, pin-holes are an artifact of the deposition technique. Figure 4.2A shows a schematic of an ideal zero-porosity network, but in reality all 2D nanomaterial films display some degree of porosity. For example, layer-by-layer (LBL) or electrophoretic deposition (EP) yields tightly tiled networks of nanosheets with a high degree of alignment. Film continuity is sometimes achieved at network thicknesses as low as $20\,nm$ [67, 330, 332, 333].On the other hand, non-contact deposition methods that use dilute inks, such as IJP, AJP or spray coating, are susceptible to non-uniformities during droplet drying [302, 334, 335]. These types of films are depicted in the schematic in Figure 4.2B and need to be $1-2\,\mu m$ thick to form

continuous networks. This disparity is especially evident when comparing the minimum insulating thickness of films i.e. the thickness at which the films are continuous without pin-holes, of the same material deposited using different printing methods. For example, boron-nitride nanosheets deposited by IJP/AJP reach an insulating thickness at $\approx 1\,\mu m$ [63, 286] whereas when assembled via LBL or EP, they need only be tens of nanometres thick to form a continuous film [336, 337].

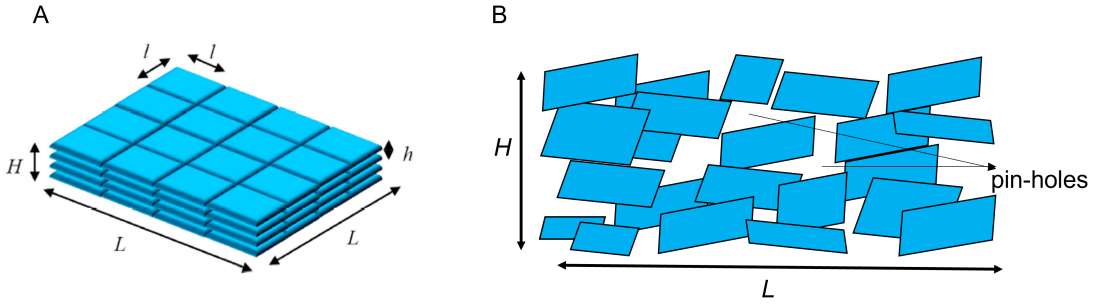

Figure 4.2: A: Schematic showing the idealised layout of a zero-porosity network [291]. B: Schematic showing the realistic cross-section of a 2D nanosheet network with oblique junctions and pin-holes.

As mentioned above, discontinuities in dielectric films can lead to shorting. It then follows that network porosity, which can be quantified as P_{net} must be controlled. Highly porous networks tend to have poorly aligned nanosheets leading to oblique junctions with low area, point-like contacts. When the nanosheets within the film are aligned, the porosity is low as junctions are formed with large basal plane area overlaps leading to desirable network properties. Barwich et al. have examined the effect of applying heat and pressure to controllably annihilate large pores $(> 40\,nm)$ in nanosheet networks and improve nanosheet alignment [291]. They estimated network porosity as $P_{net} = 1 - \frac{\rho_{net}}{\rho_{ns}}$ [64, 291] where the density of the film is derived from measurements of the film mass and dimensions. This brings to light that the mechanical properties of networks are also important. As a film is deposited, nanosheets must be easily able to conform to the ones underneath. This conformality, albeit partially driven by vdW interactions, depends mainly on the bending rigidity of the nanosheets. Classically, the bending rigidity can be written as $D \sim Eh^3$ where E is Young's modulus and h is the thickness [338, 339]. It should be noted however, that this model breaks down at the monolayer limit [340]. In the case of 2D nanomaterials, h is extremely small meaning that they can be very flexible. Considering that thin nanosheets are highly conformal and a large basal plane allows for nanosheet alignment, it can be concluded that the aspect ratio is the chief geometrical variable in determining the quality of networks [318]. Nanosheets produced by LPE however often have low aspect ratios (< 30) [341] and pose a challenge to producing well defined networks.

Post-processing

Printed nanosheet networks typically require some sort of processing after deposition to improve network properties for optimum device performance. Post-processing techniques

can involve calendaring and thermal or photonic annealing. Calendering or compressing of films can lead to improvements in network conductivity by reducing the porosity, and improving nanosheet alignment within the film [316, 342–345]. However, as it involves physical contact, this technique could easily damage the type of films that are used in this body of work. In this case, we turn to thermal annealing which involves heating the network in a vacuum oven. It is important to anneal in vacuum to prevent oxidation of the films at high temperatures, however this depends on the material. Usually, it is to remove trapped solvent within the network or in some cases to degrade any ink-stabilising polymers or additives that might be undesirable in the film [346, 347]. For example, thermal annealing has been shown to drive changes in the vertical inter-layer spacing (on the order of angstroms) in both MoS_2 [348] and graphene oxide networks [349], leading to improvements in the out-of-plane conductivity. When considering printed electronics on flexible substrates such as PET, high temperatures cannot be used. In such cases, photonic annealing can be performed where a series of light pulses are applied to a nanosheet network causing a rapid increase in local temperature (up to $500^{\circ}\,C$ [350]. This decomposes the unwanted organics such as polymers while leaving the substrate intact. When polymers are included as part of the ink formulation and deposited into the film, they sterically separate the nanosheets. Thus, their removal is beneficial as it would significantly collapse the network structure [351] causing more contacts between the nanosheets, which reduces the porosity and enhances network properties such as charge carrier conduction.

This work largely deals with improving the permittivity of printed dielectric films made of solution processed 2D nanosheets and their composites. As mentioned above, they will be investigated through their integration into a capacitor geometry. Thus, in the sections that follow we will describe in detail the working of a parallel-plate capacitor, along with a discussion on impedance spectroscopy and modelling techniques used in this work to characterise the dielectric films.

4.2 Capacitors

The genesis of capacitor technology is generally attributed to the invention of the Leyden jar in 1745 by the German scientist Ewald Georg von Kleist and independently by the Dutch physicist Pieter van Musschenbroek in 1746 [352]. The Leyden jar is a narrow necked jar partially filled with water with an electrical lead brought through a cork into the neck of the bottle of water. The Dutch version of the jar employed a foil over the outside surface that acted like an electrode. Kleist's implementation however, was more colourful as his hands holding the jar formed the outer electrode, which led him to experience a painful shock as he touched the lead going in to the water. It was in fact Benjamin Franklin, the great American statesman and inventor that later showed that the water in the jar was not essential and proceeded to make flat capacitors consisting of a sheet of glass between foil electrodes [353]. The first practical fixed and variable capacitors were invented by Michael Faraday, the scientist whose name is now the unit for capacitance.

A capacitor is an important two-terminal electrical device whose function is to store electric charge. They are primarily used as low or high-pass band filters and in high speed switching logic circuits. As shown in Figure 4.3, it is a simple system consisting of two parallel metal plates, of area A that contain a dielectric material between them and are separated by a distance d. As the two metal plates are charged, positive charge $+Q$

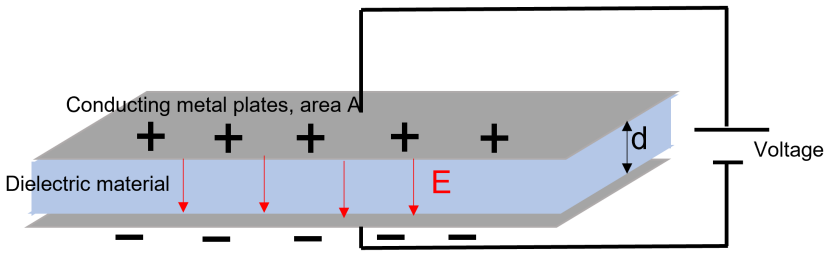

Figure 4.3: Geometry of a parallel plate capacitor of area A and thickness d.

is accumulated on one plate and a negative charge $-Q$ of the same magnitude on the other. The charges on the plates create a potential difference, V, that is proportional to their magnitude, Q. Thus we can write $Q = CV$ where C is the proportionality constant called capacitance. By considering the voltage V, the distance between the plates, d, and defining surface charge density, $\sigma_{sc} = Q/A$, we can write $V = Ed$ where E is the electric field strength that is generated between the plates. Consequentially, it can be shown that $C = \frac{\sigma_{sc}A}{Ed} = \frac{\epsilon A}{d}$. Here, $\epsilon = \sigma_{sc}/E$ is the permittivity of the material between the two metallic plates. The so called dielectric constant or relative permittivity of a dielectric material can be written as $\epsilon_r = \epsilon/\epsilon_0$ where ϵ_0 is the permittivity of free space of the value $8.854 \times 10^{-12} m^{-3}\, kg^{-1} s^4 A^2$.

For dielectric materials, the permittivity is dependent on the frequency of the applied electric field, E. It also depends on the chemical structure and imperfections/defects of the material along with other physical parameters like pressure and temperature. The permittivity of a material is a measure of electric polarisation, i.e. the relative displacement of negative and positive charges of atoms or molecules within the material. Polarisation requires time to take place and is the reason that it is dependent on the time variation, i.e. frequency of the applied electric field. An ideal dielectric material is one with no mobile charge carriers (electrons or ions) that is able to store electrical energy.

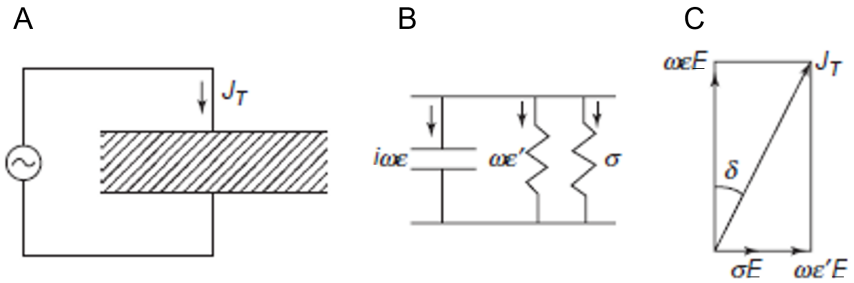

Figure 4.4: A: Circuit diagram of current J_T flowing through a capacitive circuit. B: Circuit diagram representing the dielectric loss contributions. C: Phasor diagram representing the loss angle, δ.

Resistors are circuit elements that resist the flow of current. Electrical resistors

follows Ohm's law ($V = IR$) at all current, voltage and frequencies. Moreover, the voltage and current signals are "in-phase" with each other, which means there is no phase difference between them. Capacitive behaviour is different in that the resistance it presents to the flow of current is dependent on the frequency of the AC voltage applied. When a time-varying electric field is applied across a parallel-plate capacitor, the current leads the voltage by 90° and in these cases, a more general concept of resistance is used, called impedance. Impedance takes into account the voltage and current phase differences through circuit elements.

Consider an applied sinusoidal field, E, where $\omega = 2\pi f$ is the angular frequency and E_m is the amplitude of the signal or magnitude of the electric field.

$$E = E_m e^{i\omega t} \tag{4.1}$$

When a time varying electric field of this nature is applied across a parallel-plate capacitor, the total current density, J_T through the dielectric as depicted in Figure 4.4A can be written as

$$J_T = J + \epsilon^* \frac{dE}{dt} \tag{4.2}$$

where J is the conduction current and ϵ^* is the complex permittivity that is introduced to allow for dielectric losses due to orientation of electric dipoles. First let us consider the conduction current, J. Considering a material with cross-sectional area, A and length l displaying a resistance of R, the conductivity can be written as

$$\sigma = \frac{l}{AR} = \frac{lI}{AV} \tag{4.3}$$

The current density can be defined as $J = I/A$ since it is the magnitude of current per cross-sectional area of the material. Furthermore, the voltage across the material and the applied electric field are related as $V = El$. Thus, it follows that Eqn. 4.3 can be written as

$$\sigma = \frac{J}{E} \tag{4.4}$$

In order to work out the current density due to dielectric losses, the complex permittivity can be written as

$$\epsilon^* = \epsilon - i\epsilon' = (\epsilon_r - i\epsilon'_r)\epsilon_0 \tag{4.5}$$

where ϵ_r is the dielectric constant and ϵ'_r is the loss factor. Using Eqn. 4.1 and Eqn. 4.5, the second term of Eqn. 4.2 can be written as

$$i\omega(\epsilon - i\epsilon')E \tag{4.6}$$

Finally, using Eqn. 4.4 and Eqn. 4.6, the total current density can be written as

$$J_T = (\sigma + \omega\epsilon')E + i\omega\epsilon E \tag{4.7}$$

The first term of Eqn. 4.7 is a loss component that is present at all frequencies, even $\omega = 0$ i.e. DC voltage. It is due to inelastic scattering of charge carriers with scattering sites. The second term is also a loss component, but one that increases with frequency and disappears at $\omega = 0$. This contribution to loss is due to the material resistance to

polarisation. The conductivity, σ, in dielectric materials is generally very small and so can be neglected. It would follow that

$$\tan\delta = \frac{\epsilon'}{\epsilon} \tag{4.8}$$

and is termed the loss tangent. In the case that $\epsilon'/\epsilon << 1$, Eqn. 4.5 simplifies into

$$\tan\delta = \frac{\epsilon'}{\epsilon} \approx \delta \tag{4.9}$$

where δ is the termed the loss angle. A representation of the various loss components of a capacitor is shown in Figure 4.4B and C. Having established the basic working of a capacitor and describing permittivity of dielectric materials, we will now discuss the means by which these characterisations are made - through a technique called impedance spectroscopy.

4.3 Impedance Spectroscopy

Impedance spectroscopy is a well-established body of research, albeit one that is the subject of many controversies. It is based on the detection and interpretation of processes that occur in response to an external voltage perturbation applied at predetermined AC frequencies. The current in response to this perturbation is indicative of the physical or mechanical structure and chemical composition of the analysed system. Historically, it was used to analyse electrically conductive ionic fluids or to analyse highly resistive materials such as polymers, ceramics and organic colloids [354]. The dielectric impedance response in particular, is based on the concept of energy storage and the resulting relaxation per release of this energy. This notion was introduced by Maxwell and later expanded by Debye who used it to describe the time required for dipolar molecules to reversibly orient themselves in an external AC field.

Hence, impedance analysis of dielectric materials allows us to extract two of their fundamental properties - permittivity, ϵ, and conductivity, σ. These two are characteristic of the materials ability to store electrical energy and transfer electrical charge respectively. They are both related to molecular activity and depend on the frequency of the applied oscillating electric field. In the terahertz frequency range, polarisation can be electronic and atomic in the form of very small translational displacements of the electron cloud. Orientational or dipolar polarisations i.e. rotational moments experienced by permanently polar molecules are experienced in the megahertz to kilohertz frequency range. Finally, polarisation can be ionic with ion displacement within the material in the kilohertz to hertz frequency range.

Consider an applied sinusoidal voltage of the form

$$V = V_0 e^{i\omega t} \tag{4.10}$$

The current is at the same frequency but phase shifted

$$I = I_0 e^{i(t-\theta)} \tag{4.11}$$

where $\theta = -90^\circ$ for ideal dielectrics. Using Eqn. 4.10 and 4.11, the impedance, $|Z|$ can be defined as

$$Z = \frac{V}{I} = \frac{V_0 e^{i\omega t}}{I_0 e^{i(t-\theta)}} = \frac{V_0 e^{i\theta}}{I_0} = |Z| e^{i\theta} \tag{4.12}$$

Using de Moivre's theorem we can represent impedance as a complex number,

$$Z = |Z| \cos\theta + i|Z| \sin\theta = Z_{real} + iZ_{imaginary} \tag{4.13}$$

We had mentioned above that the two characteristic properties of a dielectric are the storage of electrical energy, that is represented by its permittivity and the transfer of electric charge, that is represented by its conductivity. We shall now see how the real and imaginary impedance can represent these two quantities. Consider a dielectric sandwiched between two electrodes. When an alternating voltage (Eqn. 4.10) is applied, an alternating current will flow (Eqn. 4.11). As we described earlier, this current has two components - one that is due to Ohm's law and the other due to the polarisation of the dielectric in response to the voltage i.e. the alternating charging/discharging of the capacitor. The first term can be written as $I = V/R$ and the second as $I = dQ/dt$. Hence, using $Q = CV$, we can write

$$I = \frac{V}{R} + C\frac{dV}{dt} \tag{4.14}$$

Substituting Eqn. 4.10 in 4.14,

$$I = \frac{V_0 e^{i\omega t}}{R} + i\omega C V_0 e^{i\omega t} \tag{4.15}$$

Using the definition of impedance from Eqn. 4.12,

$$\frac{I}{V} = \frac{1}{R} + i\omega C = \frac{1}{Z} \tag{4.16}$$

Capacitance and resistance can be written in terms of permittivity and conductivity as

$$C = \frac{\epsilon A}{L}$$

and,

$$R = \frac{L}{A\sigma}$$

So, Eqn. 4.16 becomes

$$\frac{1}{Z} = \frac{\sigma A}{L} + i\omega\frac{\epsilon A}{L} = \frac{A}{L}(\sigma + i\omega\epsilon) \tag{4.17}$$

Dividing through by $(i\omega A/L)$ we have

$$\epsilon - i\frac{\sigma}{\omega} = -i\frac{1}{Z}\frac{L}{\omega A} \tag{4.18}$$

Since impedance is a complex number, (Eqn. 4.13),

$$\epsilon - i\frac{\sigma}{\omega} = -i\frac{1}{Z_{re} + iZ_{im}}\frac{L}{\omega A} \tag{4.19}$$

Finally, by multiplying top and bottom of Eqn. 4.19 by the complex conjugate, we can write

$$\epsilon - i\frac{\sigma}{\omega} = \frac{L}{\omega A}\frac{-iZ_{re} - Z_{im}}{Z_{re}^2 + Z_{im}^2} \tag{4.20}$$

By comparing the real and imaginary parts of Eqn. 4.20, it is clear that the permittivity can be written as

$$\epsilon = \epsilon_r\epsilon_0 = \frac{-Z_{im}}{|Z|^2}\frac{L}{\omega A}$$

Note from Eqn. 4.13 that Z_{im} is negative since $\theta = -90^\circ$ making permittivity is a positive number. The frequency dependent conductivity can then be written as

$$\sigma = \frac{L}{A}\frac{Z_{re}}{|Z|^2}$$

Graphical Representation of Impedance Spectroscopy data and Circuit Models

We have established that impedance spectroscopy involves the measurement of the current response to an AC voltage perturbation at a range of frequencies. The impedance therefore is the ratio of the applied voltage and measured current, at each frequency. As seen above, impedance is a complex number and has real and imaginary parts. Impedance data can be presented in two ways - via a Bode plot or a Nyquist plot. The Bode plot displays the phase angle and the logarithm of the impedance magnitude as a function of the logarithm of frequency. It explicitly shows frequency information. The Nyquist plot shows the imaginary impedance plotted against the real impedance. The impedance spectra often appear as single or multiple arcs in the complex plane. Nyquist plots are especially popular because the shape of the plot yields insight into possible conduction mechanisms or kinetic governing phenomenon. This will be discussed more in detail below.

It is important to note here that impedance spectroscopy should not be applied without some prior knowledge of the analysed system's chemical, physical, mechanical and electrical characteristics. In order to avoid misinterpretation of the data, a preliminary idea of what the system is expected to perform like is necessary. The experimental data must often be interpreted within the context of the developed model even before the data is acquired. We will now describe the impedance response of a few common circuit models.

The impedance of a simple capacitor can be easily derived from the definition of capacitance,

$$C = \frac{Q}{V} \tag{4.21}$$

We can write

$$I = \frac{dQ}{dt} = C\frac{dV}{dt} = C(i\omega)V \tag{4.22}$$

Therefore,

$$Z = \frac{V}{I} = \frac{1}{i\omega C} \tag{4.23}$$

Thus, the impedance of a capacitor increases as the frequency is reduced. A more realistic circuit model contains both resistive and capacitive elements. One such circuit

model is the $R||C$ circuit which consists of a resistor and a capacitor in parallel as shown in Figure 4.5A. As the frequency is scanned the current flows according to the path of least impedance. At low frequencies, the current flows only through the resistor as the impedance due to the capacitor is highest. The impedance due to the resistor is independent of frequency and follows $V = IR$ with a phase $\phi = 0°$. At high frequencies, the current flows entirely through the capacitor, following $Z = 1/\omega C$ with a phase $\phi = -90°$. The phase transitions from $0°$ to $-90°$ at the critical frequency $f_c = 1/(2\pi RC)$ at $45°$. The value $\tau = RC$ is referred to as the time constant of the circuit and is a measure of the rate of discharge of the capacitor.

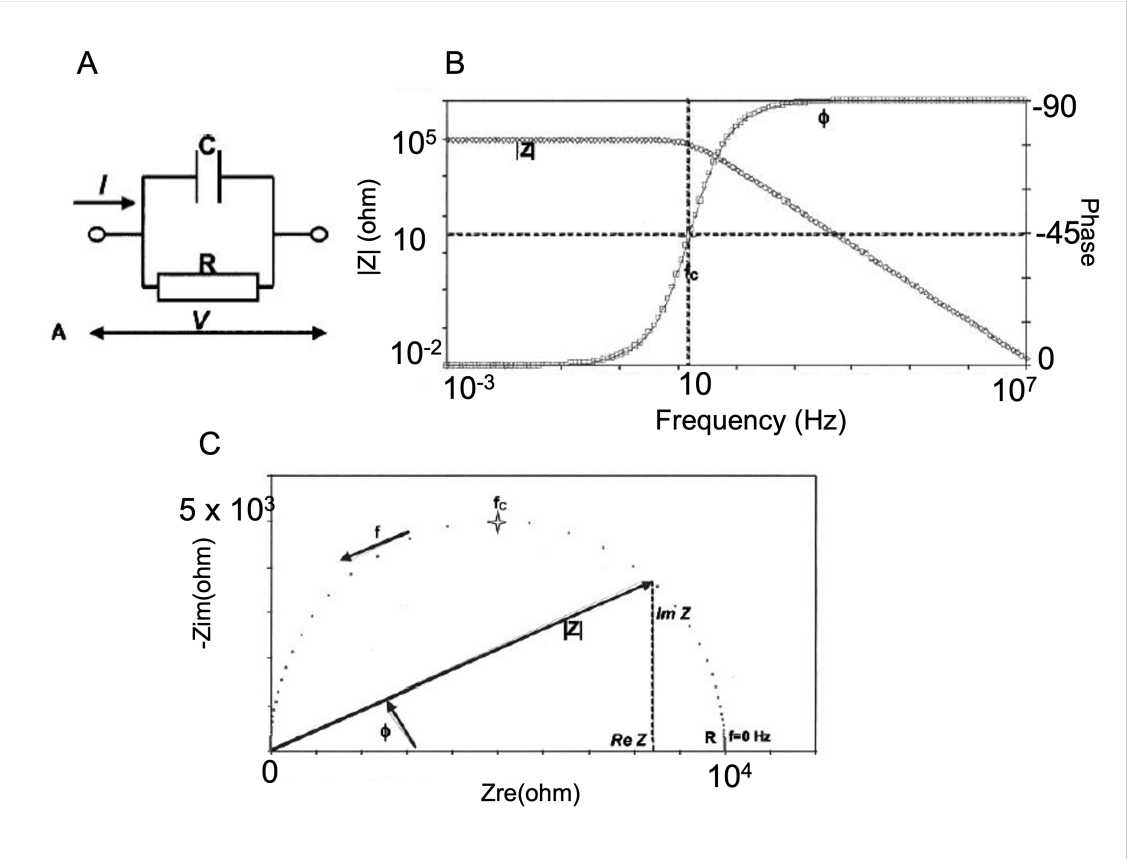

Figure 4.5: A: Circuit diagram of an $R||C$ circuit and its respective B: Bode and C: Nyquist plots [354].

The impedance of a $R||C$ circuit is added according to

$$\frac{1}{Z_T} = \frac{1}{Z_R} + \frac{1}{Z_C}$$

We know $Z_R = R$ and $Z_C = -i/\omega C$ so,

$$Z_T = \frac{R(-i/\omega C)}{R - (i/\omega C)}$$

By multiplying the top and bottom by $R + (i/\omega C)$, the complex conjugate of the denominator, we get

$$Z_T = \frac{R}{1 + (\omega RC)^2} - i\frac{\omega R^2 C}{1 + (\omega RC)^2} \tag{4.24}$$

with the first term being Z_{re} and the second term Z_{im}. Hence, the phase can be determined by $\phi = \tan^{-1}(-\omega RC)$. The Nyquist plot of a $R||C$ circuit, shown in Figure 4.5C is a semicircle starting at the origin and each point denoting the frequency of measurement. The x intercept denotes the resistance, R,and the impedance vector denotes $|Z|$ and the phase angle ϕ.

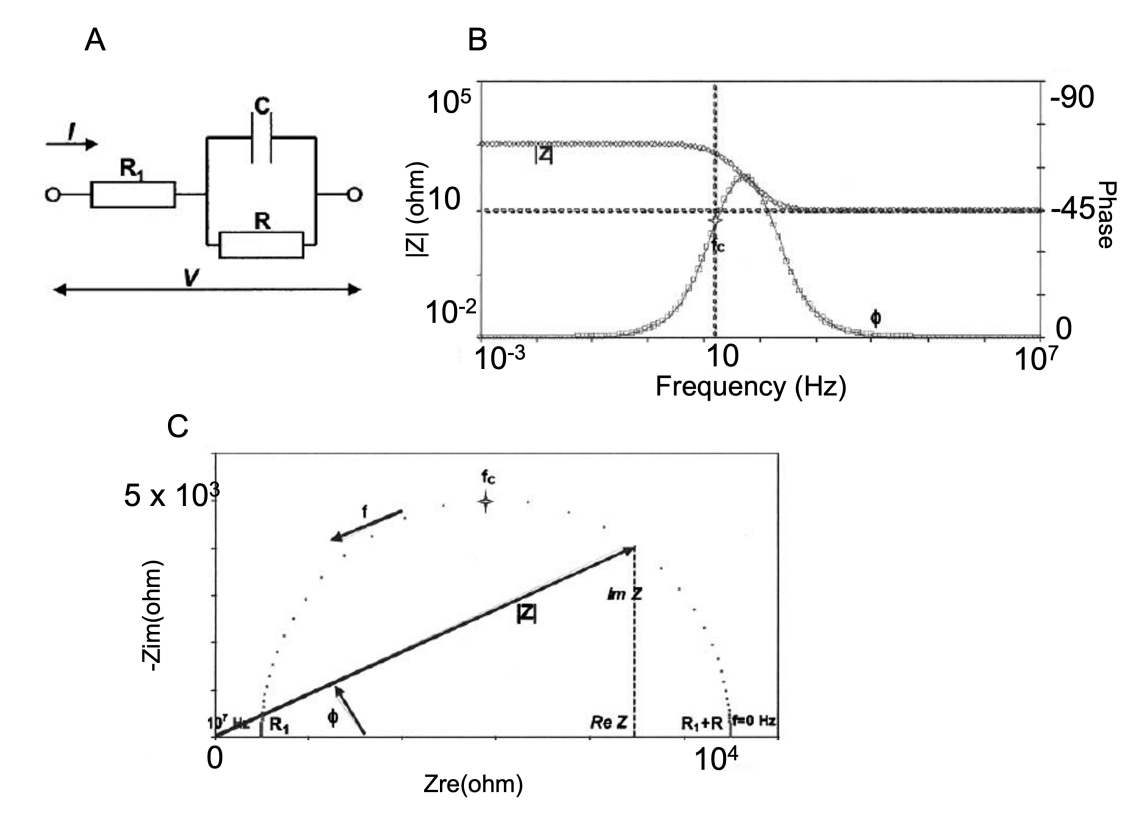

Figure 4.6: A: Circuit diagram of a Randles circuit and its respective B: Bode and C: Nyquist plots [354].

The Randles circuit is a slightly more complicated circuit model where a resistor, R_1 is added in series to the above circuit as seen in Figure 4.6A. At low frequencies, when the impedance from the capacitor is at its highest, the current entirely flows through the two resistors. The height of the plateau as seen in Figure 4.6B at low frequency thus represents $(R + R_1)$. The phase angle is 0° and the current flows according to $I = V/(R_1+R)$. At medium frequencies, the current is distributed between the capacitor and resistor, R and the phase angle starts to go towards -90° as we begin to see capacitive effects. At high frequencies, the impedance is equal only to series resistance, R_1 that is represented by the height of the plateau at low frequency and the phase returns to 0°.

The impedance response of a Randles circuit only differs slightly from the $R||C$ circuit as

$$Z_T = Z_{R1} + Z_{R||C}$$

Therefore, the total impedance can be written as,

$$Z_T = R_1 + \frac{R}{1+(\omega RC)^2} - i\frac{\omega R^2 C}{1+(\omega RC)^2} \tag{4.25}$$

The Nyquist plot as seen in Figure 4.6C is also a semi-circle but with x-axis intercepts R_1 at high frequency and $(R_1 + R)$ at low frequency.

4.3.1 A Review of Printed Dielectric Films

Dielectrics play an important role in printed electronics, especially in heterostructure devices where conductive elements need to be electrically isolated from one another. They mainly function as charge separators and enable independent device arrays in integrated circuits. In thin-film transistors (TFTs), a good gate dielectric allows for lower switching voltages [355, 356]. A common issue in TFTs is charge carrier scattering at the dielectric/semi-conducting interface that leads to a reduction in carrier mobility. This is mostly due to charge traps in the dielectric surface and phonon scattering caused by high-κ dielectrics. Thus, the investigation of dielectrics with high permittivity and low losses are vital to the progress of printed electronics. Improving dielectric permittivity, breakdown strength and mechanical robustness will ultimately lead to better device performance. In this review, we will discuss the three main types of dielectrics that have emerged in the field of printed electronics.

Ceramic and Metal Oxide Dielectric Films

In electronics, capacitors can be generally classified depending on their function and operating frequency as being surface-mount, on-chip or embedded. Discrete surface mount capacitors are usually made of ceramic materials and termed as multi-layer ceramic capacitors (MLCC). Over the years, several studies on developing MLCCs into integrated circuits have been made [357]. In the past, ceramic powders would be cast and sintered into dense bodies. Solution based deposition approaches however are more scalable and tend to be more robust. Another avenue of progress in the field of dielectric materials has been in metal oxides. They have demonstrated desirable properties such as high relative permittivity and low dielectric losses for use as gate dielectrics in TFTs [358–360].

MLCCs enable application flexibility and show large capacitance values with manageable operating voltages. Common high permittivity ceramics are usually ferromagnetic materials for example, $BaTiO_3$, PZT and $Bi_4Ti_3O_3$. These have also been integrated in silicon based electronics [361–364]. $Ba_{0.6}Sr_{0.4}TiO_3$ (BST) is emerging as a suitable candidate for applications in embedded memories, frequency agile tunable devices and embedded capacitor layers [326], exhibiting high permittivity values ($\epsilon_r = 700$). In parallell, metal oxides such as Al_2O_3, SiO_2, HfO_2 and TiO_2 are showing great promise as gate dielectrics in printed electronics [365–368]. Their direct deposition on substrates and electrodes via various methods such as CVD, CSD, ED and pulsed layer deposition allows for control over film growth. Among these, TiO_2 has caught the most traction for its high dielectric constant, low cost and low toxicity [369, 370].

Ceramic dielectric materials pose certain disadvantages. MLCCs often require high operating frequencies (100 - 300 MHz) [357] because of their geometrically restricted distance from integrated circuits. Furthermore, they require high temperatures to obtain crystalline structures. For example, BST needs a process temperature of 700 $^\circ C$ and N_2 pressure of 13.3 Pa [326]. Post-processing temperatures in excess of of 500 $^\circ C$

are often necessary. Electrophoretically deposited $BaTiO_3$ films must be sintered at 1300 - 1400 $^{\circ}C$ [328]. These high temperatures make ceramic dielectric films unsuitable for plastic substrates. Thus, there is a challenge in integrating ceramic materials with appropriate deposition techniques, patterning and thermal annealing processes required for device fabrication. Metal oxides too pose challenges in film growth. Commonly used techniques such as atomic layer deposition require functionalisation of the underlying layer or substrate [371, 372]. Pulsed vapour deposition and sputtering could be used as they do not require functionalisation, but they too cause significant damage to the underlying layer and can result in poor quality dielectrics [373, 374].

In order for ceramic dielectric films to be embedded in printed wiring boards, there is a need to reduce the high process temperatures. Several studies on polymer-ceramic composites are emerging to circumvent this issue [375–377]. First, the ceramic film is coated on metal foils and is processed at high temperatures. This is then embedded into polymer packages. These composite devices show permittivity values orders of magnitude higher than pure polymer films but the dielectric properties of the ceramic film is observed to be deteriorated. If the ceramic content is increased, the films become brittle and hence difficult to fabricate devices out of.

Polymer Dielectric Films

The development of electronic circuits on flexible substrates has been ongoing since the start of the 21^{st} century. Depositing dielectric materials as separators and gate dielectrics over plastic substrates is only possible at low temperatures, unlike conventional silicon based devices or those from the above mentioned ceramic dielectrics. This is where the use of polymer-based dielectrics in flexible organic thin-film transistors (OTFTs) has seen immense growth [378–380]. In addition to this, polymer films are also sometimes used as a buffer between the semiconducting channel and traditional gate dielectrics in TFTs to improve charge carrier mobility [77]. This section will detail some of the main advantages and shortcomings of polymer dielectric films.

Polymers allow for easy processing as they are compatible with various deposition techniques such as spin-coating, printing and evaporation. This enables large area films to be conveniently deposited onto several substrates in a functional device geometry with an opportunity for structural modifications. Recently there has been reports on the use of dipolar glass polymers that show relatively high permittivity (≈ 6) [381, 382]. These polymers display intrinsic microporosity and have been used in high performing FETs from solution-casted films [383]. In the past, low-frequency passives using polymers on flexible plastic substrates have been demonstrated through ink-jet printed devices [145, 384]. Cook et al. have since demonstrated flexible multi-layer RF capacitors using two custom formulated polymer based dielectric inks [385]. Thus, polymers are a versatile option for use as dielectrics in functional devices.

There are however some shortcomings of polymer dielectric films. It is difficult to raise the electrical permittivity above 5 for linear dielectric polymers [381, 386]. There are very few choices of suitable polymer dielectrics with sufficiently high permittivity for high performing OTFTs. As a result, they require high operating voltages, sometimes $> 100V$ since a thick dielectric layer is required to eliminate gate leakage current. Another issue is that polymer dielectric materials interfacing with the semiconducting channel can cause mobility degradation and instability issues in the transistors [387]. This makes developing high-κ dielectrics that are compatible with OTFTs a challenge

[388].

Polymer dielectric films often have low breakdown strength due to the large free volume in the solid state. This also leads to redispersion of the polymer layer during deposition of subsequent organic layers ultimately affecting performance [389]. Recently, there has been development in cross-linking polymers at relatively low temperatures with the help of reagents. Li et al. have developed a cross-linking reagent that improves solvent resistance during solution processing and increases electrical robustness [378]. Solid polymer electrolytes in the form of ion gels are being developed where inorganic/polymer composites create an electrical double-layer and obtain high capacitances for low operating voltages [390]. Thus it is necessary to further explore dielectric materials beyond polymers.

Dielectric Layered Crystal Networks

The advent of 2D nanomaterials has opened up another avenue in materials research for device fabrication. An entire family of materials with desirable properties is fueling the ever expanding field of printed electronics. Among printed dielectric nanomaterial films however, boron-nitride (hBN) has dominated the field owing to its similarity to graphite and its low cost, abundance and ambient stability. The majority of the reported work on hBN has been based on mechanically cleaved high-quality thin flakes or from solution processed inks that are deposited via coating techniques or digital printing methods such as ink-jet and aerosol-jet printing.

Mechanically cleaved nanosheets are of superior quality and consist mostly of atomically flat thin films that are robust and have few defects. Devices fabricated from them show high performance for example in the work of Britnell et al. where defect-free ultrathin hBN crystalline layers are formed through mechanical cleaving and show high breakdown field [391]. Withers et al. have fabricated LEDs made by stacking conductive graphene, insulating hBN sheets produced by the peel-lift/vdW technique [392] and various other semiconducting monolayers into complex designed sequences [393].

Solution processed hBN has the advantage of yielding large quantities and being easy and cheap to produce. It allows for large area printing on several substrate surfaces with high design flexibility. For example, Zhu et al. have created a "one pot" formulation of polyurethane and hBN that was deposited into capacitors via the K-bar coating method to yield films of permittivity close to 8, [332] which is higher than other reports of hBN films. Another study reported electrophoretically deposited films of hBN in 2-butanone that showed a permittivity of 5 [333]. Several reports have also deposited LPE hBN nanosheets via digital printing methods [63, 286, 385, 394]. The inks were formulated with binders or polymers accordingly to tailor their properties to suit the printing technique. The highest permittivity among these was achieved by Worsley et al. with water based inks that were ink-jet printed into capacitors, giving a permittivity of 6 [78].

The reported work on printed dielectric films of 2D nanomaterials is highly skewed towards hBN. The above mentioned works are still limited to permittivities between $\approx 2-8$. Furthermore, films of hBN are quite porous and can be brittle which poses challenges to printed devices. There has been some significant work done with 2D nanosheets of other materials such as montmorillonite (MTM) [395–398] and titania [399–402]. Ultrathin dielectric films from solution processed 2D nanosheets of MTM have been assembled on silicon and show high capacitances of $\approx 600\,nF/cm^2$ and low

leakage currents down to $6 \times 10^{-9}\, A/cm^2$ [67]. They display a permittivity of 5.7. Other studies involve films fabricated from titania nanosheets. Osada et al. have demonstrated high-κ films of 2D nanosheets of titania which exhibit high relative dielectric constant of ≈ 125 and low leakage currents of $10^{-9} - 10^{-7}\, A/cm^2$ [330]. Although films of MTM and titania have desirable dielectric properties, their fabrication is generally through layer-by-layer deposition or electrostatic self-assembly which are complex processes that involve high temperatures and sensitive environments. They have not yet been deposited using digital or scalable printing techniques. Below is a table comparing the different publications on printed electronics using solution processed 2D dielectric nanomaterials.

While other printable dielectric materials may be more mature, printed networks of dielectric layered crystals appear to offer compelling advantages over polymeric and ceramic networks. They can be processed at ambient temperatures and show potential of scalability. However, there is a lack of reports of fully printed heterostructure devices in the field of printed electronics. Vertically stacking printed films often leads to shorting via redipsersion and damage of the underlying layer during subsequent layer deposition. It is in this vein that the following chapters are focused on exploring dielectric 2D materials with high permittivity that can be readily used to fabricate printed electronic devices.

Reference	Materials + substrate	Method of deposition	Fit parameters: R, C/A	Dielectric constant
ACS Nano 2019, 13, 54−60	Water based graphene and hBN inks; Pre cleaned glass substrate	All ink-jet printed	(Randles) Rser ~ 90kohm Rleak > 1Gohm C/A ~ 2nF/cm^2 for 3 um thickness	6.1 ± 1.7
10.1002/adfm.202002339	"one-pot" formulation (exfoliated together) of polyurethane (PU) w/ hBN nanofillers + hardener ; PET/ITO substrate	K-bar coating Bottom: ITO Top: evaporated Au/Pt	(Randles) C/A ~ 2.72 pF/mm^2	~7.57
10.1021/acsnano.9b04337	hBN + propylene glycol as secondary solvent + HPMC binder Kapton substrate	AJP Bottom: evaporated Cr/Au Top: AJP AgNW	Overlap area ~0.664 mm^2	~3.01
http://dx.doi.org/10.1063/1.4958858	Graphene (NMP) + hBN (IPA) PET substrate	Inkjet-printed graphene electrodes Spray coated hBN	(RC circuit) Rser~125kohm C/A ~ 0.245 nF/cm^2	~2.25
10.1038/s41467-017-01210-2	Ag/hBN/Ag PET substrate coated with SiO2 np	DoD ink-jet printer	Overlap area ~ 500um^2 t=1.2 um C/A ~ 8.7 nF/cm^2	Not reported
10.1109/LMWC.2013.2264658	Polymers SU-8 (photoresist) and PVP Flexible polymide substrate	Dimatix DMP-2800 ink-jet printing Bottom+top: Cabot CCI300 silver nanoparticle ink printed and cured at 120 C	SU-8 shows C~20pF PVP ~ 50pF for same A Quality factor between 4 – 8	Not reported
https://doi.org/10.1021/acsaelm.9b00500	hBN in 2-butanone	Electrophoretic deposition of hBN Evaporation of Al ITO/hBN/Al	175 nF/cm^2 Phase stable at 87 degrees	5
https://doi.org/10.1016/j.ensm.2	Water based, additive free MXene as electrodes GO ink as solid state flex polymide substrate	All ink-jet printed SSC and MSCs	High C/A, good cycling, supercaps, specific cap can be changed by addition of liq electrolytes.	Not reported

Figure 4.7: Literature table comparing various publications specifically on printed electronics using solution processed 2D dielectric nanomaterials

Chapter 5

All-Printed Capacitors from BiOCl nanosheets

5.1 Introduction

With the rapid progress seen in solution processed 2D nanomaterial research, the field of printed electronics is more accessible than ever. The liquid-phase exfoliation (LPE) of layered crystals has been integral to this shift, from generating and characterising nanosheet dispersions to the refinement of functional inks suitable for printing [77, 119, 131]. A whole host of nanomaterials with varying electronic properties have been made available in an ink form that can be easily deposited on rigid or flexible substrates via several printing techniques [341, 403, 404]. The learnings from exfoliation studies, combined with rheological tuning have allowed nanosheet inks to be developed and facilitated rapid growth in printed devices, from early photodetectors to complex devices such as transistors that involve multiple processing steps [64].

However, there is a challenge in constructing all-printed vertically stacked heterostructures made from 2D nanomaterial films. One of the main issues being that 2D nanomaterial networks are quite porous and contain discontinuities within the film, called pin-holes. These pin-holes could lead to electrical shorting by creating undesired contacting between adjacent layers. Another difficulty that arises during multiple layer-on-layer depositions is re-dispersion. This leads to non-uniform and poorly defined interfaces and could result in shorting. These issues underscore the importance of finding dielectric 2D materials that can form robust films so as to sufficiently insulate vertically stacked networks and enable multiple layer printed heterostructures. Thus, it is not surprising that the increase in reports of fully printed transistors using 2D materials has necessitated a parallel growth in investigation into printed dielectrics [67, 332, 333].

Dielectric network properties are typically investigated using a vertical parallel-plate capacitor design [63, 64]. This allows features such as dielectric constant and strength to be evaluated and most importantly, allows the minimum thickness of a continuous network to be found as devices will short when pin-holes are present. So far, hBN has been the main dielectric material that has been explored and incorporated into printed structures [63, 78, 223, 286, 405]. This is primarily due to its structural similarity to graphene and wide availability. However, hBN presents several difficulties. For one, hBN films have a low permittivity of 3-6. Furthermore, hBN has a density of $2.1\,g/cm^3$, making its powder density substantially lower. This causes it to be frustrating to handle and requires large quantities for exfoliation. The low density also translates into poor

quality films that are brittle and highly porous, leaving them open to redispersion and pinholes. Considering these factors, making an all-printed device out of binder-free hBN films is extremely challenging. Some works have incorporated binders or polymers into the hbN inks, but that compromises the purely 2D nature of the printed device. Thus, there is a clear gap in the field that requires further exploration of dielectric materials.

Thin films of high-κ dielectrics grant superior performance in silicon devices and allow lower operating voltages [406]. In addition, a high dielectric constant means the charged impurities and defects are more effectively screened [407]. Going by this, a similar strategy can be applied to layered crystal networks, where thin films of high dielectric constant materials can be used in printed electronic devices. Given the inverse scaling of the dielectric constant with the band-gap [406], there are a range of materials that may be suitable for use as alternative dielectrics. In this vein, we introduce bismuth-oxychloride as a viable option for all-printed heterostructure devices.

In this work, we report the liquid-phase exfoliation of $BiOCl$ for the first time. We demonstrate the exfoliation of $BiOCl$, characterise the resultant nanosheets, and optimise the dispersions for printing. Here, we use an aerosol-jet printer (AJP) to deposit both graphene and $BiOCl$ inks to create vertically stacked capacitors. We then characterise these structures using impedance spectroscopy to extract the dielectric constant and find the minimum insulating thickness where a continuous network is formed. We report a material dielectric constant of ≈ 41 and a dielectric strength of $0.67\,MV/cm$ with a pin-hole free network obtained at a thickness above $1.6\,\mu m$. Interestingly, our data suggests the presence of a second series capacitance, which we propose originates at the inter-sheet interfaces within the electrode networks.

5.2 Experimental Procedure

Graphite powder was sourced from Asbury (Grade 3763) and $BiOCl$ powder from Sigma-Aldrich. The graphite was first pre-treated by tip sonication 450 W) in 80 mL of N-methyl-2-pyrrolidone (NMP) at 40 mg/mL for 1 h, followed by a short centrifugation at 3218g. The supernatant containing the soluble impurities was discarded and the sediment was redispersed in 80 mL of fresh NMP and tip-sonicated for a further 6 h at 450 W power. The $BiOCl$ bulk powder did not require pre-treatment due to its purity and was directly tip-sonicated in 80 mL of NMP at 20 mg/mL concentration for 4 h and 450 W power. Both the dispersions were size-selected through a two-step liquid cascade centrifugation technique. They were first centrifuged at 106g for 90 min, and the sediment containing large un-exfoliated material was discarded. The supernatant from this run was centrifuged at 3830g for 90 min, and the corresponding sediment collected.

The concentration of the resulting dispersions was measured using a vacuum filtration method where $1\,ml$ of the dispersion was filtered through a PETE membrane whose weight was recorded prior to filtration. By subtracting the weight after filtration and the weight before filtration, we can deduce the mass per $1\,ml$ of the dispersion. In this way, the collected sediment of graphene was redispersed in triethylene glycol monomethyl ether, MTG at 1.5 mg/mL and the collected $BiOCl$ sediment was redispersed in IPA at 3 mg/mL. UV - visible spectroscopy was performed using a Varian Cary 5000 to optically characterize the exfoliated nanosheet dispersions. The wavelength was scanned between 800 and 200 nm, and a 4 mm path length-reduced volume quartz cuvette was used for the measurement. Raman spectroscopy was performed on the liquid $BiOCl$

dispersion using a Horiba Jobin Yvon LabRAM HR800 with a 532 nm excitation laser in air under ambient conditions. The spectra were collected by a 100x objective lens (NA = 0.8) and dispersed by 600 g/mm at 25% of the laser power (9 - 5 mm). Bright-field TEM images representative of the standard dispersion of $BiOCl$ were captured using a JEOL 2100, operated at 200kV. The morphology of a vacuum-filtered film of $BiOCl$ flakes was studied through scanning electron microscopy carried out using a Zeiss Ultra Plus SEM using a 2 kV accelerating voltage and 30 um aperture.

The films were deposited using an aerosol-jet printer from Optomec. A 150 μm nozzle was used, and the sheath and carrier flow rates were set to ≈ 45 and $\approx 25\, sccm$ respectively, giving a focusing ratio of 1.8. The platen temperature was set at $80^\circ C$ for IPA-based inks and $100^\circ C$ for MTG-based inks, and all of the printing was carried out at a 1 mm/s platen speed. The coolant temperature was kept between $20^\circ C$ and $25^\circ C$. The film geometry was drawn in AutoCAD and converted to a code that was fed into the Optomec software. The graphene bottom electrode (roughly 7 $\times$ 0.3 mm^2) was printed onto an alumina coated polyethylene terephthalate (PET) substrate designed to minimize droplet wetting. A total of 25 passes were deposited to ensure the film has bulk-like characteristics. The $BiOCl$ layer was deposited over the bottom electrode in 0.7 $\times$ 0.7 mm^2 boxes of varying pass numbers. The top graphene electrode (roughly 0.1 $\times$ 7 mm^2) was then deposited over this dielectric layer by performing a total of 30 passes to ensure it had adequately coated the underlying dielectric layer and reached bulk-like characteristics. At each stage of the vertically stacked heterostructure, the film was annealed overnight in a vacuum oven at $80^\circ C$ to remove trapped solvent.

The thickness and roughness of the printed films was measured using a Dektak 150 Stylus Profiler. A typical optical flat-bed scanner was used to obtain scanned images of the films for optical transmission data from the printed films. Preliminary electrical characterisation was done by simple IV measurements using a Keithley 2621A to confirm capacitor behaviour. Impedance spectroscopy was then performed using a Gamry Reference 3000 to characterise the printed capacitors. Finally, breakdown strength measurements were carried out using a Keithley 4200-SCS Parameter Analyser where the voltage was increased starting from $0.1\, V$ in steps of $1\, V$ until a spike in the current is measured. The voltage at which this occurs is defined as the breakdown voltage of the film.

5.3 Results and Discussion

Material Characterisation

Bismuth oxychloride is an inorganic crystal consisting of alternating layers of Cl^-, Bi^{3+} and O^{2-} ions as seen in Figure 5.1A [408]. The presence of layered structures can be clearly seen in the SEM image of the bulk unexfoliated powder in Figure 5.1B. As described in the Experimental Procedures section, $BiOCl$ was exfoliated into 2D nanosheets in NMP via well-established probe sonication [128, 409, 410] to give a white coloured dispersion, as seen in Figure 5.1C. This dispersion, that has not undergone size-selection and consists of nanosheets of varying sizes is called the standard sample.

UV-vis spectroscopy was carried out on the standard sample to obtain its extinction spectrum. As seen in Figure 5.1D, the extinction response is fairly featureless and decays as a power law at high wavelengths. As dispersions of insulating 2D materials exhibit large scattering [408], the extinction spectra was split into its inherent absorption and

scattering components with the help of an integrating sphere [403, 411]. The absorption spectrum has a clear band-edge at $340 - 360\,nm$ which corresponds to a band-gap of 3.5 eV, validating its insulating behaviour [412]. The extinction spectra is completely dominated by the scattering component above $\approx 350\,nm$ and decays with wavelength as a power law with exponent close to -2.

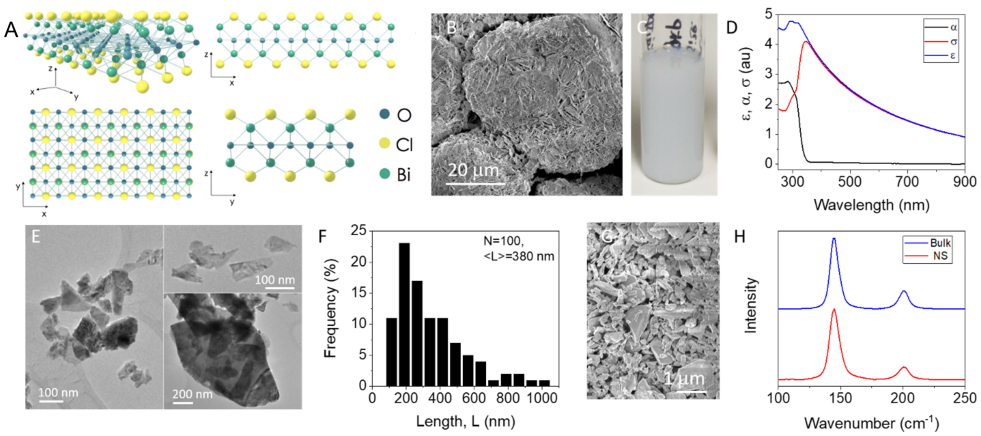

Figure 5.1: Liquid exfoliation of $BiOCl$. A: Structure of $BiOCl$. B: SEM image of $BiOCl$ powder. C: Photograph of a "standard sample" dispersion of $BiOCl$ exfoliated in NMP. D: Extinction, absorption and scattering coefficient spectra of a "standard sample" dispersion of $BiOCl$. E-F: Example TEM images of $BiOCl$ nanosheets (E) and a histogram showing nanosheet length (F). G: An SEM image of a film of $BiOCl$ nanosheets. H: Raman spectra measured on bulk powder as well as on a nanosheet film similar to that in G.

The TEM images taken of the standard sample show clear evidence of 2D nanosheets as seen in Figure 5.1E. The length of a nanosheet is defined as the longest measured dimension. The lengths of the observable nanosheets were measured and plotted as a histogram as shown in Figure 5.1F. The standard sample contains a broad lognormal distribution of nanosheet sizes with a mean length of $< L >= 380\,nm$. Figure 5.1G shows an SEM image of a vacuum filtered film of a standard sample of $BiOCl$. The film consists of a disordered arrangement of platelets. In order to confirm that the insulating nature of the material remains unchanged by the LPE process, Raman spectroscopy was carried out on LPE $BiOCl$ nanosheets as well as a spectrum from bulk $BiOCl$ powder. As seen in Figure 5.1H, the two spectra are virtually identical.

Exfoliation studies were carried out on the $BiOCl$ dispersions by varying certain aspects of the exfoliation procedure. Firstly, the effect of initial powder concentration on the final concentration of nanosheets in dispersion was tested. This was followed by a sonication time study on the final dispersion concentration and lastly, a $BiOCl$ dispersion was monitored over several hours for a time stability study. In each case, the different dispersions were characterised by UV-vis spectroscopy. Backes et al. have shown that an increase in spectral intensity is indicative of an increased concentration of dispersed nanosheets [403]. With this in mind, we shall now discuss the results of the exfoliation studies.

$BiOCl$ was exfoliated in NMP with starting concentrations of 1, 5, 10, 20, 50 and 70 mg/ml. The same exfoliation procedure that is detailed in the Experimental Procedure

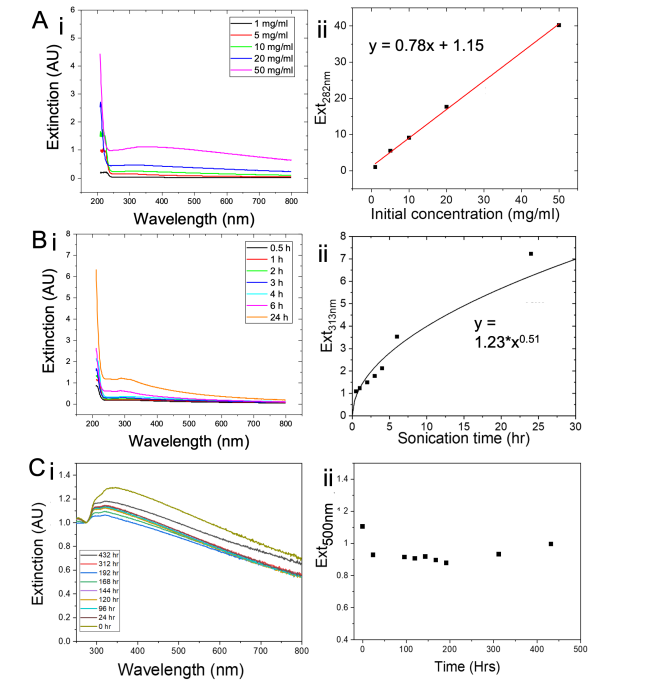

Figure 5.2: A(i): Extinction spectra measured for different concentrations of $BiOCl$ precursor. A(ii): Linear relationship between yield of exfoliated material and initial concentration of $BiOCl$ precursor. B(i): Extinction spectra of precursor $BiOCl$ sonicated for different time durations. B(ii): Extinction at 313 nm plotted against sonication time showing the effect of nanosheet concentration in dispersion with increased sonication times. C(i): Extinction spectrum of $BiOCl$ dispersion over time. C(ii): Extinction at 500 nm vs time.

section was applied to each sample. The results of the initial concentration study are shown in Figure 5.2A(i). When the extinction spectra for each dispersion are plotted together, the spectral intensity is seen to increase with the initial $BiOCl$ concentration, indicating a higher concentration of dispersed nanosheets. [403]. The value of extinction at 282 nm was extracted for each dispersion and plotted against initial concentration as seen in Figure 5.2A(ii). A linear relationship is seen, however it is limited to a threshold concentration, past which the powder does not undergo exfoliation due to saturation of the precursor. Note, the 75 mg/ml sample is missing from the data for precisely this reason. Large amounts of unexfoliated sediment was observed after sonication.

Similarly, to study the effect of sonication time on the final dispersion concentration, $BiOCl$ powder was exfoliated for sonication times of 0.5, 1, 2, 3, 4, 6 and 24 h in NMP, otherwise following the same exfoliation procedure. As seen in Figure 5.2B(i), the intensity of the peaks in the extinction spectra is seen to increase with increasing sonication time, indicating a higher concentration of nanosheets being produced. The extinction value at 313 nm was plotted against sonication time as shown in Figure 5.2B(ii). This wavelength was chosen since there is feature visible at $313\,nm$ which allows us to directly compare the spectra. The relationship is not linear but represented by the curve $y = 1.23x^{0.51}$. This square-root dependence, where the concentration of the final dispersion saturates on increasing the sonication times is widely observed [120, 141, 413, 414].

Finally, the stability of a $BiOCl$ nanosheet dispersion was assessed over time. An

extinction spectra was taken after specific time intervals as seen in Figure 5.2C(i). The overall shape of the spectra remains largely unchanged, indicating no change in the chemical behaviour of the dispersion. However, there is a systematic reduction observed in the spectra over time which could indicate degradation and reaggregation. Figure 5.2C(ii) shows the extinction value at 500 nm plotted against time to be relatively stable, with little change over several hours. Here, the extinction value at $500\,nm$ was chosen since it displays no prominent feature in the spectra, allowing us to track the stability of the dispersion with certainty.

TEM analysis was performed on the graphene ink. Figure 5.3A shows a TEM image of typical graphene flakes. A histogram showing the distribution of flake sizes is seen in Figure 5.3B with a mean length of $< L >= 360 \pm 20\,nm$. Raman spectroscopy was performed on the graphene nanosheets to extract information about nanosheet thickness using the metrics developed by Backes et al. where they relate the variation of the 2D/G band intensity and 2D-band shape with nanosheet thickness [404]. Figure 5.3C shows the obtained Raman spectra for the graphene ink, giving an average nanosheet thickness of N = 12 monolayers.

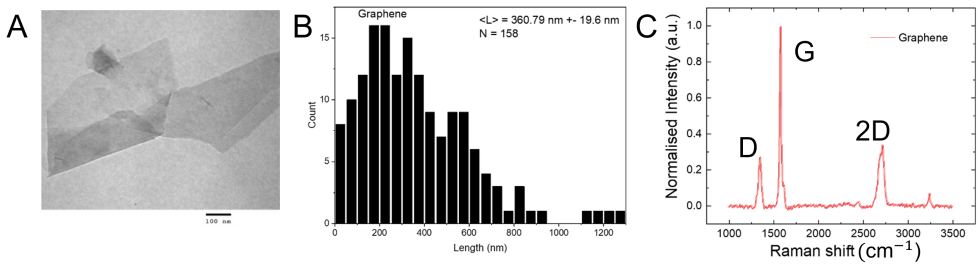

Figure 5.3: A: TEM image of graphene flakes. B: Histogram showing average the nanosheet length. C: Raman spectrum of graphene ink showing the characteristic D, G and 2D peaks.

Device Fabrication

It is essential in electronic devices that insulating films that are pin-hole free and have desirable dielectric properties such as high permittivity and breakdown strength can be produced [63, 78, 286]. In order to characterise films of $BiOCl$, vertically stacked parallel-plate capacitors were fabricated in the geometry shown in Figure 5.4A. Using solution processed inks of graphene and $BiOCl$, we sequentially printed nanosheet networks in a capacitor configuration. The networks were deposited using aerosol-jet printing (AJP).

The bottom electrode was printed using a graphene ink that was prepared using the procedure outlined in the Experimental Procedure section. The graphene was exfoliated in NMP but then solvent transferred to MTG. This technique of transferring material to a different solvent for printing after exfoliation in a solvent with well-matched solvent parameters is quite common [64, 223, 411]. It is usually done when the solvent used for exfoliation is not suitable for the printing method, or the substrate used. In our case, where the device fabrication is performed in open-air conditions, the highly toxic nature

of NMP makes it unusable. However, NMP consists of polymerised by-products that adsorb onto the nanosheet surface [415] and allow the material to be dispersed at higher concentrations when transferred to poorly matched solvents such as alcohols.

We initially transferred the NMP-exfoliated graphene into IPA at a concentration of $0.5\,mg/ml$ but the resultant printed features were discontinuous (and hence of low conductivity, $< 1\,S/m$). Furthermore, the ink was found to steadily accumulate in the mist line resulting in large drops destroying the prints. Inspired from commercial silver inks, which can print for a full day without similar accumulation, we transferred the NMP-exfoliated graphene into MTG also at $0.5\,mg/ml$. This allowed for long deposition times (at least $8\,h$) and resulted in continuous networks. SEM images shown in Figure 5.4B reveal good horizontal orientation of the flakes. The bottom electrode was printed with dimensions $0.3 \times 7\,mm^2$ and a thickness of 200 nm (W to X in Figure 5.4C). After printing, the bottom electrodes were put into a vacuum oven overnight at $100^\circ\,C$ to remove any residual solvent that would adversely affect the conductivity.

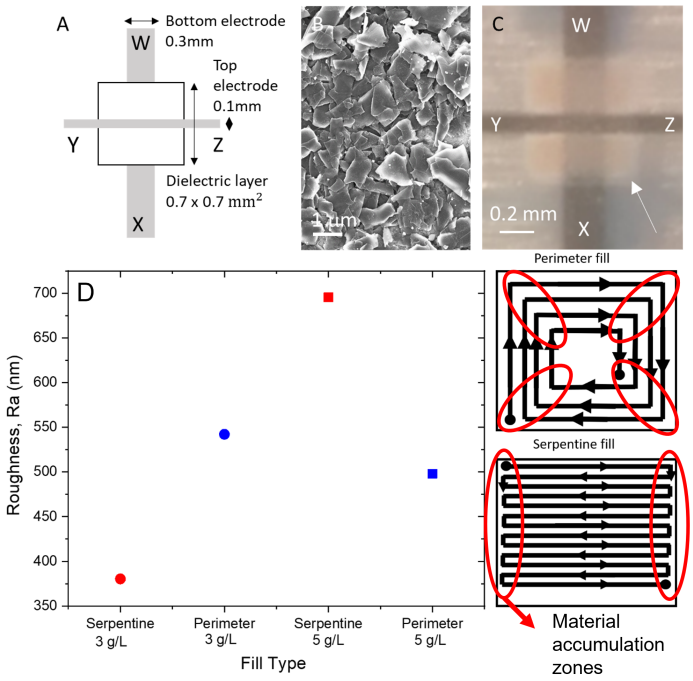

Figure 5.4: A: Schematic showing capacitor structure. B: SEM image of surface of bottom graphene electrode. C: Photograph of printed capacitor. The lines W-X and Y-Z are the bottom and top electrodes respectively which were both printed from liquid exfoliated graphene. The dielectric is the white square in the centre which was printed from $BiOCl$ nanosheets. D: Roughness values obtained for films printed at two concentrations, each filled using perimeter and serpentine fill patterns. Also, schematic showing fill patterns.

The dielectric layer was printed over the bottom electrodes with dimensions of $0.7 \times 0.7\,mm^2$. A feature size large enough to ensure the printing of the top electrode will not lead to any undesirable contacting. We found that the method for filling a rectangular feature also plays a role in the uniformity of the films. There are two fill options with the

Optomec software – serpentine and perimeter. The serpentine fill produces a feature by moving from top to bottom in a snake-like fashion whereas the perimeter fills from the outside perimeter in like a spiral as seen in Figure 5.4D. The perimeter fill leaves ridges in the film where material accumulates as the nozzle spirals inwards during filling. The serpentine fills leaves ridges at the edges of the feature. This is represented by the red circles in Figure 5.4D. Films of the same thickness ($\approx 3\,\mu m$) were deposited and their uniformity was measured using a profilometry scan. The roughness, R_a was calculated by the program as the root mean square (RMS) of the surfaces measured microscopic peaks and valleys. By dividing the R_a values for the respective fill pattern with the mean thickness, we can see that the serpentine fill gives more uniform films (11%) than the perimeter fill (23%). However it should be noted that aerosol-jet printing has a rich parameter space and the fill-pattern is not the only parameter that affects uniformity of the films. Factors such as line width, concentration of the ink, substrate and numerous others can affect film uniformity. At this stage also, the device was put into a vacuum oven overnight at $80°\,C$ to remove any residual solvent that may result in film flattening and contribute to uniformity.

The top electrode was printed using the same ink and printing parameters as for the bottom electrode. The top electrode was printed at a higher thickness of $\approx 250\,nm$ to address the roughness of the $BiOCl$ layer with lateral dimensions of $0.17\,mm^2$. This narrower width was chosen to avoid any undesired contacting between layers in the case where ink spreads or pools during printing. During printing of stacked films, there is a possibility of redispersion of the underlying layer. An advantage of having the two inks in different solvents (MTG and IPA) is that it introduces solvent orthogonality and reduces the risk of redispersion.

Optical Characterisation of AJP Films

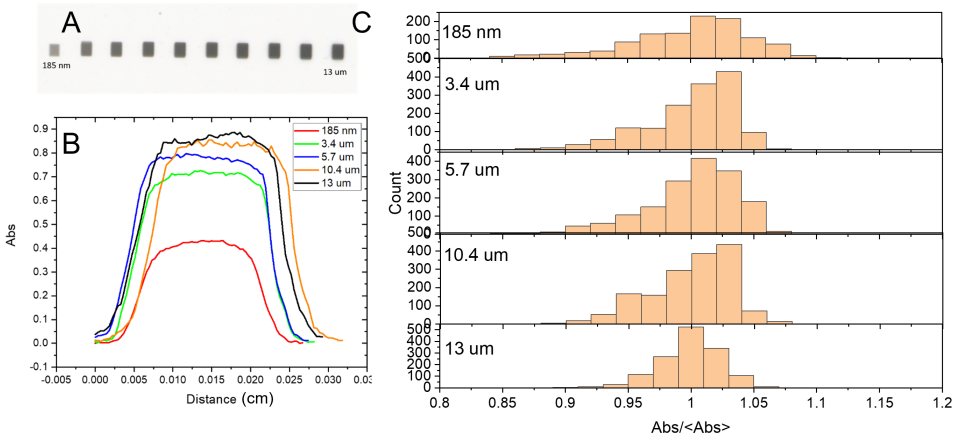

Figure 5.5: A: Scanned image of printed squares of $BiOCl$. B: Absorption line scans for sample thicknesses showing topography of films. B: Histograms of scanned image of films showing increased absorption and therefore filling up of pin-holes as thickness increases

Aerosol-jet printing being a relatively new method of deposition, leaves a lot to be studied in terms of film morphology and the type of networks that are formed. A small characterisation study was performed to understand the uniformity of aerosol-jet printed films through optical transmission data. Ten boxes of $BiOCl$ ranging from thicknesses $185\,nm$ to $13\,\mu m$ were deposited on flexible PET substrate. A scanned image of resolution 6400 dpi was taken using an optical flatbed scanner as shown in Figure 5.5A. In order to analyse the image, the scanner signal from each film was extracted using ImageJ software. The scanner signal was converted into absorption using a calibration curve [179] that was created for the scanner using optical filters of known transmission values. Line scans across the printed films were extracted as shown in Figure 5.5B and histograms were made from the data to show the thickness distribution for each film. Shown below in Figure 5.5C is a sample of the absorption data collected. Considering the resolution of the scanned images is 6400 dpi, using ImageJ we can calculate that each pixel of our scanned images represents $0.2\,mm$. This can be identified as the minimum size of pin-holes that can be detected using this technique. Pin-holes smaller than this size, will lie outside the resolution of this image. The absence of data points at an absorption value of 0 indicated no pin-holes (bigger than $0.2\,mm$) in the films, however measurements past a certain thickness become difficult as the signal starts to saturate due to low transmission.

The absorption data also reveals some information about the uniformity of the films. The narrow distribution in the absorption peaks observed for each printed network implies little variation in thickness across the film, pointing towards uniformity. Furthermore, the distribution gets narrower as the networks get thicker suggesting that the thicker films are more uniform. Thus, optical characterisation of printed networks can be used to collect some morphological information about the films.

Device Characterisation

As the capacitance of a device is inversely related to the thickness, we printed a set of devices with a range of dielectric thicknesses. The dielectric thickness was controlled by increasing the number of print passes over the bottom electrode. As was discussed in detail in Chapter 3, aerosol-jet printing is a highly complex process with several variables. While the constitution of the ink and the carrier flow rates can be reliably controlled, the atomisation process is still poorly understood. It is currently not known whether there is preferential atomisation for smaller nanosheets over large, if the atomisation causes secondary exfoliation or even for how long the deposited mass per unit area is constant. However, these are questions to be addressed in later studies. For this work, we kept our variables consistent across devices, but we note that this still results in some currently unaccountable variations. As shown in Figure 5.6A, the relationship between pass number and $BiOCl$ thickness is linear within error and is consistent with a deposition rate of $85 \pm 3\,nm$ per pass.

In order to identify which of the printed capacitors are insulating, we performed some preliminary electrical measurements. I-V measurements of the bottom electrodes were made immediately after printing and annealing, and before the subsequent layers were deposited. A resistance of $100\,k\Omega$ was recorded, which corresponds to a conductivity of $2300 \pm 600\,S/m$, that is consistent with reports on similar LPE graphene films [64, 179, 223]. On completion of the printed device, two types of I-V measurements were made to ensure the capacitors were insulating. First, the resistance of the top electrode, R_{YZ},

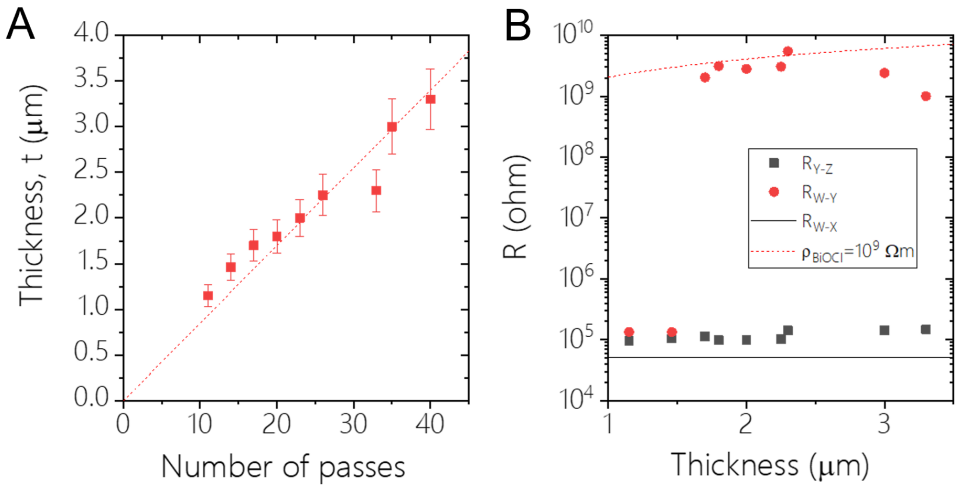

Figure 5.6: A: $BiOCl$ layer thickness as a function of number of print passes. The line is consistent with a deposition rate of $\approx 85\,nm$ per pass. B: Two-probe resistance measured both through the dielectric layer (R_{W-Y}) and across the top electrode (R_{Z-Y}) as a function of dielectric thickness. The resistance across the bottom electrode (R_{W-X}) is shown for comparison. The dashed line plots the dielectric resistance assuming a dielectric resistivity of $\approx 10^9\,\Omega m$.

was measured to ensure the graphene network had reached a bulk-like conductivity in agreement with the bottom electrode. A second resistance was measured between the top and bottom electrode, R_{WY}, to determine if the dielectric layer is insulating where we define the dielectric layer as sufficiently insulating if $R_{WY} \geq 10^4 \times R_{YZ}$. As seen in Figure 5.6B, the resistance across the top electrode, R_{YZ}, is reasonably constant at $\approx 100\,k\Omega$ across all the thicknesses and matches closely to the resistance of the bottom electrode with a conductivity of $2800 \pm 600\,S/m$.

The two thinnest capacitors, with dielectric layer thicknesses of $0.8\,\mu m$ and $1.1\,\mu m$ yielded a value of $R_{WY} \approx 100k\Omega$ which indicates the devices are shorted. Devices above this threshold thickness display R_WY of a few $G\Omega$, that is equivalent of an open circuit measurement. This implies that the out-of-plane resistivity of $BiOCl$ is at least $10^9\,\Omega m$, which compares to the measured resistivity of networks of $BiOCl$ nanosheets of $10^{10}\,\Omega m$ [416]. Thus, having established the capacitors above a thickness of $1.6\,\mu m$ are insulating we performed impedance measurements in order to characterise the dielectric films made from the newly exfoliated 2D material, $BiOCl$.

Impedance Measurements

Impedance spectroscopy is a useful method of characterising capacitors since the measured frequency dependence of impedance can be fit to circuit models that best match the data. In our case where it is important to identify pin-holes in the film, such circuits can be used to identify parallel resistances that are consistent with current leakage in capacitors.

We performed impedance measurements on the graphene/$BiOCl$/graphene stacks

for a range of $BiOCl$ network thicknesses between $1.15\,\mu m$ and $3.3\,\mu m$. An AC voltage is applied over a range of angular frequencies, ω and the associated current measured. This current is shifted from the voltage by a phase shift, θ. As detailed in Chapter 4, AC impedance is a complex quantity that can be written as $Z = |Z|\cos\theta + i|Z|\sin\theta = Z_{re} + iZ_{im}$

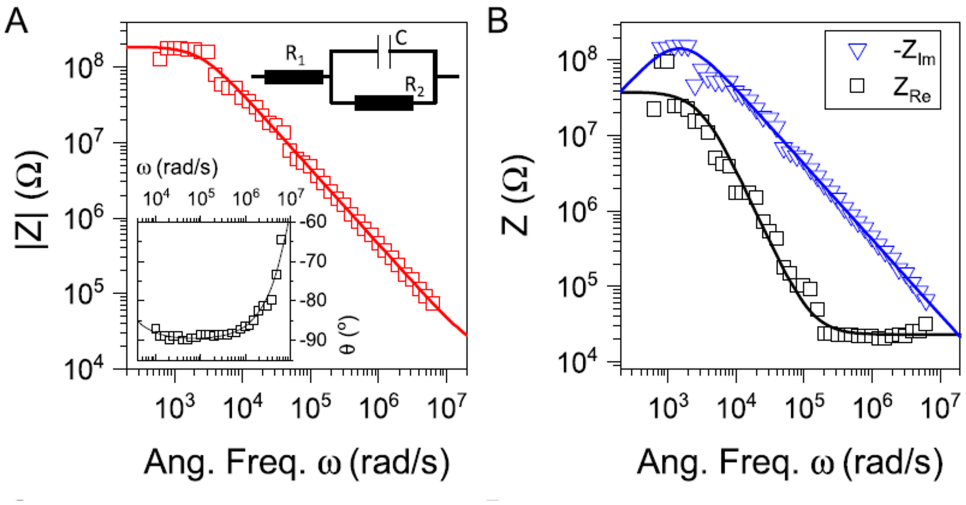

Figure 5.7: Impedance analysis of printed capacitors. A: Modulus, $|Z|$, and phase θ (bottom inset) as a function of frequency for a typical ($t = 2.3\,\mu m$) capacitor. Top inset: Randles circuit used for fitting. B: Real and imaginary components of the impedance measured for printed capacitors. In A and B, the lines are fits to Eqt. 5.1 and 5.2.

Shown in Figure 5.7A is the impedance spectrum, $|Z|$ vs ω for a representative capacitor of thickness $2.3\,\mu m$ and overlap area $0.3 \times 0.1\,mm^2$. It should first be noted that for all the samples, the data from $|Z|$ and Z_{im} were fitted as they were generally the most noise-free, whereas the θ and Z_{re} data tended to be noisier. The modulus of impedance for a Randles circuit, $|Z|$ is characterised by a plateau at low angular frequency followed by an ω^{-1} decay at higher frequencies. Shown in the inset of Figure 5.7A is the phase versus angular frequency. The phase, θ is $\approx -90°$ over the middle range of the frequencies, but falls off at both low and high frequencies. The plateau seen in the $|Z|$ vs ω spectra as well as the tapering off of phase at low and high frequencies are indications of resistances in the system.

The real (Z_{re}) and imaginary components (Z_{im}) of the impedance are plotted vs ω in Figure 5.7B. The imaginary component of impedance closely resembles the modulus, showing this component to be dominant, emphasising the capacitive nature of the system. The real impedance transitions between plateaus at low and high frequencies via an ω^{-2} decay at intermediate frequencies. This transition is also evidence for the presence of series and parallel resistances in the system. Keeping in mind these behaviours, we can suggest that the graphene/$BiOCl$/graphene stacks are electrically equivalent to a capacitance (C) combined with series (R1) and parallel (R2) resistors as shown in the inset in Figure 5.7A. This model is called a Randles circuit and as discussed in Chapter 4 the impedance can be represented as

$$Z_{Randles} = R_1 + \frac{R_2}{1+(\omega R_2 C)^2} - i\frac{\omega R_2^2 C}{1+(\omega R_2 C)^2}$$

where

$$Z_{re} = R_1 + \frac{R_2}{1+(\omega R_2 C)^2} \tag{5.1}$$

and

$$Z_{im} = \frac{\omega R_2^2 C}{1+(\omega R_2 C)^2} \tag{5.2}$$

In addition, these equations can be combined to yield fitting equations for $|Z|$ and θ using

$$|Z| = \sqrt{Z_{re}^2 + Z_{im}^2} \tag{5.3}$$

and

$$\theta = \tan^{-1}\frac{Z_{im}}{Z_{re}} \tag{5.4}$$

The data from $|Z|$, Z_{re} and Z_{im} were fitted using the above equations yielding reasonable fits in all cases. However, it should be noted that most of the phase curves were too noisy to be fitted. From Eqn 5.2, we can see that the values of C and R_2 can be extracted from the fit of Z_{im}. The most reliable fit data for R_1 however came from the Z_{re} versus ω curves due to the presence of the high frequency plateau which pins down the value of R_1 in the fit. In addition, to illustrate the dependence of θ on ω, we have used Eqt. 5.4 coupled with the values of C, R_1 and R_2 found from fitting the other data sets to plot the black line in Figure 5.7A(inset). This curve clearly illustrates the deviations from $\theta = -90^\circ$ at low and high frequencies which are due to the presence of parallel and series resistances respectively.

The values of R_1 and R_2 have a physical significance in our printed capacitor systems. The series resistance R_1 represents the electrode resistance which in our case is graphene. The parallel resistance R_2 represents pin-holes in the systems and therefore any current leakage between the two electrodes. The effect of these two resistances is most clearly seen in the Z_{re} versus ω plot in Figure 5.7B. The height of the plateau seen at low frequency is the sum of R_1 and R_2 whereas the height of the plateau seen at high frequency is the value of R_1.

Figure 5.8A shows the values of R_1 and R_2 plotted against thickness of the $BiOCl$ films. We find that this graph is quite similar to that in Figure 5.6B. The series, R_1, is of similar magnitude to the resistance across the top electrode, R_{Z-Y}, while the parallel resistance, R_2, is of similar magnitude to the resistance through the dielectric layer, R_{W-Y}. In addition, we find that while R_2 is very large ($> 10^8\,\Omega$) for $BiOCl$ thicknesses above $1.6\,\mu m$, the two samples with the thinnest dielectric layers display much lower values of R_2, consistent with the presence of pinholes.

In the case of a simple capacitor, we expect the the capacitance to scale linearly with thickness of the dielectric film as $C/A = \epsilon_0\epsilon_r/t$. Shown in Figure 5.8B are the capacitance values obtain from the Randles circuit fits that have been normalised to overlapping electrode area and plotted against the inverse of thickness. We see a monotonic

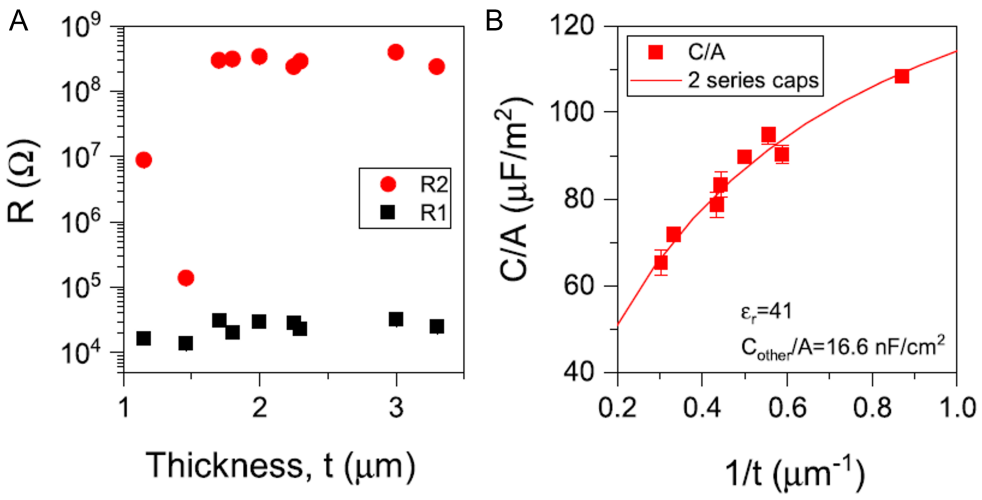

Figure 5.8: A: Parallel (R_2) and equivalent series (R_1) resistances plotted versus dielectric thickness. B: Areal capacitance plotted versus inverse dielectric thickness. The line is a fit to Eqt. 5.7.

increase of C/A with $1/t$, however there are two abnormalities. First, there is clearly some curvature in the data set and second, the data is not consistent with a straight-line through the origin. This can be explained if we consider the measured capacitance to being equivalent to a series combination of two capacitors: one of which is thickness independent, which we will call C_0 and one which scales normally with dielectric thickness, $C(t)$. We can write

$$\frac{1}{C} = \frac{1}{C_0} + \frac{1}{C(t)} \tag{5.5}$$

where

$$C(t) = \frac{\epsilon_0 \epsilon_r A}{t} \tag{5.6}$$

It is easy to see by inserting Eqt. 5.4 into 5.3 that,

$$\frac{C}{A} = \frac{\epsilon_0 \epsilon_r / t}{1 + \frac{\epsilon_0 \epsilon_r / t}{C_0 / A}} \tag{5.7}$$

Here, ϵ_r is the dielectric constant associated with the $BiOCl$ network. We find this equation fits the data in Figure 5.8B very well if $\epsilon_r = 41 \pm 3$ and $C_0/A = 16.6 \pm 1.4\, nF/cm^2$. Assuming the porosity of the BiOCl network is $\approx 50\%$, this value implies an intrinsic dielectric constant of ≈ 80 which is somewhat higher than the theoretical permittivity of bulk $BiOCl$, which is $\approx 50 - 60$ [90, 412, 417]. This difference in permittivity of printed films when compared to bulk could be a result of factors such as lower porosity, flake orientation and electrode coverage. As far as we know, this is the highest reported value of ϵ_r in the field of printed electronics. The majority of work in printed dielectric films using 2D nanomaterials has been focused on hBN and depending

on the method of deposition, the permittivity of these films range only between 3 and 6 [63, 223, 418]. Other papers have shown the use of montmorillonite, a commonly found layered silicate, to fabricate capacitors through the layer-by-layer assembly process giving dielectric constant of 5.7 [67].

In order to explain the origin of the series capacitance C_0/A, we consider the inter-nanosheet junctions within the graphene electrodes [323]. As has been proposed for inter-nanotube junctions [419] it is possible that nanosheet-nanosheet junctions act as parallel capacitor-resistor combinations. Then, the graphene electrode would display a capacitance which was due to the network combination of all of the inter-nanosheet capacitances. We can model the graphene electrode as a set of stacked layers, each one nanosheet thick and separated by a distance $\lambda = 1\,nm$. Given the combined thickness of both electrodes is $\approx 500\,nm$ and each graphene sheet is $\approx 4\,nm$ thick, the pair of electrodes are ≈ 100 layers thick. Thus, the capacitance associated with the interlayer junction is $C/A = \epsilon_0\epsilon_r/\lambda$. It follows then that the capacitance of n stacked (i.e. in series) layers is $C_n/A = \epsilon_0\epsilon_r/n\lambda$. Taking $\epsilon_r = 1$ (for air), $n = 100$ and $\lambda = 1\,nm$, we get a capacitance $\approx 10\,nF/cm^2$ which is very close to the measured value of $16.6 \pm 1.4\,nF/cm^2$.

It is important to ask why this "internal capacitance" has not been observed before, for example in previous printed capacitors with graphene electrodes. If we consider Eqt 5.5, a series combination of C_0 and $C(t)$ yields $C = C(t)/(1 + C(t)/C_0)$. This only deviates from $C(t)$ if $C(t)/C_0$ is large enough. Here, $C(t)$ i.e. the $BiOCl$ capacitance is large due to its high permittivity and could be the reason we see the influence of the internal capacitance C_0.

5.3.1 Dielectric Breakdown Measurements

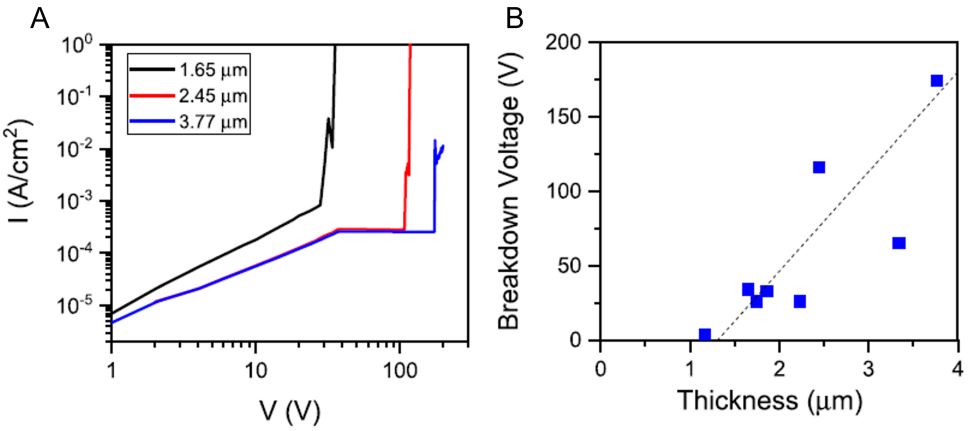

Figure 5.9: Dielectric breakdown strength of $BiOCl$ capacitors. A: Current density versus voltage curves for three different $BiOCl$ layer thicknesses. B: Breakdown voltage plotted versus $BiOCl$ layer thickness. The dashed line represents a breakdown strength of $0.67\,MV/cm$.

We have measured the breakdown strength of our graphene/$BiOCl$/graphene capacitors. Figure 5.9A shows the out-of-plane (i.e. R_{W-Y}) current density versus voltage

curves measured for capacitors of three thicknesses. In all cases, we see a quasi-linear increase in the current density up to the breakdown voltage, above which the current density increases rapidly. Figure 5.9B shows the breakdown voltage plotted against the $BiOCl$ layer thickness. Interestingly, this graph implies the breakdown voltage to be extremely small for dielectric thicknesses below 1 - 1.5 μm. However, above this critical thickness, the breakdown voltage increases linearly with layer thickness. This critical thickness is very similar to the thicknesses below which R_{WY} and R_2 rapidly fall off. This suggests that the very low breakdown voltages indicated by Figure 5.9B for thin $BiOCl$ films are associated with the presence of pinholes. Once the capacitors become pinhole-free, the linear increase of breakdown voltage with thickness (dashed line) implies a breakdown strength of $0.67\,MV/cm$. This value is lower than those measured for liquid-exfoliated BN nanosheets ($\approx 2.5\ MV/cm$) [78, 131] and BN/polymer composites ($3\,MV/cm$) [418]. In part, the break-down voltage is lower in $BiOCl$ compared to that in BN because of the smaller band gap of the former material [420]. However, it is likely that the low dielectric strength is also partly associated with the presence of defects within the nanosheets. We speculate that edge defects, which are thought to be prominent in all liquid-exfoliated nanosheets, may play a significant role.

5.4 Conclusions

In summary, we have demonstrated the liquid phase exfoliation of a new layered insulating material, $BiOCl$ to give a stable dispersion of 2D nanosheets. Through extinction spectroscopy, we see the data is consistent with insulating behaviour showing an optical gap of $3.5\,eV$. We then show how a dispersion of $BiOCl$ can be easily tailored to be aerosol-jet printed into thin, pin-hole free insulating films that are integral in the field of printed electronics. We demonstrate this by fabricating capacitors of graphene-$BiOCl$-graphene and characterising their working to obtain a dielectric constant for $BiOCl$ films. Capacitors with dielectric layer thicknesses ranging from $1.15\,\mu m$ to $3.3\,\mu m$ are printed with films starting to be fully insulating, or pin-hole free, after $1.6\,\mu m$. Impedance spectroscopy performed on the stacked structure revealed the behaviour to be electrically equivalent to a capacitance combined with series and parallel resistors. We find that the data is consistent with the capacitance being equivalent to a series combination of two capacitors, one of which is thickness independent (C_0) and one of which scales normally with dielectric thickness. Fitting the data to this model, we derive a value of relative permittivity $\epsilon_r = 41 \pm 3$ which is currently the highest reported value of permittivity for printed 2D dielectric nanosheet films. We also find some stray capacitance of the value, $C_0/A = 16.6 \pm 1.4\,nF/cm^2$ which is thought to be thickness independent. We speculate that this additional capacitance may be related to the inter-nanosheet junctions.

Chapter 6

Improving Permittivity through BiOCl-Ag Nanoplatelet Composites

6.1 Introduction

Composite materials are generally fashioned to enhance mechanical properties such as strength and flexibility [421–423]. However, they can also be used to change or tune the electrical characteristics of a material. For example, the use of conductive polymer composites that are made up of polymers and metallic fillers in a number of electromagnetic frequency interference (EMI) shields, antistatic devices and conducting coatings [424, 425]. Composite fabrication has the advantages of achieving performance superior to either of its individual components, without altering their chemical and structural identity. Furthermore, the electrical characteristics of a composite can be described by percolation theory. It is a powerful tool that can be applied to investigate the physical properties of heterogeneous materials [426]. Unlike the linear rule of mixtures [427, 428], percolation theory accounts for the dramatic change in a property of the composite upon reaching long range connectivity within the network.

With regards to insulator-conductor composites, polymer nanocomposites made of conducting particles embedded in an insulating polymer matrix have been widely studied [429–431]. This is due to the large increase in dielectric permittivity they exhibit in the vicinity of the conductive filler percolation threshold [432–434]. The sudden increase is attributed to the formation of conducting regions that are separated by small distances within the network. This effect creates local microcapacitors that contribute largely to the permittivity of the material [434]. Studies have even been performed in ceramic-metal composites (CMCs) where metal particles are dispersed in a ceramic matrix, such as $BaTiO_3$ without entering into their lattice structure [435]. Predictably, there has been recent work on conducting polymers or liquid crystal suspensions using nanomaterials such as carbon nanotubes and graphene flakes that display colossal spikes in permittivity close to the percolation threshold [436, 437].

High dielectric permittivity materials are a necessary part of electrical applications, mainly for charge separation purposes [438–441]. With the rise of 2D nanomaterial production through liquid phase exfoliation and its subsequent success in printed electronics, there is a more urgent need for 2D nanomaterial dielectrics with high permittivity and low losses. So far, most of the work done in dielectric films from 2D nanomaterials has been focused on hBN [63, 78, 223, 286, 405]. However, it suffers from low permittivity (3-7) and in most cases requires a binder or additive in order to be deposited into thin

films. Taking inspiration from the high permittivities displayed by polymer-conductive filler matrices and from established works that show 2D nanomaterial networks follow percolation theory [442–445], we propose a 2D:2D nanomaterial composite in the hope that we achieve high permittivity values from its printed films.

We have introduced in the previous chapter a new dielectric 2D nanomaterial, $BiOCl$ that displays a permittivity that is significantly larger than the current 2D dielectric nanomaterial films used specifically in printed electronics [172]. In this work, we fabricate devices out of $BiOCl$ and Ag nanoplatelet (AgNP; note: not to be read as silver nanoparticles) composite films. The $BiOCl$ nanosheets are prepared through liquid phase exfoliation and the Ag nanoplatelets sourced commerically. The composite inks are deposited into devices using a spray-coating technique and their dielectric properties are characterised by impedance spectroscopy.

6.2 Experimental Procedure

Silver nanoplatelet paste, Nanoflake N300 was sourced commercially from Tokusen, USA. Graphite powder sourced from Asbury (Grade 3763) was first pre-treated by tip sonication ($450\,W$) in $80\,mL$ of N-methyl-2-pyrrolidone (NMP) at $40\,mg/mL$ for $1h$, followed by a $1\,h$ centrifugation at 3218g. The supernatant containing the soluble impurities was discarded and the sediment was redispersed in $80\,mL$ of NMP and tip-sonicated for a further $6\,h$ at $120\,W$ power. $BiOCl$ powder, sourced from Sigma Aldrich was pre-treated by tip sonication ($450\,W$) in a $6\,mg/ml$ solution of sodium cholate and DI water at a concentration of $30\,mg/ml$ for $1\,h$. This was followed by a $1\,h$ centrifugation at 3218g to separate out the sediment. The supernatant containing the soluble impurities was discarded and the sediment redispersed in a $2\,mg/ml$ sodium cholate and DI water solution. This was tip sonicated for $6\,h$ at $450\,W$ power for exfoliation. Both the graphene and $BiOCl$ dispersions were size-selected through a two-step liquid cascade centrifugation technique. They were first centrifuged at 106g for 90 min, and the sediment containing large un-exfoliated material discarded. The supernatant from this run was centrifuged at 3830g for $90\,min$, and the corresponding sediment collected.

Once again, the concentration of the resulting dispersions was measured using the vacuum filtration method. In this way, the graphene sediment trapped between 106g and 3830g was redispersed in IPA to give a $0.5\,mg/ml$ dispersion. Similarly, the $BiOCl$ sediment was redispersed in DI water to give a $5\,mg/ml$ ink. The silver nanoplatelet ink was made by diluting the paste to a $5\,mg/ml$ dispersion in DI water. UV- visible spectroscopy was performed using a Varian Cary 5000 to optically characterize the exfoliated nanosheet dispersions. The wavelength was scanned between 800 and $200\,nm$, and a 4 mm path length-reduced volume quartz cuvette was used for the measurement. Bright-field TEM imaging was performed on the standard dispersions of the $BiOCl$ and $AgNP$ inks using a JEOL 2100 operated at $200\,kV$ and a beam current of $107\,\mu A$.

Indium Tin Oxide (ITO) coated ($100\,nm$) glass slides were sourced commercially from Ossila. These glass slides were segmented and certain areas etched away using dilute HCl solution at $50°C$ followed by $NaCl$ solution wash to leave behind a strip of ITO on each glass segment that would behave as the bottom electrode. The glass segments were then cleaned by immersion in Helmanex solution followed by 10 min of sonic bath. This was repeated with IPA to ensure clean substrates. The $AgNP-BiOCl$ films are subsequently sprayed on top of the ITO with Kapton tape used to block areas

so as to leave some of the ITO exposed for electrical measurements. The composite inks of varying $AgNP$ volume fraction were prepared using the $BiOCl$ and $AgNP$ inks using the formula $\phi_{AgNP} = \frac{V_{AgNP}}{V_{AgNP}+V_{BiOCl}}$. They were placed in the sonic bath for 15 min before spray coating to ensure uniform mixing. The films were deposited using a Harder & Steenbeck Infinity Airbrush secured to a Janome JR2300N mobile gantry. $5\,ml$ of the composite ink was sprayed on top of the ITO and annealed in the vacuum oven overnight at $80^\circ C$ to remove trapped solvent. A mask was placed over this middle layer and $15\,ml$ of graphene sprayed over this to form top electrodes. The device was once again annealed overnight in a vacuum oven at $80^\circ C$ to remove trapped solvent. This procedure yields four separate devices for each volume fraction of $AgNP - BiOCl$ ink. The thickness and roughness of the printed films was measured using a Dektak 150 Stylus Profilometer. The morphology of the spray coated composite films was captured using a Zeiss Ultra Plus SEM in the InLens mode using a $30\,\mu m$ aperture and $2 - 5\,kV$ accelerating voltage.

Preliminary electrical characterisation was done by simple I-V measurements using a Keithley 2621A to confirm capacitor behaviour. Impedance spectroscopy was then performed using a Gamry Reference 3000 to characterise the printed capacitors. It should be noted that the data obtained from the devices in this work is much less noisy than that presented in the previous chapter. This is due to significant improvement in the measurement set-up. The impedance spectroscopy was carried out in a Faraday cage that was properly grounded. This vastly improved the signal-noise ratio of the data collected and allowed for accurate fitting.

6.3 Results and Discussion

6.3.1 Material Characterisation

The dielectric - metallic composites are realised through mixing nanosheet inks of bismuth oxychloride and silver nanoplatelets. The $BiOCl$ nanosheets are prepared through liquid phase exfoliation. However, unlike in the previously reported work, the $BiOCl$ ink was prepared by exfoliation in a surfactant water dispersion. This was done in order to prevent the use of any toxic solvents such as NMP since the film deposition takes place in an exposed environment. Consequentially, there is no difference in the resultant nanosheets as we will reveal through the characterisation techniques below.

Figure 6.1A shows the extinction spectrum obtained from UV-vis spectroscopy of the surfactant-exfoliated $BiOCl$ dispersion. The spectrum is identical to that measured from the NMP-exfoliated dispersion presented in the previous chapter. The spectrum is generally featureless as expected for insulating 2D materials and decays as a power law at high wavelengths. The extinction spectrum has been split into its scattering and absorption components with the help of an integrating sphere [403, 411]. For wavelengths above $\approx 350\,nm$, the scattering component largely dominates the extinction response and decays with wavelength as a power law with an exponent close to -2. The absorption component shows a clear band edge at $340 - 360\,nm$ leading to an optical gap of $3.5\,eV$ in line with previous reports [412] and consistent with insulating behaviour.

Figure 6.1B and 6.1C show representative TEM images of the exfoliated $BiOCl$ nanosheets and the commercially sourced Ag nanoplatelets respectively. In both cases, the images reveal the presence of two-dimensional structures with no large 3D objects observed. The $BiOCl$ nanosheets are quite small in size, with the largest being $\approx$

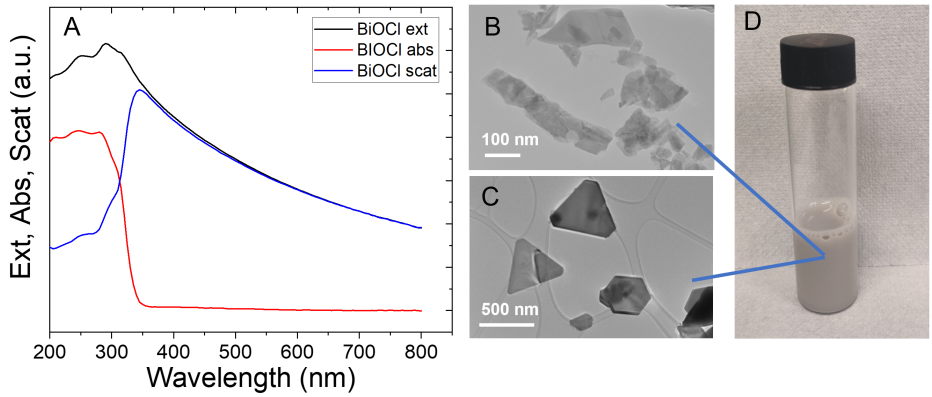

Figure 6.1: A: Extinction spectrum of the surfactant exfoliated dispersion of $BiOCl$ showing scattering and absorption components. B: TEM image of $BiOCl$ nanosheets. C: TEM images of commercially sourced Ag nanoplatelets. D: Image of a $AgNP - BiOCl$ composite ink.

$150-200\,nm$. The Ag nanoplatelets are much larger, with an average size of $\approx 500\,nm$. They are mostly triangular in shape and are expected to be $45\,nm$ thick (as specified by the supplier). Their thickness is also apparent in Figure 6.1C due to the darker contrast. The composite inks are prepared by mixing together the $BiOCl$ and Ag nanoplatelet inks in varying volume fractions as detailed in the Methods section. As seen in Figure 6.1D, the resulting composite ink is grey-ish in colour owing to the presence of silver.

6.3.2 Device Characterisation

The NMP exfoliated graphene was transferred to IPA after size-selection to allow spray coating [64, 223, 411]. The mobile gantry used for spray coating is placed in a fume-hood, but otherwise exposed to air and therefore it is essential that non-toxic solvents be used during deposition. Similarly, the exfoliated $BiOCl$ was transferred from $2\,mg/ml$ sodium-cholate solution to pure DI water. This solvent transfer is done mainly because the back pressure during spraying can cause bubbles to form in the presence of surfactants, leading to non-uniform films. However, the stability of the dispersion is maintained as the surfactant molecules adsorb onto the surface of the nanosheets keeping them from reaggregating [118]. Furthermore, any residual surfactants remaining in the dispersion will help lower the surface tension of water ($\sigma \approx 72\,mN/m$), making it more compatible to be sprayed on glass or ITO ($\sigma \approx 36\,mN/m$). As detailed in Chapter 3, surface energy matching between solvent and substrate leads to better surface wetting and ultimately more uniform film formation.

As as been established previously, the dielectric networks are characterised by incorporating them into a parallel-plate capacitor geometry. At first, an all-printed vertically stacked heterostructure device was attempted. However, we quickly encountered problems with shorting. A spray coated bottom electrode tends to be rough, and any subsequent spraying on top of it results in highly porous and non-continuous films, even for thicknesses on the order of $5\,\mu m$. Thus, by eliminating a printed bottom electrode,

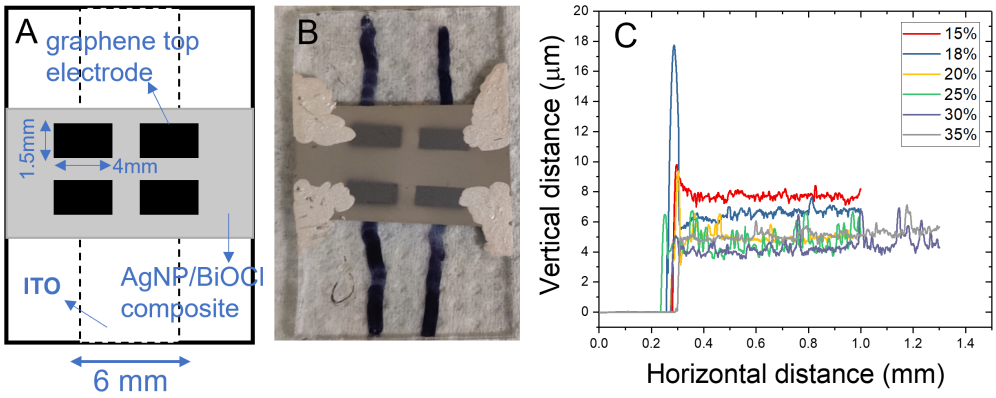

Figure 6.2: A: Schematic showing the geometry of sprayed capacitors. B: Optical image of a $15\% AgNP - BiOCl$ film capacitor. C: Thickness profiles of representative composite films.

we can ensure a uniform and continuous composite film by spraying directly on to ITO. The composite inks are spray coated onto a glass substrate with a strip of exposed ITO that is $100\,nm$ thick, acting as the bottom electrode. Figure 6.2A shows the schematic of a typical batch of devices of one composite loading level. Four graphene top electrodes are sprayed on top of this composite film using a shadow mask. Each batch results in four distinct devices of overlap area $2 \times 1.5\,mm^2$. Composite films ranging from $15\%\, AgNP - BiOCl$ to $40\%\, AgNP - BiOCl$, were deposited as well as a pure $BiOCl$ film (i.e. $0\%\, AgNP$). A representative batch of devices of loading level $15\%\, AgNP - BiOCl$ is shown in Figure 6.2B. Note that the films are grey in colour owing to the presence of Ag nanoplatelets. Silver paint is applied to the graphene electrodes as contacts for electrical measurements.

The thickness of the films were measured using a profilometer and representative thickness profiles are shown in Figure 6.2C. Although each film was prepared by spraying $5\,ml$ of ink, the thickness of each composite film varies over a range of values, typically between $4\,\mu m$ and $9\,\mu m$. This can be partly attributed to substrate placement and alignment during spraying. However, Ag nanoplatelets being of density $10.5\,g/cm^3$ and $BiOCl$ being of density $7.8\,g/cm^3$, the composite inks will vary in mass depending on the loading level which could affect the resultant film thickness. The thickness profiles display a small peak or "lip" at the start of the step seen at $0.3\,mm$. This feature appears when the Kapton tape covering parts of the substrate is peeled off and slightly lifts the edges of the film. As envisioned, by spraying the films directly on ITO, they are generally of low roughness, with R_a between $2 - 5\%$. This is ideal for the subsequent spraying of the top electrode. A mask is placed over the composite film to pattern the top electrodes with feature size $4 \times 1.5\,mm^2$. Graphene ink in IPA is used and $15\,ml$ deposited to ensure the film is in the thickness-independent region of conductivity. Solvent orthogonality is established in the deposition of the two stacked layers, which reduces the risk of redispersion.

As the composite films increase in loading level of Ag nanoplatelets, percolative paths start to form that alters the conductivity of the film. At low loading levels, the Ag

nanoplatelets are few and far between within the film. As the volume fraction of Ag is increased, nanoplatelets reside closer together and can form continuous paths within the film going between the electrodes, allowing conduction. In order to identify when the composite films start to be conducting, simple I-V measurements are performed. A DC voltage is applied between the bottom electrode (ITO) and the top electrode (graphene) and the current response measured. We will discuss this further below.

Figure 6.3A-C show SEM images of composite films of three loading levels. A pure $BiOCl$ film made up of a network of randomly arranged nanosheets is shown in Figure 6.3A. Firstly, it is clear that the $BiOCl$ nanosheets are quite small, with most being $< 200\,nm$ in length. They are quite densely packed and show no pin-holes or gaps within the film. However, the film does not appear uniform but displays "domains" or "dips" that are visible in the SEM image. This is a possible artifact of the spray coated films, where large droplets might have landed on the substrate and caused material displacement during drying. Seen in Figure 6.3B is the SEM image of a $15\% AgNP - BiOCl$ composite film. The black arrows in the image point to Ag nanoplatelets within the network. The nanoplatelets are dispersed within the film as discrete objects. Figure 6.3C shows the SEM image of a $40\% AgNP - BiOCl$ composite film. As depicted by the black lines drawn over the image, the Ag nanoplatelets are much more prevalent within the film and form areas of linked networks that create conductive paths.

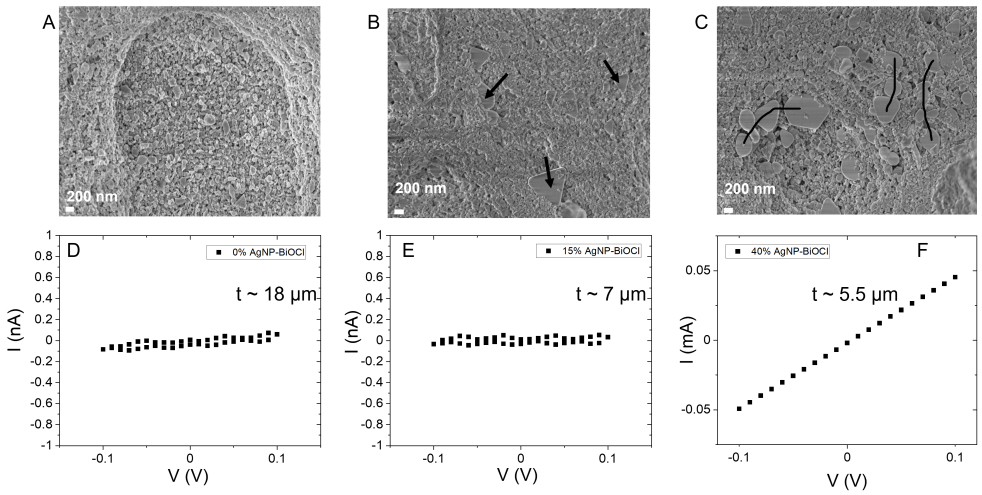

Figure 6.3: A-C:: SEM images of composite films of 0%, 15% and 40% $AgNP$ loading level. D-F: Out-of-plane IV measurements of the respective composite films.

Figures 6.3D-F show the I-V responses of the three composite films. As seen in Figure 6.3 D and E, a voltage scan through $\pm 100\,mV$ yields a current response identical to an open circuit. This implies the insulating nature of the composite film, and thus it can be concluded that there are no conductive paths formed by the Ag nanoplatelets that span the entire composite. Figure 6.3F displays an example of a composite film that has reached percolation. The $40\%\, AgNP - BiOCl$ film conducts $60\,\mu A$ of current when a voltage of $100\,mV$ is applied. It is important to note here that any current conducted by the composite film is due to the conductive paths created by the Ag nanoplatelets, and not by pin-holes or shorts within the system. It was for this reason that thick films were deposited as it would ensure no pin-holes.

As this is a system consisting of different films of varying conductivity, it is useful to establish certain numerical figures to avoid confusion. Figure 6.4A shows the conductivities of the different films in a typical device. The bottom electrode ITO displays a conductivity of $1.78 \times 10^5\, S/m$ and the top graphene electrode a conductivity of $500 S/m$. This is within the expected range of values for sprayed graphene films [446–448]. A composite film that is insulating, i.e. before the Ag nanoplatelets have reached percolation, displays conductivities in the range of $1 \times 10^{-8}\, S/m$. A composite film is considered to have reached percolation when it displays conductivities of $1 \times 10^{-3}\, S/m$ i.e. $\geq 10^4$ times the conductivity before percolation.

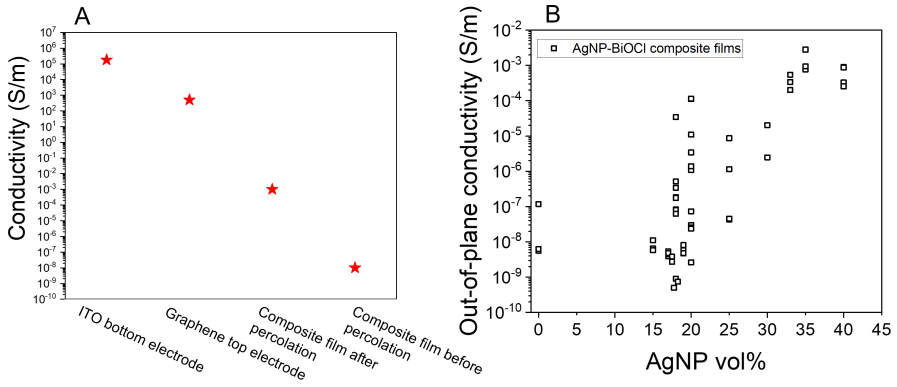

Figure 6.4: A: Conductivities of various films within the device. B: Out-of-plane conductivity of composite films as a function of Ag nanoplatelet loading level.

As mentioned earlier, each batch of a composite film contains four devices. The out-of plane conductivity of each device was calculated from their I-V responses. Figure 6.4B shows the out of plane conductivity as a function of Ag nanoplatelet loading level. The conductivity values range from $10^{-8}\, S/m$ to $10^{-3}\, S/m$ as the loading level of Ag nanoplatelets is increased from 0% to $40\, vol\%$. Although the data is quite scattered, there is a general upward trend, starting at $\approx 18\% - 20\%\, AgNP - BiOCl$. This broad percolation threshold can be explained by the highly non-uniform nature of the composite films. Due to the random arrangement of the Ag nanoplatelets within the sprayed network, the same loading level can have different distributions of nanoplatelets - with some leading to percolative paths, while others not. This is especially clear around the percolation threshold point. For example, across the ten devices of $18\%\, AgNP - BiOCl$ the conductivity ranges between 10^{-9} and $10^{-6}\, S/m$ and across the nine devices of $20\%\, AgNP - BiOCl$ the conductivity ranges between 10^{-9} and $10^{-4}\, S/m$. Furthermore, this type of scatter around the percolation threshold is a statistical effect and to be expected in randomly oriented systems such as these [449].

The increase in conductivity with Ag nanoplatelet loading level can be described using percolation theory. When an electrically conducting filler is added to an insulating matrix, a significant rise in conductivity occurs when the first conducting path through the sample is formed. This theory that is widely used to describe percolation effects in graphene-polymer composites [450, 451], recently has been applied also to nanomaterial (2D:1D and 2D:2D) composites [442–445]. As detailed in Chapter 4, the equation $P \propto \mid \phi – \phi_c \mid^n$ can be written as $\sigma = \sigma_s \mid \phi – \phi_c \mid^t$ [452, 453] where σ is the conductivity of the composite film and σ_S is the scaling factor that generally represents the conductivity

of the metallic filler. The Ag nanoplatelet volume fraction is given by ϕ, with ϕ_c and t being the percolation threshold and the percolation exponent respectively.

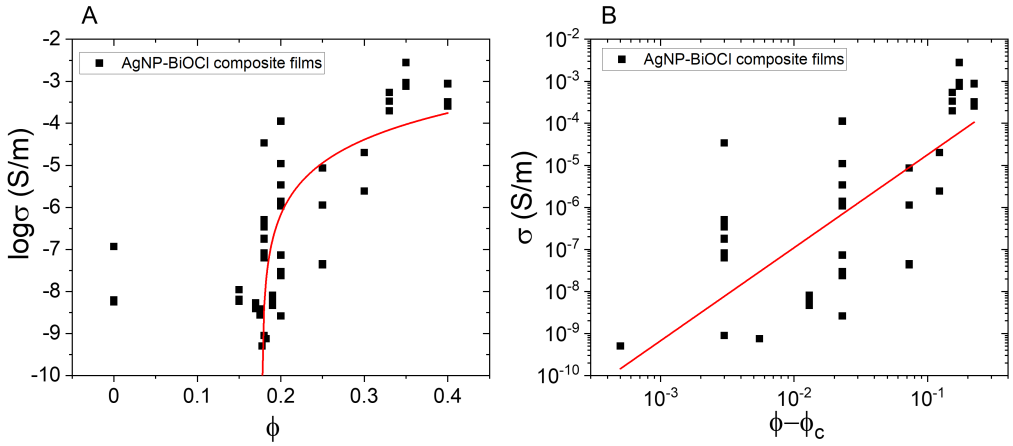

Figure 6.5: A: Conductivity (σ) data fit using percolation theory to identify the percolation threshold (ϕ_c) and exponent (t). B: Conductivity data after percolation threshold to display linear behaviour in conductivity with increase in Ag nanoplatelet loading level. The red lines are fit to the equation $\sigma = \sigma_s \mid \phi – \phi_c \mid^t$.

We have analysed the data for the $AgNP - BiOCl$ platelets using the above equation. Although the data is scattered, the general trend can still be fit as shown in Figure 6.5A. From the fit, we find the percolation threshold to be $\phi_c = 0.177 \pm 2E - 4$. This value is much larger than those previously reported for 3D composites with graphene fillers ($< 1\, vol\%$) [450, 451] and for 1D nanocomposite systems ($\approx 0.1\, vol\%$) [444, 454–457]. However, theoretical predictions show that for composites of randomly oriented monodisperse conducting discs in an insulating matrix, the percolation threshold is actually independent of disk diameter [458]. This relatively high percolation threshold has a practical advantage over 1D nanocomposite systems in that it is much easier to design a percolative system accurately when the required volume fractions are high. It should be noted that the small error presented in the fit derived percolation threshold is not representative of the large scatter seen in the data, but is simply from the fitting function used.

The percolation exponent was observed to be $t = 2.44 \pm 0.8$. This is higher than the expected percolation exponent for 2D composites ($t = 1.33$) [452], but closer to the universal percolation exponent, $t = 2$ [452] for binary mixtures of 3D systems. The scaling factor, $\sigma_s \approx 0.007\, S/m$ is deduced from the intercept. Considering that the scatter in the data is across a few orders of magnitude, we do not expect this value to be representative of the conductive filler conductivity. Figure 6.5B shows the conductivity of the composites after the percolation threshold at 0.177 volume fraction to be broadly linear, however the significant scatter in the data should be noted.

6.3.3 Impedance Measurements

The aim of this work was to demonstrate an improvement in the permittivity of a dielectric/conductive filler composite network in the region before percolation. In order

to measure permittivity, impedance spectroscopy was performed on the parallel-plate capacitors to first extract a capacitance and later, the dielectric permittivity. The frequency dependence of the impedance and phase of the composite films was recorded between $100\,Hz$ and $10^6\,Hz$ and the data was fitted to well-established circuit models. As detailed in previous chapters, a sinusoidal voltage, $V = V_0 e^{i\omega t}$ was applied over a range of frequencies, and the associated current, shifted from the voltage by a phase θ i.e. $I = I_0 e^{i(\omega t - \theta)}$ was measured. The AC impedance, which is a complex quantity can be described by $V/I = Z = |Z|\cos\theta + i|Z|\sin\theta = Z_{re} + iZ_{im}$.

The data collected generally fits the model of a series R-C circuit. Shown in Figure 6.6A the modulus of the impedance, $|Z|$ and phase, θ is plotted against the applied frequency, f (note: $\omega = 2\pi f$). It shows the characteristic $1/f$ decay in impedance observed for a capacitor. However, the phase is seen to taper off from -90° towards 0° at high frequencies as shown in the inset of Figure 6.6A. This effect is indicative of a series resistive element present in the system [63, 172, 354]. To make this more clear, the impedance is split into its real (ReZ) and imaginary parts (ImZ), as shown in Figure 6.6B. The imaginary part of the impedance is nearly identical to the modulus of the impedance, suggesting that the system is largely capacitive. The real part of the impedance however shows a plateau at high frequency, which points towards a series resistive element in the system. Noting that the "flattening" of ReZ occurs at $\approx 10^3\,\Omega$, it is possible the resistive element in question is from the sprayed graphene top electrodes, which display resistances of the same order of magnitude (refer Figure 6.4A). Thus, in this case it is fitting to use a series RC circuit model. It should be noted that there is no observable plateau in the low frequency regime, confirming the absence of a parallel resistance. This implies that the sprayed films have no pin-holes.

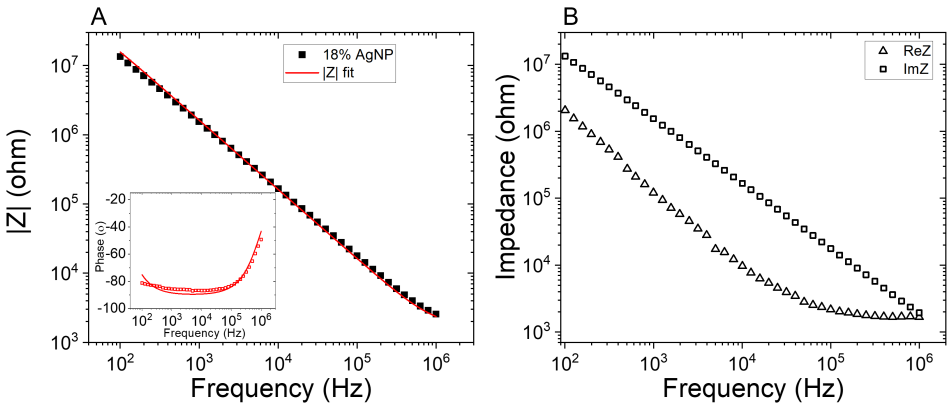

Figure 6.6: A: Impedance and phase (inset) data and fits for a representative capacitor of $18\%AgNP - BiOCl$ composite film. B: The real and imaginary parts of the impedance showing evidence of a series resistance.

Before moving on to the extraction of permittivity from the impedance fits, an important distinction between the devices must be made. We have established that each batch or loading level of composite film contains four devices. It is vital that these devices be treated uniquely and as individual data points. In most cases, the difference between the four devices is insignificant. However, Figure 6.7A shows an example of why it is non-trivial to treat the devices separately. Plotted is the impedance response of

three devices, all made from the "shared" composite film $30\%AgNP - BiOCl$. Device 1 displays a $1/f$ decay in $|Z|$ up to $\approx 10^4\,Hz$ and then plateaus at $\approx 10^5\,\Omega$. Device 2 also displays a $1/f$ decay in $|Z|$ but starting later, at $\approx 10^5\,Hz$ and plateauing at $10^4\,\Omega$. Finally, device 3 is largely non-changing in $|Z|$ with frequency.

These distinct responses from different devices out of the same composite film points to a highly disordered system. Not just the arrangement of the Ag nanoplatelets, but their mass distribution within the dielectric network could largely vary across the film. Although the film is sprayed from a $30\,vol\%$ ink, the true loading level for each of the four devices can diverge from this value and is reflected in their impedance response. By analysing the impedance spectra, the plateau at low frequency seen in device 1 is indicative of a parallel resistance in the system. This parallel resistance is more pronounced in device 2 and is the dominant response in device 3. It can be attributed to the formation of percolative paths by Ag nanoplatelets within the $BiOCl$ network. The percolative paths formed in device 1 are fewest since there is a large capacitative response $(1/f)$ measured in the spectra. Device 2 and device 3 are largely characterised by conductive paths formed by Ag nanoplatelets and show little variation of $|Z|$ with frequency. This is made more clear in the schematics drawn for devices 1, 2 and 3 in Figure 6.7.

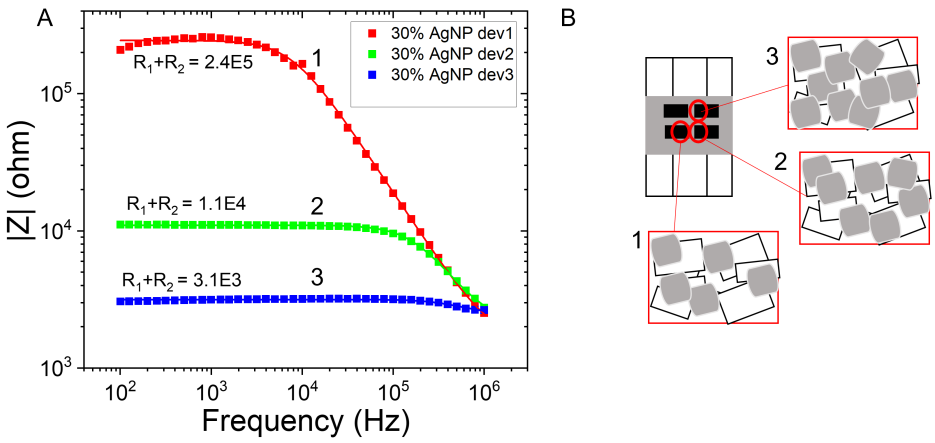

Figure 6.7: A: Impedance response of three devices made out of the same $30\%AgNP - BiOCl$ composite film. B: SSchematic showing how filler non-uniformity in the composite can lead to different electrical responses.

These impedance spectra can be fit using a Randles circuit, the derivation of which was presented in Chapter 4. A Randles circuit is characterised by a plateau in the impedance at low frequency, which indicates the presence of a parallel resistance, as well as a plateau at high frequency, which is indicative of a series resistance. In the frequency range available to us, we only observe the low frequency plateau in impedance. Referring to Chapter 4, the total impedance response of such a circuit can be written as $Z_T = R_1 + \frac{R_2}{1+(\omega R_2 C)^2} - i\frac{\omega R_2^2 C}{1+(\omega R_2 C)^2}$ where R_1 and R_2 are the series and parallel resistances respectively, C is the capacitance of the system and $\omega = 2\pi f$ is the angular frequency. Fitting the impedance response of Device 1, 2 and 3 presented in Figure

6.7A to the above equation, we get parallel resistance values of $R_2 = 2.4 \times 10^5\,\Omega$, $R_2 = 8.9 \times 10^3\,\Omega$ and $R_2 = 724\,\Omega$ respectively. Note that the height of the plateau at low frequencies is in fact $R_1 + R_2$ (Refer explanation of Figure 4.6). Thus, the orientation and possibly quantity of Ag nanoplatelets differs between the four devices, resulting in different responses. This non-uniformity is unsurprising when considering sprayed films where there is little control over the homogeneity and distribution of conductive filler within the network.

The impedance response from all the devices before percolation was recorded and fit to a simple parallel-plate capacitor i.e. by $Z = -i/\omega C$ where $\omega = 2\pi f$ is the angular frequency and C is the capacitance. We have shown that capacitance can be written as $C = \frac{\epsilon_0 \epsilon_r A}{t}$ where ϵ_0 is the permittivity of free space, ϵ_r is the permittivity of the dielectric material between the electrodes and A and t are the overlap-area and thickness of the dielectric respectively. Using the capacitance extracted from the impedance fits, it is straightforward to calculate the permittivity or dielectric constant of the composite films.

When the percolation threshold is approached from below, as is the case with conductor-insulator composites, the dielectric constant ϵ of the composite diverges as follows [426, 427, 459]

$$\epsilon \propto \epsilon_m |\phi - \phi_c|^{-s} \tag{6.1}$$

where ϵ_m is the dielectric constant of the insulator matrix, s is the critical exponent of approximately 1 and ϕ and ϕ_c are fraction of conductive filler and percolation threshold respectively. The above equation suggests that a large dielectric constant can be achieved in composites if $\phi \to \phi_c^-$. Dielectric enhancements of the magnitude $\epsilon/\epsilon_m > 100$ have been observed in several dielectric composites [460–464]. For example, Pecharroman et al. [460] achieved dielectric constants of 80,000 at $10\,kHz$ by preparing percolative composites with $BaTiO_3$ ceramics and Ni particles as the conductive filler. Work on these types of composites with nanomaterials however are limited [436, 437]. Yuan et al. have improved the dielectric constant of a polymer matrix by 260-fold by dispersing graphene flakes in liquid crystals. Enhanced κ values from ≈ 100 to more than 4000 were observed in CNT-reinforced polymer composites [465, 466].

The critical behaviour of the dielectric constant near percolation can be explained by the existence of microcapacitor networks [461]. Microcapacitors can form by neighbouring conductive filler particles and a very thin layer of dielectric between them. Each microcapacitor contributes a large capacitance [459] as the distance between conductive fillers can be on the order of microns (or in some cases, nanometres). This large capacitance can be related with a significant increase in the intensity of local electric field when the conductive fillers are very close to each other i.e., near the percolation threshold. The significant increase in electric field promotes the migration and accumulation of charge carriers at the interfaces between the fillers and matrix.

Presented in Figure 6.8A is the calculated permittivity of each device for composites of varying volume fraction of Ag nanoplatelets. It should be noted that there is a significant spread in the data at each loading level. This can be attributed to the non-uniformity and inhomogeneity of the sprayed composite films described previously and also to the multiple possible variations of nanosheet alignment close to the percolation threshold. The red dashed line represents permittivity of a pure spray coated film of $BiOCl$. An important result is that the permittivity obtained from spray-coated films of $BiOCl$ ($\epsilon_r = 19$) is much lower than that of aerosol-jet printed (AJP) films ($\epsilon_r = 41$).

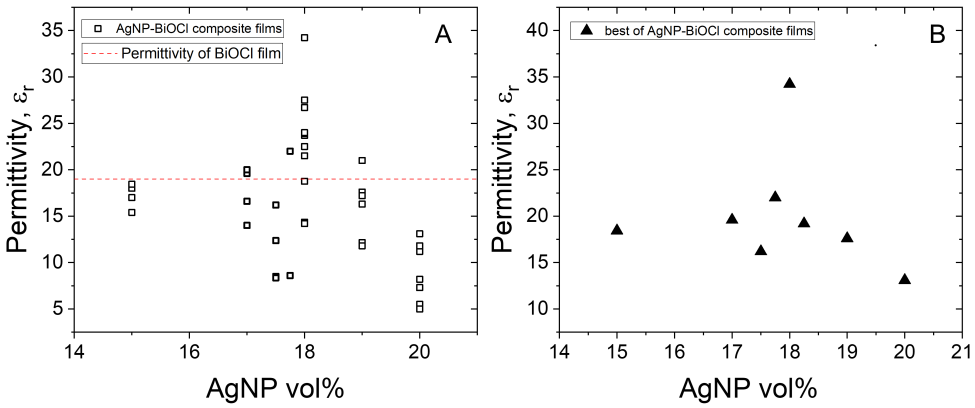

Figure 6.8: A: Permittivity of all devices of various loading levels, before percolation The dashed red line represents the permittivity of a sprayed $BiOCl$-only film. B: Plot of the highest permittivity measured for each device at $AgNP$ loading levels below the percolation threshold.

This could imply the morphology of films formed by spray coating and AJP are different. There could be various reasons for this, in addition to the difference in the underlying mechanisms of deposition of the two techniques. The $BiOCl$ ink used for the AJP films was in IPA and the ink was for spray-coated films was in DI water. This could affect drying mechanisms and material migration within the network during deposition. Furthermore, since the $BiOCl$ was exfoliated in different solvents, the resulting nanosheet size may vary which ultimately affects nanosheet packing and alignment within the film. It should also be noted here that aerosol-jet printing allowed the deposition of a vertically stacked heterostructure, with no shorting seen even for films of thicknesses 1 - 2 μm. A fully stacked network however, could not be achieved through spray coated films. This too points towards a difference in the morphology of the films produced by the two methods.

As shown in Figure 6.8, the $18\% AgNP - BiOCl$ devices consistently display higher permittivity when compared with the other loading levels. This is in-line with the rise in conductivity seen in the composites in Figure 6.4. As the percolation fit yielded a percolation threshold of 17.7%, in theory we would expect to see a spike in permittivity somewhere just below an $AgNP$ loading level in this range. However, the conductivity data was quite scattered and so presents an error in the fit. Furthermore, we must consider laboratory error in measuring out small fractions of volume during composite ink preparation.

We have established that each of the four devices made from a film of a loading level of Ag nanoplatelets must be treated uniquely. Hence, in order to emphasize the increase in permittivity observed in $Ag - BiOCl$ composite films, the device showing the highest permittivity for each loading level was plotted against $AgNP$ volume fraction. As seen in Figure 6.8B, a permittivity of 35 was achieved at $18 vol\%$. This is nearly a two-fold increase in permittivity when compared with pure $BiOCl$ films. The low increase in permittivity can be attributed to poor control of conductive fillers within the insulator networks, with clumps and islands of aggregates forming as Ag volume fraction is increased. Furthermore, the Ag nanoplatelets are significantly larger than the $BiOCl$ nanosheets ($500\,nm$ vs. $100\,nm$) leading to uneven distribution. This is evident

in the spread of data seen in the percolation curve. Although this increase is much lower than theoretical predictions and other experimental results [460–464], this is the first demonstration of insulator-conductive filler films using all 2D nanomaterial composites. Furthermore, it is significantly higher than previously reported permittivities of sprayed films of dielectric 2D nanomaterials that are usually made of hBN (ϵ_r between 3 and 7) [63, 67, 223, 418].

6.4 Conclusions

In summary, composite inks were made by mixing liquid-phase exfoliated $BiOCl$ nanosheets and commercially sourced Ag nanoplatelets. These composite inks were deposited into films by spray coating onto an ITO substrate. Several vertically stacked devices of the form ITO/AgNP-BiOCl/graphene were fabricated in a parallel-plate capacitor geometry to characterise the dielectric properties of the composite films. As the volume fraction of Ag nanoplatelets was increased from 0% to 40%, a percolation curve was observed where the conductivity of the composite film abruptly increased starting from $18\% - 20\%$ volume fraction of Ag nanoplatelets. Using percolation theory, the data was fit to obtain a percolation threshold of 17.7%, percolation exponent of 2.2. The conductivity data was largely scattered about the percolation threshold which is to be expected. Next, impedance spectroscopy was carried out on the devices in order to obtain dielectric permittivity. The data was indicative of pure capacitors, with no pin-holes. A permittivity of 34, which is twice as large as pure $BiOCl$ sprayed films was obtained at $18\% AgNP - BiOCl$, illustrating the formation of microcapacitors within the composite network that increase the overall permittivity. This is a relatively low increase compared to theoretical predictions and some experimental studies. However, it can be attributed to the highly disordered nature of the sprayed composite films, where there is little control over the distribution of conductive fillers through the insulator matrix.

Chapter 7

Improving Dielectric Breakdown Strength through BiOCl-hBN Composites

7.1 Introduction

The vast improvement of performance in electronic devices and their parallel miniaturisation has necessitated the development of insulating materials [438, 467]. In particular, the use of dielectric materials in the form of thin films in energy storage devices, field-effect transistors and other electronic circuitry. The key goal is to develop dielectric materials that have desirable properties such as high electrical resistivity, large dielectric constant and high breakdown strength. Dielectric breakdown strength specifically is an important feature of insulating materials that needs to be studied for the systematic development of devices. With respect to thin films however, dielectric breakdown first occurs in localised regions where there are pin-holes or weak oxide spots [468]. This makes it difficult to measure the dielectric material's intrinsic breakdown strength.

To this point, work to improve the dielectric breakdown strength of insulating materials has been largely focused on polymers. This is due to their use in a broad range of applications, from cable wire insulation [469, 470] to thin film capacitors [471, 472]. Although polymers have several desirable physical properties such as strength and flexibility, there is still scope for improvement of their dielectric properties such as permittivity and breakdown strength. In this vein, there has been a whole host of work done on polymer composites with inorganic materials that elevate their dielectric properties [473–476]. These inorganic materials are generally of high thermal conductivity and dielectric permittivity such as alumina, silicon nitride and boron nitride [477]. Recently with the advance of 2D nanomaterials, there has been reports of polymer nanocomposites that incorporate nanosheets or two-dimensional platelets into a polymer matrix. For instance, Wen et al. have fabricated nanocomposite capacitors with a polymer matrix and monolayer titania that show enhanced energy density and breakdown strengths [473]. Wang et al. have improved the thermal conductivity and dielectric breakdown strength of epoxy films by adding boron nitride nanofibers [475].

The development of faster and more powerful devices is generally seen to be going in the direction of smaller circuitry. This has inadvertently lead to progress in the form of printed electronics fabricated from 2D nanomaterial inks. As expected, this has required a parallel growth in 2D dielectric materials that can be deposited into thin films

and that harbour desirable properties such as large dielectric constants and high breakdown strength. The function of dielectric films in electronic devices is mainly to act as charge separators, but also in lowering operating voltages in thin-film transistors and reducing charge scattering at the dielectric - semiconducting interface. The importance of this role however is not reflected by the body of work done in 2D dielectric nanomaterial films, which remains quite limited and largely focused on boron-nitride. Other inorganic materials such as TiO_2, Al_2O_3, $BaTiO_3$ and $SrTiO_3$ exhibit large dielectric constants [365–368] and low losses, however their exfoliation into nanosheets and subsequent deposition into films through existing printing technology remains unresolved and challenging. In that respect, boron-nitrde has received most of the attention, due its straightforward exfoliation into nanosheets [332, 333] and compatibility with various deposition techniques [63, 286, 385, 394]. Nonetheless, it suffers from inherently low permittivity.

The motivation for this work is to develop a composite material that combines the desirable properties of two dielectric materials. We have established that printed films of $BiOCl$ display permittivities in the range of 20-40 [172], but show low breakdown strength due to the material's narrow band-gap [172]. We also know from previous reported work that hBN shows high dielectric breakdown fields of the order of $250\,V/\mu m$ [78, 131]. In this vein, we suggest a composite film by introducing hBN nanosheets to $BiOCl$ films in order to improve its breakdown strength, while also maintaining a relatively high dielectric permittivity value.

7.2 Experimental Procedure

Graphite powder sourced from Asbury (Grade 3763) was first pre-treated by tip sonication ($450\,W$) in $80\,mL$ of N-methyl-2-pyrrolidone (NMP) at $40\,mg/mL$ for $1\,h$, followed by a $1\,h$ centrifugation at 3218g. The supernatant containing the soluble impurities was discarded and the sediment was redispersed in $80\,mL$ of NMP and tip-sonicated for a further $6\,h$ at $450\,W$ power. The $BiOCl$ and hBN powders were both sourced from Sigma Aldrich and underwent a pre-treatment each by tip sonication ($450\,W$) in a $6\,mg/mL$ solution of sodium cholate and DI water at a concentration of $30\,mg/mL$ for $1\,h$. This was followed by a $1\,h$ centrifugation at 3218g to separate out the sediment. The supernatant containing the soluble impurities was discarded and the sediment redispersed in $2\,mg/mL$ sodium cholate and DI water solution. Both dispersions were tip sonicated for 6 h at 450 W power for exfoliation. The graphene, $BiOCl$ and hBN dispersions were size-selected through a two-step liquid cascade centrifugation technique. They were first centrifuged at 106g for $90\,min$, and the sediment containing large un-exfoliated material discarded. The supernatant from this run was centrifuged at 3830g for $90\,min$, and the corresponding sediment collected.

The graphene sediment trapped between 106g and 3830g was redispersed in IPA to give a $0.5\,mg/mL$ dispersion. Similarly, the $BiOCl$ and hBN sediments were redispersed in DI water to give $5\,mg/mL$ inks. UV–visible spectroscopy was performed using a Varian Cary 5000 to optically characterize the exfoliated nanosheet dispersions. The wavelength was scanned between 800 and $200\,nm$, and a $4\,mm$ path length-reduced volume quartz cuvette was used for the measurement. Bright-field TEM was performed to image the surfactant exfoliated hBN ink using a voltage of $200\,kV$ and a beam current of $107\,\mu A$. Indium Tin Oxide (ITO) coated ($100\,nm$) glass slides were sourced commercially from Ossila. These glass slides were segmented and certain areas etched

away using dilute HCl solution at $50^\circ C$ followed by $NaCl$ solution wash to leave behind a strip of ITO on each glass segment that would behave as the bottom electrode. The glass segments were then cleaned by immersion in Helmanex solution followed by $10min$ of sonic bath. This was repeated with IPA to ensure clean substrates. The $BiOCl-hBN$ films are subsequently sprayed on top of the ITO with Kapton tape used to block areas so as to leave some of the ITO exposed for electrical measurements. The composite inks of varying $BiOCl$ volume fraction were prepared using the $BiOCl$ and hBN inks using the formula $\phi_{BiOCl} = \frac{V_{BiOCl}}{V_{BiOCl}+V_{hBN}}$. They were placed in the sonic bath for $15\,min$ before spray coating to ensure uniform mixing. The films were deposited using a Harder $\&$ Steenbeck Infinity Airbrush secured to a Janome JR2300N mobile gantry. $1\,ml$ of the composite ink was sprayed on top of the ITO and annealed in the vacuum oven overnight at $80^\circ C$ to remove trapped solvent. A mask was placed over this middle layer and $15\,mL$ of graphene sprayed over this to form top electrodes. The device was once again annealed overnight in a vacuum oven at $80^\circ C$ to remove trapped solvent. This procedure yields four separate devices for each volume fraction of $BiOCl-hBN$ ink.

The thickness and roughness of the printed films was measured using a Dektak 150 Stylus Profiler. The morphology of the spray coated composite films was captured using a Zeiss Ultra Plus SEM in the secondary electron mode, with a 30 μm aperture and 2-3 kV accelerating voltage. Preliminary electrical characterisation was done by simple I-V measurements using a Keithley 2621A to confirm capacitor behaviour. Impedance spectroscopy was then performed using a Gamry Reference 3000 to characterise the printed capacitors. Finally, breakdown strength measurements were carried out using a Keithley 4200A-SCS Parameter Analyzer where the voltage was ramped up from $0.1\,V$ to $200\,V$.

7.3 Results and Discussion

7.3.1 Material Characterisation

Boron nitride is an inorganic compound consisting of alternating layers of nitrogen and boron atoms bonded together in a hexagonal lattice structure. In addition to its similarity to graphene, it is highly abundant and non-toxic. There have been several reports on the preparation of 2D nanosheets from the layered bulk crystal of boron nitride [8, 21, 478]. In this work, we employ well-established liquid phase exfoliation techniques on commercially sourced boron nitride powder to produce 2D nanosheets. The second dielectric material used in this work is $BiOCl$. We first characterise the two dielectric inks independently before assembling the composite inks. Since we use the same $BiOCl$ ink as in the previously reported work, the focus in this section will be on the hBN ink.

The extinction spectrum obtained from UV-vis spectroscopy of the dispersion of hBN is shown in Figure 7.1A. As expected for insulating materials [411], the spectra are relatively featureless. It is largely dominated by scattering and decays as a power law at high wavelengths. To properly isolate the constituent absorption and scattering components of the spectra, we use an integrating sphere [403, 411]. The extinction spectra looks to be completely dominated by the scattering component for wavelengths above $\approx 250\,nm$. The resulting absorption spectra shows a clear band-edge at $\approx 220\,nm$, leading to an optical band-gap of $5.635\,eV$ in line with previous reports [8, 478] and consistent with insulating behaviour.

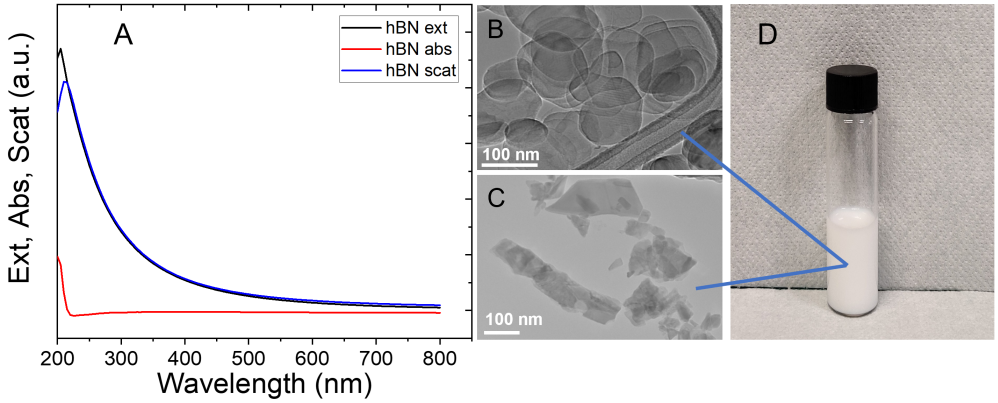

Figure 7.1: A: Extinction spectrum of the surfactant exfoliated dispersion of hBN showing scattering and absorption components. B: TEM image of exfoliated hBN nanosheets. C: TEM image of exfoliated $BiOCl$ nanosheets. D: Image of a $BiOCl - hBN$ composite ink.

Figure 7.1B and C show representative TEM images of the hBN and $BiOCl$ dispersions respectively. In both cases, the images reveal the presence of two-dimensional structures with no large 3D objects observed.The hBN nanosheets appear to be rounded and generally larger than $100\,nm$ in size in line with previous reports of surfactant exfoliated boron nitride [8, 63, 478]. The composite inks are prepared by mixing the two dielectric inks in varying volume fractions of $BiOCl$. Figure 7.1D shows the $BiOCl - hBN$ composite ink to be a homogeneous dispersion that is white in colour.

7.3.2 Device Characterisation

Previous attempts at an all-sprayed vertically stacked heterostructure often lead to shorting, even with films that are $\approx 6\,\mu m$ thick. To avoid this, the composite inks were deposited directly onto ITO, which acts as the bottom electrode. Figure 7.2A shows the schematic of a typical batch of devices of one loading level of a $BiOCl - hBN$ composite film. As depicted, the vertical strip represents ITO, the white box represents the dielectric composite film and the four black squares represent graphene top electrodes. Figure 7.2B is an optical image of a $70\%\,BiOCl - hBN$ device. Graphene ink in IPA is sprayed on top of the film as top electrodes, producing four devices, each of overlap area $2 \times 1.5\,mm^2$. Profilometry was performed to measure the thickness of the sprayed film as shown in Figure 7.2C. The films are generally of thicknesses between $2\,\mu m$ and $4\,\mu m$. They display a roughness of $\approx 15 - 20\%$ which is higher than that of the $AgNP - BiOCl$ composite films $(2 - 5\%)$.

The reason for the higher value of roughness could be because the $BiOCl - hBN$ films are thinner than the $AgNP - BiOCl$ films. Consider an inherent roughness of $R_a = 100\,nm$ for a sprayed nanosheet network due to misalignment of nanosheets on the upper surface. The thinner the films, the higher the overall roughness they display since, thickness–normalised roughness $= R_a/t$ where t is the total thickness of the film. Another possible contribution to the film roughness is the density ratio of the materials that make up the composite. The $AgNP - BiOCl$ composites have a density ratio

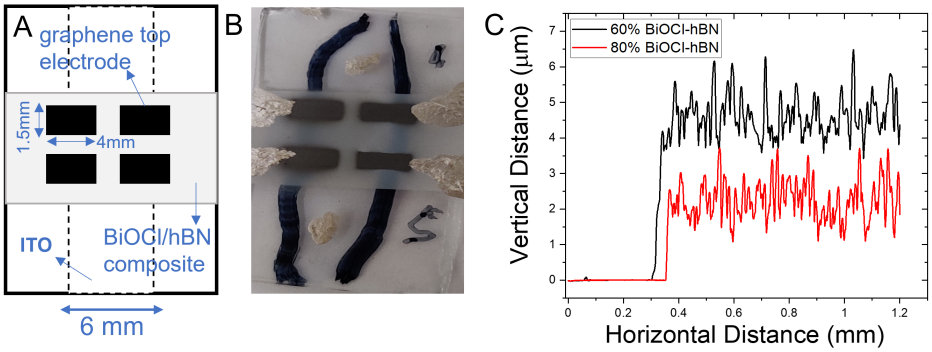

Figure 7.2: A: Schematic showing the geometry of the sprayed capacitors. B: Optical image of a $65\% BiOCl - hBN$ film capacitor. C: Thickness profiles of representative composite films.

of $10 : 7$ whereas the $BiOCl - hBN$ composites have a much higher density ratio of $7 : 2$. This disparity within the composite might lead to uneven deposition and therefore rougher films, although this is just a qualitative observation.

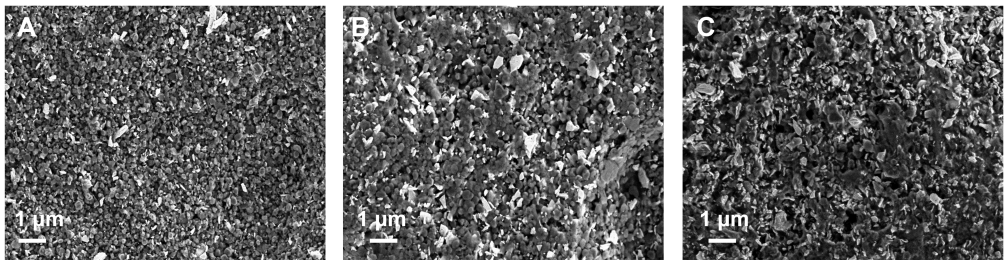

Figure 7.3: A-C: SEM images of $BiOCl - hBN$ composite films of 80, 50 and $25 vol\%$ $BiOCl$ respectively.

To better visualise the dielectric composite films, SEM images were taken of three loading levels of $BiOCl - hBN$ as shown in Figure 7.3. It is clear from the images that the films are pin-hole free and made up of a randomly arranged network of $BiOCl$ and hBN nanosheets. Figure 7.3A shows an $80\%\, BiOCl - hBN$ composite network. The hBN nanosheets can be easily differentiated from the $BiOCl$ nanosheets as they appear brighter. This is partly because they are more "flake-like" and hence have more prominent edges that emit more electrons. Additionally, hBN has a wider band-gap and so is less conductive than $BiOCl$. During SEM imaging, this leads to the material accumulating charge and hence appearing brighter. The $BiOCl$ nanosheets however, are much smaller and are seen to clump together which makes them appear darker. Furthermore, with a narrower band-gap, they conduct more electrons during SEM imaging and appear darker than hBN. Figure 7.3B shows a $50\%\, BiOCl - hBN$ film where the hBN nanosheets are more visible throughout the network. The bottom corner of the image shows a "dip"

in the film that is a common artifact of sprayed networks where non-uniformities appear due to solvent pooling or uneven drying. Figure 7.3C shows an $25\%\ BiOCl-hBN$ film. Here, the contrast between the two types of dielectric nanosheets is less obvious. This can be attributed to the fact that the network is made up mostly of hBN nanosheets that are overlapping, making their edges less prominent and hence causing fewer electrons to be emitted during SEM imaging.

In order to ensure the deposited composite films are insulating, out-of-plane I-V measurements were performed. Figure 7.4A shows representative I-V curves for composite films of 25, 50 and $80vol\%\ BiOCl$. From the slope of the I-V curves, the film conductivity can be deduced to be $6 \times 10^{-9}\ S/m$ confirming the insulating nature of the deposited films. The resistance across the graphene top electrode, termed R_{across}, was also measured to further assure that any resistance to current flow occurs solely due to the insulating composite films, and not due to poor conductivity of the graphene network. Figure 7.4B shows the out-of-plane resistance of representative composite films, termed $R_{through}$ compared with R_{across}. We consider the sprayed composite dielectric film to be insulating if $R_{through} \geq 10^4 \times R_{across}$.

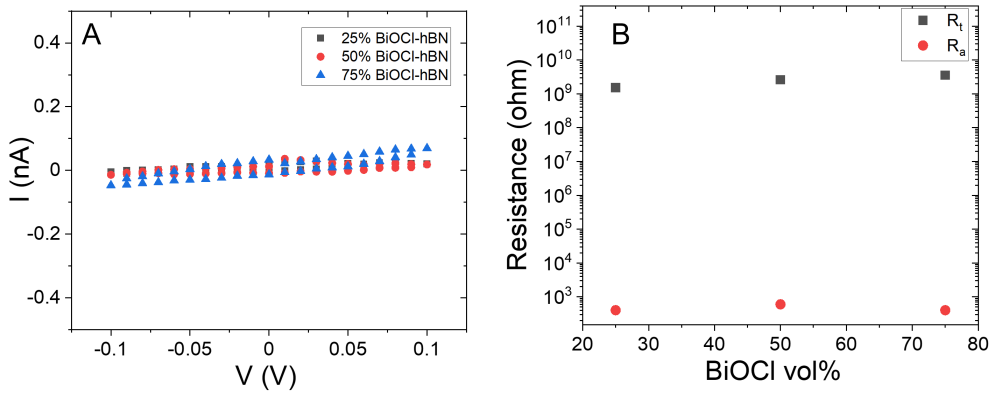

Figure 7.4: A: I-V scans of dielectric composite films with 25%, 50% and $80\%\ BiOCl$. B: R_{across} and $R_{through}$ values of the sprayed capacitors for different loading levels of $BiOCl$.

7.3.3 Impedance Spectroscopy

The aim of this work is to improve the dielectric breakdown strength of a printed $BiOCl$ network by introducing hBN nanosheets. However, it is interesting to observe what effect adding $BiOCl$ nanosheets has on the dielectric permittivity of the composite film. We once again use impedance spectroscopy in order to characterise the dielectric composite network. The impedance response of the devices is recorded as the frequency is scanned from $100\ Hz$ to $10^6\ Hz$. Figure 7.5A and B show the typical impedance and phase responses of two composite films of 65% and $85\%\ BiOCl - hBN$. As seen, the impedance follows a $1/f$ behaviour that is characteristic of a pure capacitor. This is further confirmed by a phase of $-90°$ that only slightly tapers at high frequencies. This trailing off of the phase is representative of a small series resistance as discussed in the previous chapter and can be attributed to the resistances of the top graphene electrode and the ITO bottom electrode.

The data from the 65% and 85% $BiOCl-hBN$ composite films is presented here since they are both of thickness $2.8\,\mu m$. This allows us to compare their impedance responses directly. We measure a higher impedance from the 65% composite film. This is expected since for a pure capacitor, $Z=-i/\omega C$. It follows that the capacitance of the device made from the $85\%BiOCl-hBN$ is higher than that of the $65\%BiOCl-hBN$ device due to larger $BiOCl$ content and will therefore display a lower impedance. Figure 7.5C and D show the impedance and phase data for a representative device of a 75% composite film fit to a capacitor according to the above equation.

In some cases however, the sprayed composite films contain discontinuities in the network, that we call pin-holes. During deposition of the top electrode, the graphene ink can penetrate these pin-holes and cause shorting by creating contacts with the bottom ITO electrode. This can be detected in the impedance response of the shorted devices.

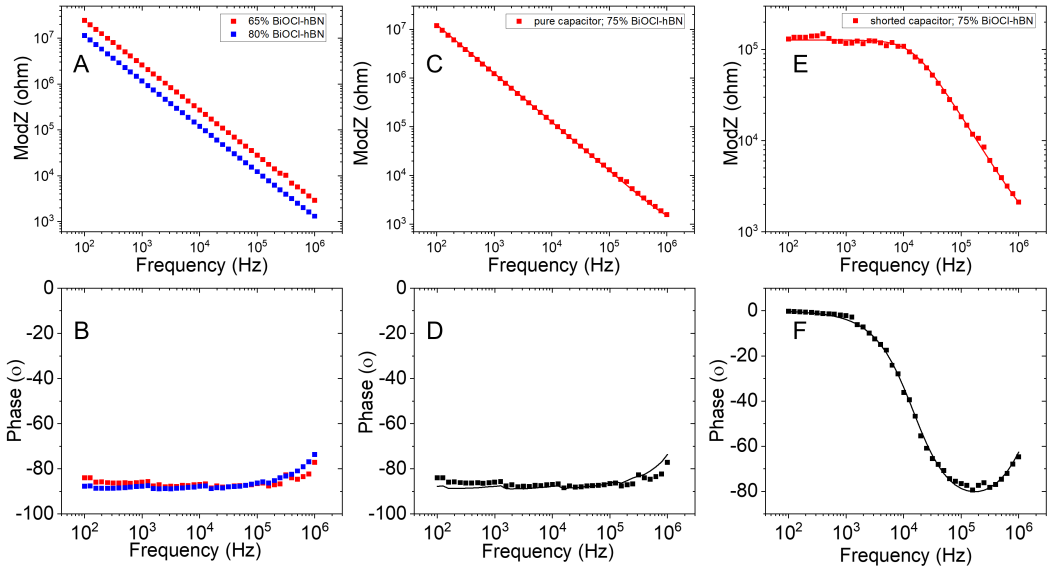

Figure 7.5: A and B: Impedance and phase responses of two films of varying $BiOCl$ content that are both $2.8\,\mu m$ thick for comparison. C and D: Impedance and phase fits of a $75\%BiOCl-hBN$ film with no pin-holes. E and F: Impedance and phase fits of a $75\%BiOCl-hBN$ film with pin-holes

Figure 7.5E and F show the impedance and phase data of a shorted capacitor made from a $75\%BiOCl-hBN$ film. The data is characterised by a plateau at low frequency followed by a $1/f$ decay as the frequency is increased. Similarly, the phase rises up from $\approx -90^\circ$ to 0° at low frequencies. Both of these effects are indicative of a parallel resistance in the system, which suggests that there is some current leakage between the electrodes caused by pin-holes. The slight tapering off of the phase towards 0° at high frequencies is indicative of a series resistance that can be attributed to the graphene top electrode. By considering the above features, the data is fit to a Randles circuit. As detailed in Chapter 4, the impedance of a Randles circuit can be written as $Z_T = R_1 + \frac{R_2}{1+(\omega R_2 C)^2} - i\frac{\omega R_2^2 C}{1+(\omega R_2 C)^2}$ where R_1 and R_2 are the above mentioned series and parallel resistances in the system. Fitting the data to this equation, we can extract the value of R_2 to be $126\times10^3\,\Omega$. Referring back to Figure 7.4B, we can compare this value

to the $R_{through}$ values of the working capacitors ($\approx 10^9\,\Omega$) and confirm that the capacitor has pin-holes that leak current between the electrodes. Thus, impedance spectroscopy can be used as an effective way to identify any pin-holes in the heterostructure system.

The impedance response from the working devices are all fit to a capacitor and the capacitance value is extracted following the equation $Z = -i/\omega C$. Here, $\omega = 2\pi f$ is the angular frequency. We have shown in Chapter 4 that capacitance of a metal-dielectric-metal system can be written as $C = \frac{\epsilon_0 \epsilon_r A}{t}$ where ϵ_0 is the permittivity of free space, ϵ_r is the permittivity of the dielectric material between the electrodes and A and t are the overlap-area and thickness of the dielectric respectively. Thus it is straightforward to calculate the permittivity displayed by the films of varying volume fractions of $BiOCl - hBN$.

Figure 7.6 shows the permittivities of the various capacitors made from the $BiOCl - hBN$ composite films with the volume fraction of $BiOCl$ increasing from 25% to 100%. It should be noted that the permittivity of a pure hBN film was extracted from reference [63]. Kelly et al. fabricated capacitors using ink-jet printed graphene electrodes and a spray-coated film of hBN that was produced using the same liquid-phase exfoliation method as this body of work. Using impedance spectroscopy to characterise the graphene/hBN/graphene capacitors of varying thickness and overlap area, they measured a permittivity of 2.25.

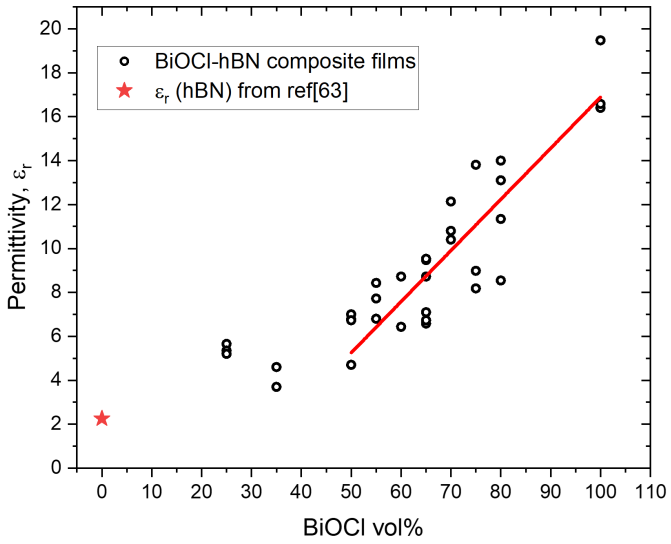

Figure 7.6: Permittivity of $BiOCl - hBN$ composite films of varying $BiOCl$ content fit linearly between $50vol\%$ and $100vol\%$ of $BiOCl$.

As mentioned previously, four graphene electrodes are deposited over the composite films to produce four unique devices. It is clear from the spread of the data between the devices made from the same composite film, that the films are not homogeneous but may contain varying fractions of hBN and $BiOCl$ under each electrode. Some of the devices may even be shorted, in which case we have fewer than four data points for each composite film. The largest spread in data is seen in devices between 50% and $100\% BiOCl - hBN$ composite films. Nevertheless, a general trend can still be observed. The permittivity of the composite films does not increase above ≈ 6 up to a

$50\%BiOCl$ in the composite film. It can be noted however, that the permittivity of a 2D hBN nanosheet network can be improved twice-fold, from 2.25 to ≈ 5 by introducing $50\,vol\%$ of $BiOCl$ nanosheets. Beyond this volume fraction, there is a general linear trend in permittivity as the $BiOCl$ content is increased. A permittivity increase of ≈ 0.2 is observed for every $1\,vol\%BiOCl$ added to the composite.

Previous work on dielectric composites has mainly been in polymer nanocomposites. It has been widely demonstrated that the primary mechanism of polarisation in polymer nanocomposites is via interfacial polarisation caused by the large contrast in the dielectric constant and conductivity at the interface between the polymer matrix and dielectric fillers [479–482]. This type of polarisation in composites can lead to desirable dielectric properties. For instance, Wen et al. have prepared composite films by solution casting polyvinylidene fluoride (PVDF) and monolayer titania (TOML) [473]. They observe a monotonic increase in dielectric constant of the composite with increasing the weight ratio of TOML. Across a frequency range of $10^2\,Hz$ to $10^6\,Hz$, the permittivity is seen to increase from 11 to 14 with an addition of 2 $wt\%$ TOML. A study by Wang et al. has revealed that composites made from epoxy and hBN nanofibres show improved permittivity as well as increased energy storage capability of polymer nanocomposites [475]. In the low frequency region $(0.1-10^2\,Hz)$, they observe an increase in permittivity from 3.5 to ≈ 4.

In our case of composites made from 2D dielectric nanosheets, the improvement in permittivity is larger than those previously reported for polymer nanocomposite films. Furthermore, the fabrication process of the composite films is far less complicated since it only involves simple liquid-phase exfoliation to produce the nanosheets followed by spray coating to deposit the films. In the work of Wen and Wang, the films are prepared by solution casting and coating methods that involve several steps and high temperature post-processing. The resultant films are also on the order of $10-100$ of microns [473, 475], whereas the $BiOCl-hBN$ films are pin-hole free at 3 - 5 μm. Thus, we have demonstrated a straightforward method of preparing dielectric composite films whose permittivity can be tuned from ≈ 4 to ≈ 18 by varying $BiOCl-hBN$ content.

7.3.4 Dielectric Breakdown Analysis

There are several studies to show the use of hBN nanosheet networks in printed electronics, largely due to its wide band-gap. However, they exhibit low permittivities, between 2-7 [63, 286, 385, 394]. It was with this in mind, that $BiOCl$ nanosheet films were investigated in the previous two works since they exhibit permittivities significantly higher than that of hBN [90, 172, 412, 417]. Nonetheless, their disadvantage is that they exhibit low breakdown voltages due to their small band-gap of $3.2\,eV$. We have shown above that the permittivity of hBN networks can be improved with the addition of $BiOCl$ nanosheets. But in order to investigate the advantages of such a composite film over a purely $BiOCl$ nanosheet network, we must show an improvement in the dielectric breakdown strength of $BiOCl$ networks with the addition of hBN nanosheets.

Generally, dielectric breakdown in thin films is irreversible when it is caused by thermal damage due to a surge in current density [483]. Irreversible polarisation events leading to permanent breakdown can also be caused by a change in cell lattice configuration, and due to moving defects and dislocations within the film when a potential difference is applied [484]. Usui et al have demonstrated reversible breakdown in ALD thin films of SiO_2 within a small window of thickness and applied voltage [485]. However, beyond

a critical voltage, permanent dielectric breakdown is observed. We have found the (irreversible) dielectric breakdown strength of aerosol-jet printed films of $BiOCl$ to be $0.67MV/cm$. The dielectric breakdown strength of hBN networks has been shown to be between 1.9 - $2.5\,MV/cm$ [78, 131] and $3\,MV/cm$ for BN/polymer composites [418]. We speculate that this difference is mainly due to their difference in band-gaps. However, the morphology of the films and LPE nanosheet edge defects could also play a role. Dielectric breakdown measurements are generally performed by applying a steadily increasing voltage and measuring the corresponding current until a spike in conduction is observed. This spike in current can be associated with electrons now being allowed to conduct due to the "absence" of a band-gap [486, 487]. Thus for films of the thickness range $\approx 2.5 - 4\,\mu m$, a sufficiently high ($> 300V$) voltage supply is required. Unfortunately, the instrument available to us to perform these dielectric breakdown had a voltage limit of $200\,V$. If we hypothesize that the dielectric breakdown of the composite films follows the rule of mixtures, using the above values of breakdown strength, we can calculate the predicted breakdown voltage required for a $75\%BiOCl - hBN$ film as follows.

$$\begin{aligned} V_{bd}(75\%BiOClhBN) &= (0.67MV/cm \times 0.75) + (2.5MV/cm \times 0.25) \\ &= 1.1275MV/cm \end{aligned}$$

Considering the $75\%BiOCl - hBN$ sprayed film is $2.8\,\mu m$ thick, we would require a voltage of $315.7\,V$ to reach dielectric breakdown. This of course, is just an estimation. Nonetheless, it lies outside of the scope of the voltage source available at present. Figure 7.7 shows the voltage ramp tests performed on $35\%BiOCl - hBN$ and $65\%BiOCl - hBN$ sprayed composite films, compared with the data from AJP $BiOCl$ films presented in Chapter 5.

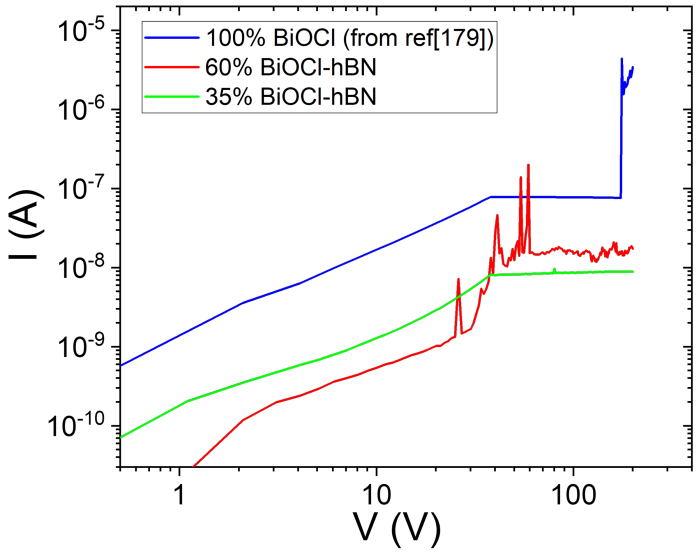

Figure 7.7: Current versus voltage curves to test the dielectric breakdown strength for three different $BiOCl$ films of varying hBN content

The AJP $BiOCl$ film is $3.7\,\mu m$ thick and reaches breakdown, i.e. shows a spike in

conductivity at $\approx 175\,V$ which gives a dielectric breakdown strength of $\approx 47\,V/\mu m$. The $35\%BiOCl-hBN$ and $65\%BiOCl-hBN$ sprayed composite films however, are $\approx 3\,\mu m$ thick and do not show a spike in conductivity across the full range of the applied voltage, up to $200\,V$. This implies that the breakdown strength of these composite films is higher than $\approx 67\,V/\mu m$. Although this is not quantitatively conclusive, we can allude to the fact that introducing hBN to a film of $BiOCl$ raises the voltage needed for the film to reach breakdown. This type of improvement in dielectric breakdown strength has been reported in a few instances through polymer nanocomposites. For example, Li et al. demonstrated in their solution processed ferroelectric terpolymer hBN nanocomposites [488], a 70% increment in dielectric breakdown field as compared with that of the pure polymer when $12wt\%$ boron-nitride nanosheets were added as fillers. Similarly, Wang et al. observed a small increase in breakdown strength of pure epoxy films by introducing $0.5wt\%$ - $1wt\%$ boron-nitride nanofibers. Although we cannot directly compare our results with these published reports due to lack of quantitative data at present, in the future we aim to show that improvement of dielectric breakdown strength of $BiOCl$ films can be achieved through $BiOCl-hBN$ composite films.

7.4 Conclusion

In summary, we have developed dielectric composite inks using liquid phase exfoliated nanosheet dispersions of hBN and $BiOCl$. The composite inks were used to deposit films in a parallel-plate capacitor geometry. An array of capacitors with increasing volume fractions of $BiOCl$ going from 25% to 100% were constructed in order to characterise the permittivity and dielectric breakdown strength of the resultant composite films. Upon adding $BiOCl$ to the composite, no significant increase in permittivity was observed up to $50\,vol\%$ after which, a linear increase was measured with a ≈ 0.2 increase for every $1\,vol\%$ of $BiOCl$ added. The dielectric breakdown measurements however, proved to be more challenging. Since the instrument available to us to perform these dielectric breakdown tests had a voltage limit of $200\,V$ and the thickness of our dielectric capacitors meant that the dielectric breakdown voltage lay outside of this range, we were unable to quantitatively describe the breakdown strength of the composites as a function of hBN content. However, we were able to show preliminary data for a subset of $BiOCl-hBN$ composites at loadings of 35 and $60\,vol\%$, which did not reach breakdown up to $\approx 71.5\,V/\mu m$. This is an improvement on pure $BiOCl$ films ($67\,V/\mu m$) and offers a potential means to tune the dielectric constant of 2D networks going forward.

Chapter 8

Conclusions & Future Work

The evolution of silicon from 'a poor man's alloying agent' [489] in the 1890s to its first demonstration in a transistor in 1954 was anything but predictable. The element that is now synonymous with electronic and optical devices started off with unrelated uses but drove development in purification methods that ultimately bolstered its use in the semiconductor industry. This is not dissimilar to the trajectory seen in the last 20 years with nanomaterial research. While the initial reports consisted of imaging and fabrication through various synthesis methods, more recently, the electrical characteristics of nanomaterials are being explored through the field of printed electronics. In keeping with this, the aim of this thesis was to improve the dielectric properties of nanomaterial films such as permittivity and breakdown strength to keep pace with the rapidly expanding field of low-dimensional materials-based electronics.

While the start of this thesis details the properties of layered crystals and their subsequent synthesis into 2D nanomaterials through solution processing methods, the main focus of this work is to explore the properties of printed networks formed by dielectric nanomaterials. Dielectric networks play the important role of maintaining separation between layers in heterostructure devices by preventing unwanted contacting between conducting and semiconducting channels. Therefore, as the field of printed electronics using nanomaterial inks matures, a parallel investigation into dielectric materials that have desirable properties such as high permittivity and dielectric breakdown strength is necessary.

So far, the reports on printed insulating networks formed from dielectric nanosheets have been largely focused on boron nitride. It is a highly abundant material that has gained traction due to its structural similarity to graphene, often considered as its insulating counterpart. Furthermore, the exfoliation of boron nitride through solution processing methods has been widely reported, making it a reliable material to work with. However, despite having a high dielectric breakdown strength due to its wide band-gap, printed films of boron nitride have only been shown to exhibit a maximum permittivity of 7. In addition to this, depositing continuous thin films of hBN without the use of binders or additives can be quite challenging. Thus, there is evidently room for improvement in developing better performing printed dielectric films. To address this, we presented a new layered dielectric crystal bismuth oxychloride (BiOCl) in Chapter 5. We demonstrated that $BiOCl$ can be easily exfoliated into 2D nanosheets using the well-established method of liquid phase exfoliation. Nanosheets of average size $L = 380\,nm$ were produced and with the help of UV-vis spectroscopy, a band-gap of $3.5\,eV$ was measured confirming their insulating nature. Through spectroscopic methods, the stability

of a dispersion of $BiOCl$ was assessed to be largely unchanging up to several hours.

As mentioned, this work is focused on improving the properties of nanostructured dielectric networks. In order to characterise dielectric films of $BiOCl$, all-printed vertically stacked heterostructures of the form graphene/$BiOCl$/graphene were fabricated using aerosol-jet printing. Considering the novelty of the material as well as the printing method, significant work was undertaken to obtain reproducible networks of dielectric films. However, through trial and error an array of printed capacitors of increasing dielectric thickness were fabricated to obtain a minimum insulating thickness of $1.6\,\mu m$. Through impedance spectroscopy, we were able to model the printed capacitors as Randles circuits and obtain information about the electrode conductivity, current leakage due to pin-holes in the system and most importantly, the capacitance of the system. The graphene electrode conductivity was measured to be between $2300\,S/m$ and $2800\,S/m$ and the out-of-plane resistivity of the dielectric film was of the order of $10^9\,\Omega m$ confirming its insulating nature. On further analysis, we found that the total capacitance response is consistent with two capacitors in series – one of which is thickness independent (C_0), while the other scales as expected with dielectric thickness (C_t). Fitting the data to this model, we find that the thickness independent capacitance is $C_0/A = 16.6 \pm 1.4\,nF/cm^2$. We speculate its origin to be from inter-nanosheet junctions within the graphene electrode. The thickness dependent capacitance can be used to deduce the dielectric permittivity. A relative permittivity of $\epsilon_r = 41 \pm 3$ is calculated for the printed $BiOCl$ films, which is currently the highest reported value for printed dielectric nanosheet networks.

The limited alternatives for dielectric layered crystals that can contribute to the family of nanomaterials is partly why the reports are distorted towards boron nitride. To address this, we can turn to composites as a way of enhancing the electrical properties of a material. One such promising avenue for improving dielectric network properties lies in conductor-insulator composites. Originally only theorised, conductive fillers dispersed in an insulating matrix were shown to lead to a colossal spike in permittivity as the percolation threshold of the conductive filler is approached. This was later demonstrated through ceramic-metal composites and in some instances through liquid crystal suspensions[435–437]. Inspired by this, in Chapter 6 we present conductor-insulator composites using silver nanoplatelets ($AgNP$) and $BiOCl$ nanosheet dispersions. The composite inks, along with a graphene ink were sprayed onto an ITO substrate to produce parallel-plate capacitors of the geometry ITO/$AgNP - BiOCl$/graphene. An array of capacitors was fabricated with increasing volume fractions of Ag nanoplatelets. As the conductor filler content was increased from $0\,vol\%$ to $40\,vol\%$, a percolative behaviour was observed where the conductivity of the composite film started to increase between $18-20\,vol\%$. Using percolation theory to fit the data, we obtain a percolation threshold at $17.7\,vol\%$ and a percolation exponent of 2.2. It should be noted that the conductivity data was largely scattered due to the dimensional disparity within the composite as a result of the large Ag nanoplatelets. This leads to an inherent non-uniformity in the films that is difficult to control given the method of composite preparation and subsequent deposition into films.

Impedance spectroscopy was carried out on the capacitors made from the composite films to characterise their dielectric permittivity. In line with previous reports, an increase in permittivity was observed in the vicinity of the percolation threshold. A permittivity of $\epsilon_r = 34$ was achieved, which is twice as large as the result for pure $BiOCl$ sprayed films. This increase was attributed to the formation of microcapacitors within the composite

network. The surge in the local electric field due to the small distances separating the Ag nanoplatelets contributes to the increased capacitance and hence is reflected in the permittivity. Although the improvement in permittivity observed here is far less impressive than previous reports with ceramic-metal composites, it is the first demonstration of 2D:2D conductor-insulator composites. Deposition of films through spray coating unfortunately lacks the control required over the distribution of the conductive fillers within the insulating matrix to observe significant spikes in permittivity.

In Chapters 5 and 6, we presented potential candidates for dielectric networks that display high permittivity. However, an ideal dielectric material is one that also exhibits high breakdown strength. We performed dielectric breakdown strength studies on aerosol-jet printed films of $BiOCl$ in Chapter 5 where the capacitors were subjected to increasing voltages and the corresponding current measured. A dielectric breakdown strength of $0.67\,MV/cm$ was measured, which is significantly lower than the breakdown strength of boron nitride ($2.5\,MV/cm$). This can be partly attributed to $BiOCl$ having a narrower band-gap but also to physical defects within the network leading to weak points where breakdown can occur. Motivated by this, in Chapter 7 we present a composite made from $BiOCl$ and hBN nanosheets. The composite inks are prepared by mixing of liquid phase exfoliated nanosheet dispersions of $BiOCl$ and hBN. In an identical procedure to the previous study, the composite inks were spray coated into parallel-plate capacitors of the geometry ITO/$BiOCl-hBN$/graphene. An array of capacitors with varying volume fractions of $BiOCl$ were characterised through impedance spectroscopy to reveal their dielectric permittivity.

As the $BiOCl$ content in the composite was increased from 0 to $50\,vol\%$, no significant increase in permittivity was observed. However, beyond $50\,vol\%$ a linear increase in permittivity of 0.2 was measured for every $1\,vol\%$ addition of $BiOCl$. This allowed us to tune the dielectric permittivity of the composite from anywhere between 2 (pure hBN) to 20 (pure $BiOCl$). The aim of this study was to improve the dielectric breakdown strength of $BiOCl$ films by introducing hBN nanosheets into the network. Dielectric breakdown strength measurements are generally performed by applying a steadily increasing voltage to the point where we measure a sudden spike in current. This spike in conductivity is associated with dielectric breakdown. In order to properly quantify the improvement in dielectric strength of our composite films, we would require a voltage source that goes beyond $200\,V$. Unfortunately, the instrument available to us had a limit below this value, and considering the thickness of our composite films, the measurement proved challenging. However, the collected preliminary data suggests an improvement in the breakdown strength upon the addition of hBN. A proof-of-concept was achieved that allows us to develop a protocol for further investigation.

Future Work

Improving the morphology of an insulating network directly affects the progress made in vertically stacked heterostructure devices. Their function as a physical barrier between active layers of a device requires them to be continuous, uniform and defect-free to prevent electrical shorting. In addition to this, with the continual scaling down of device architecture, the dielectric layers need to be thin ($\approx 1\,\mu m$). Therefore, developing thin yet mechanically robust films is essential for advancing the field of printed electronics.

The challenge of insulating a stacked heterostructure device is two-fold. Firstly, the insulating film has to be continuous and free of pin-holes that can lead to unwanted

contacting. Secondly, the very process of deposition of material on top of a film can cause redispersion of the underlying film, especially in digital printing techniques that make use of liquid inks. Redispersion of the underlying network can lead to non-uniform interfaces and material migration which results in a failed device. Hence, it is important to not only improve the physical integrity of the insulating film, but also to ensure the underlying network is not damaged.

An approach to mechanically reinforcing our printed networks can be found in 1D:2D nanocomposites. It has been previously shown that adding carbon nanotubes to a network of nanosheets significantly improves its mechanical properties [444] such as strength and toughness. Applying this to dielectric films, a possible route to explore would be composites that incorporate boron nitride nanotubes (BNNT) into dielectric nanosheet networks such as hBN or $BiOCl$. In this way, the physical properties of the network could be improved while maintaining electrical insulation. 1D:2D composite films with varying loading levels of BNNTs can be printed as parallel-plate capacitors and characterised in the same manner as the studies presented here. The mechanical improvement can be described as a function of the loading level of BNNTs required to reduce the minimum insulating thickness of a pure (BNNT-free) network.

An interesting result we observed during the fabrication of our bottom electrode/ middle layer/top electrode type heterostructures was that the possibility of device shorting is significantly higher when the bottom electrode is itself a printed film. For example, in the work presented in Chapters 6 and 7, where the device geometry was ITO/middle layer/graphene, the success rate of an un-shorted device was very high. However, when an all-sprayed device was attempted, it was likely shorted. This raises concerns that the roughness of the bottom electrode could be leading to a highly porous and discontinuous middle layer during deposition. This is another aspect which can potentially be improved by 1D:2D nanocomposites. Incorporating BNNTs in the bottom electrode nanosheet network could possibly improve its structural stability, reducing the risk of redispersion upon deposition of a subsequent layer. This type of composite can be further extended to include semiconducting films which often find themselves sandwiched between other nanosheet networks in printed devices and would be required to be structurally stable.

We have established how important it is to understand the morphology of these printed networks in order to control the resulting film properties such as permittivity and breakdown strength. In this way, microscopic imaging techniques might allow characterisation of the morphology of such structures. For example, with the help of Focused Ion Beam technology, cross-sections of printed networks with and without BNNTs can be imaged to obtain valuable information about properties such as porosity, nanosheet alignment and interface quality. Technology such as the Atlas imaging tool that is emerging makes it possible to image pin-holes within a film. Such avenues can be explored by future students with regards to dielectric films in order to compare morphologies of various types of networks. By imaging an array of printed networks that are made up of different sized 2D nanosheets but deposited using the same printing technology, or, by imaging an array of printed networks that are made up of the same sized 2D nanosheets but deposited using different printing technologies, one can study the morphology and packing of such networks in a more detailed way. Furthermore, these images can then be related to measured electronic properties to draw certain conclusions.

Perfecting the fabrication of all-printed vertically stacked heterostructure devices with well-defined interfaces and uniform, pin-hole free films can lead to various opportunities in printed electronics. One such application can be in supercapacitors formed from

printed nanosheet networks (that are inherently porous) and the addition of a liquid electrolyte. The ions in the electrolyte will then be separated only by atomic-scale distances at each of the electrodes which will significantly increase the capacitance, hence forming a supercapacitor. Other applications can include all printed thin-film transistors, electronics printed on textile substrates, printed batteries and solar cells to name a few.

To further the work in printed electronics, in addition to developing new dielectric materials, similar progress must be made in understanding printing technologies. In this vein, we propose additional characterisation of aerosol-jet printing. Being a relatively new and complex technology, little is known about the specifics of the printing process. Further work can include quantification of exactly how the nanomaterial within the ink is atomised - i.e. are the smaller nanosheets atomised before the bigger nanosheets. This will give us more information on how ink concentration and composition will affect film thickness and morphology. Since the AJP process is highly digitised, it would be beneficial to understand exactly how the various different parameters such as sheath gas flow, carrier gas flow and atomisation current fluctuate during the printing process and how best to minimise this to get highly reproducible printed features.

In conclusion, we believe this thesis presents credible alternatives for dielectric materials that can be used in printed electronic applications. By bringing forward bismuth oxychloride, we present a pathway towards dielectric networks that exhibit significantly higher permittivity than the currently used boron nitride films. Encouraged by conductor-insulator composites that display desirable dielectric properties, we demonstrate for the first time 2D:2D nanocomposite films that show promise for further improvement in permittivity. Lastly, we provide a framework for improving the breakdown strength of bismuth oxychloride by proposing 2D:2D composites made with boron nitride. Additionally, in carrying-out these studies, we have vastly improved upon the impedance spectroscopic techniques used in order to characterise printed dielectric films. We demonstrate how it can be used as a protocol for understanding some morphological properties of dielectric networks in heterostructure devices. It is hoped that the work presented in this thesis can be used as a road-map for future work on printed dielectric nanosheet networks.

Bibliography

[1] Eric Drexler. "There's Plenty of Room at the Bottom". In: *Richard Feynman, Pasadena* 29 (2009).

[2] Ian Freestone et al. "The Lycurgus cup—a roman nanotechnology". In: *Gold bulletin* 40.4 (2007), pp. 270–277.

[3] Delphine Schaming and Hynd Remita. "Nanotechnology: from the ancient time to nowadays". In: *Foundations of Chemistry* 17.3 (2015), pp. 187–205.

[4] CG Granqvist et al. "Far-infrared absorption in ultrafine Al particles". In: *Physical Review Letters* 37.10 (1976), p. 625.

[5] HW Kroto. "JR Health, SC O'Brien, RF Curl, and RE Smalley". In: *Nature* 318.162 (1985), p. I985.

[6] Kostya S Novoselov et al. "Electric field effect in atomically thin carbon films". In: *science* 306.5696 (2004), pp. 666–669.

[7] Gowoon Cheon et al. "Data mining for new two-and one-dimensional weakly bonded solids and lattice-commensurate heterostructures". In: *Nano letters* 17.3 (2017), pp. 1915–1923.

[8] Jonathan N Coleman. "Liquid exfoliation of defect-free graphene". In: *Accounts of chemical research* 46.1 (2013), pp. 14–22.

[9] Gordon Moore. "The future of integrated electronics". In: *Fairchild Semiconductor internal publication* 2 (1964).

[10] Semiconductor Industry Association et al. *International technology roadmap for semiconductors (ITRS)*. 1999.

[11] AA Tsonis and JB Elsner. "The weather attractor over very short timescales". In: *Nature* 333.6173 (1988), pp. 545–547.

[12] TW Ebbesen and PM Ajayan. "Large-scale synthesis of carbon nanotubes". In: *Nature* 358.6383 (1992), pp. 220–222.

[13] Richard E Smalley. "Discovering the fullerenes". In: *Reviews of Modern Physics* 69.3 (1997), p. 723.

[14] Wei Gao. "The chemistry of graphene oxide". In: *Graphene oxide*. Springer, 2015, pp. 61–95.

[15] G Ruess and F Vogt. "Höchstlamellarer Kohlenstoff aus Graphitoxyhydroxyd." In: *Monatshefte für Chemie und verwandte Teile anderer Wissenschaften* 78.3 (1948), pp. 222–242.

[16] RF Frindt. "Single crystals of MoS2 several molecular layers thick". In: *Journal of Applied Physics* 37.4 (1966), pp. 1928–1929.

[17] GF Walker and WG Garrett. "Chemical exfoliation of vermiculite and the production of colloidal dispersions". In: *Science* 156.3773 (1967), pp. 385–387.

[18] Rudolf Peierls. "Quelques propriétés typiques des corps solides". In: *Annales de l'institut Henri Poincaré*. Vol. 5. 3. 1935, pp. 177–222.

[19] Lev Davidovich Landau. "Zur Theorie der phasenumwandlungen II". In: *Phys. Z. Sowjetunion* 11.545 (1937), pp. 26–35.

[20] LD Landau and EM Lifshitz. "CHAPTER I–THE FUNDAMENTAL PRINCIPLES OF STATISTICAL PHYSICS". In: *Course of Theoretical Physics* (1980), pp. 1–33.

[21] Valeria Nicolosi et al. "Liquid exfoliation of layered materials". In: *Science* 340.6139 (2013).

[22] Tianjiao Liu et al. "Porous two-dimensional materials for energy applications: Innovations and challenges". In: *Materials Today Energy* 6 (2017), pp. 79–95.

[23] Mingsheng Xu et al. "Graphene-like two-dimensional materials". In: *Chemical reviews* 113.5 (2013), pp. 3766–3798.

[24] Sheneve Z Butler et al. "Progress, challenges, and opportunities in two-dimensional materials beyond graphene". In: *ACS nano* 7.4 (2013), pp. 2898–2926.

[25] Deep Jariwala et al. "Emerging device applications for semiconducting two-dimensional transition metal dichalcogenides". In: *ACS nano* 8.2 (2014), pp. 1102–1120.

[26] Zheng Cui. *Printed electronics: materials, technologies and applications*. John Wiley & Sons, 2016.

[27] Michael Naguib et al. "25th anniversary article: MXenes: a new family of two-dimensional materials". In: *Advanced materials* 26.7 (2014), pp. 992–1005.

[28] Robin B Jacobs-Gedrim et al. "Extraordinary photoresponse in two-dimensional In2Se3 nanosheets". In: *ACS nano* 8.1 (2014), pp. 514–521.

[29] Kai Cheng et al. "2D lateral heterostructures of group-III monochalcogenide: Potential photovoltaic applications". In: *Applied Physics Letters* 112.14 (2018), p. 143902.

[30] Sujoy Ghosh et al. "Fast photoresponse and high detectivity in copper indium selenide (CuIn7Se11) phototransistors". In: *2D Materials* 5.1 (2017), p. 015001.

[31] Joshua O Island et al. "Gate controlled photocurrent generation mechanisms in high-gain In2Se3 phototransistors". In: *Nano letters* 15.12 (2015), pp. 7853–7858.

[32] Foroutan Masumeh, Fatemi S Jamilaldin, and Fatemi S Mahmood. "A mini-review on dispersion and functionalization of boron nitride nanotubes". In: *Journal of Nanostructure in Chemistry* 10.4 (2020), pp. 265–274.

[33] Raul Arenal et al. "Raman spectroscopy of single-wall boron nitride nanotubes". In: *Nano letters* 6.8 (2006), pp. 1812–1816.

[34] Jun Feng et al. "Metallic few-layered VS2 ultrathin nanosheets: high two-dimensional conductivity for in-plane supercapacitors". In: *Journal of the American Chemical Society* 133.44 (2011), pp. 17832–17838.

[35] Chao Yang et al. "Metallic graphene-like VSe2 ultrathin nanosheets: superior potassium-ion storage and their working mechanism". In: *Advanced Materials* 30.27 (2018), p. 1800036.

[36] Fangwang Ming et al. "Solution synthesis of VSe2 nanosheets and their alkali metal ion storage performance". In: *Nano Energy* 53 (2018), pp. 11–16.

[37] Qingqing Ji et al. "Metallic vanadium disulfide nanosheets as a platform material for multifunctional electrode applications". In: *Nano letters* 17.8 (2017), pp. 4908–4916.

[38] Mark A Lukowski et al. "Enhanced hydrogen evolution catalysis from chemically exfoliated metallic MoS2 nanosheets". In: *Journal of the American Chemical Society* 135.28 (2013), pp. 10274–10277.

[39] Mark A Lukowski et al. "Highly active hydrogen evolution catalysis from metallic WS 2 nanosheets". In: *Energy & Environmental Science* 7.8 (2014), pp. 2608–2613.

[40] Babak Anasori, Maria R Lukatskaya, and Yury Gogotsi. "2D metal carbides and nitrides (MXenes) for energy storage". In: *Nature Reviews Materials* 2.2 (2017), pp. 1–17.

[41] Babak Anasori and Ûrij G Gogotsi. *2D metal carbides and nitrides (MXenes)*. Springer, 2019.

[42] Xinliang Li et al. "2D carbide MXene Ti2CTX as a novel high-performance electromagnetic interference shielding material". In: *Carbon* 146 (2019), pp. 210–217.

[43] Marina Mariano et al. "Solution-processed titanium carbide MXene films examined as highly transparent conductors". In: *Nanoscale* 8.36 (2016), pp. 16371–16378.

[44] Hayelom Dargo Beyene et al. "Synthesis paradigm and applications of silver nanoparticles (AgNPs), a review". In: *Sustainable materials and technologies* 13 (2017), pp. 18–23.

[45] Run Xu et al. "Single-crystal metal nanoplatelets: Cobalt, nickel, copper, and silver". In: *Crystal growth & design* 7.9 (2007), pp. 1904–1911.

[46] Guichuan Xing et al. "The physics of ultrafast saturable absorption in graphene". In: *Optics express* 18.5 (2010), pp. 4564–4573.

[47] JW McClure. "Diamagnetism of graphite". In: *Physical Review* 104.3 (1956), p. 666.

[48] JC Slonczewski and PR Weiss. "Band structure of graphite". In: *Physical Review* 109.2 (1958), p. 272.

[49] Gordon W Semenoff. "Condensed-matter simulation of a three-dimensional anomaly". In: *Physical Review Letters* 53.26 (1984), p. 2449.

[50] Eduardo Fradkin. "Critical behavior of disordered degenerate semiconductors. II. Spectrum and transport properties in mean-field theory". In: *Physical review B* 33.5 (1986), p. 3263.

[51] F Duncan M Haldane. "Model for a quantum Hall effect without Landau levels: Condensed-matter realization of the" parity anomaly"". In: *Physical review letters* 61.18 (1988), p. 2015.

[52] Andre K Geim and Konstantin S Novoselov. "The rise of graphene". In: *Nanoscience and technology: a collection of reviews from nature journals*. World Scientific, 2010, pp. 11–19.

[53] Philip Richard Wallace. "The band theory of graphite". In: *Physical review* 71.9 (1947), p. 622.

[54] Yanyan Xu et al. "Liquid-Phase exfoliation of graphene: An overview on exfoliation media, techniques, and challenges". In: *Nanomaterials* 8.11 (2018), p. 942.

[55] A Hernández-Mınguez, YT Liou, and PV Santos. "Interaction of surface acoustic waves with electronic excitations in graphene". In: *Journal of Physics D: Applied Physics* 51.38 (2018), p. 383001.

[56] Kirill I Bolotin et al. "Ultrahigh electron mobility in suspended graphene". In: *Solid state communications* 146.9-10 (2008), pp. 351–355.

[57] M Garašanin. "The Eneolithic period in the central Balkan area". In: *The Cambridge ancient history* 3 (1982), pp. 136–62.

[58] Ruben Mas-Balleste et al. "2D materials: to graphene and beyond". In: *Nanoscale* 3.1 (2011), pp. 20–30.

[59] Vitor M Pereira, AH Castro Neto, and NMR Peres. "Tight-binding approach to uniaxial strain in graphene". In: *Physical Review B* 80.4 (2009), p. 045401.

[60] Changgu Lee et al. "Measurement of the elastic properties and intrinsic strength of monolayer graphene". In: *science* 321.5887 (2008), pp. 385–388.

[61] Alexander A Balandin et al. "Superior thermal conductivity of single-layer graphene". In: *Nano letters* 8.3 (2008), pp. 902–907.

[62] Takeshi Terao et al. "Alignment of boron nitride nanotubes in polymeric composite films for thermal conductivity improvement". In: *The Journal of Physical Chemistry C* 114.10 (2010), pp. 4340–4344.

[63] Adam G Kelly et al. "All-printed capacitors from graphene-BN-graphene nanosheet heterostructures". In: *Applied Physics Letters* 109.2 (2016), p. 023107.

[64] Adam G Kelly et al. "All-printed thin-film transistors from networks of liquid-exfoliated nanosheets". In: *Science* 356.6333 (2017), pp. 69–73.

[65] Ning Guo et al. "Fabrication of large area hexagonal boron nitride thin films for bendable capacitors". In: *Nano Research* 6.8 (2013), pp. 602–610.

[66] Andrew Harvey et al. "Exploring the versatility of liquid phase exfoliation: producing 2D nanosheets from talcum powder, cat litter and beach sand". In: *2D Materials* 4.2 (2017), p. 025054.

[67] Jian Zhu et al. "Layer-by-layer assembled 2D montmorillonite dielectrics for solution-processed electronics". In: *Advanced Materials* 28.1 (2016), pp. 63–68.

[68] A Nagashima et al. "Electronic structure of monolayer hexagonal boron nitride physisorbed on metal surfaces". In: *Physical review letters* 75.21 (1995), p. 3918.

[69] Martina Corso et al. "Boron nitride nanomesh". In: *Science* 303.5655 (2004), pp. 217–220.

[70] Kostya S Novoselov et al. "Two-dimensional atomic crystals". In: *Proceedings of the National Academy of Sciences* 102.30 (2005), pp. 10451–10453.

[71] D Pacile et al. "The two-dimensional phase of boron nitride: Few-atomic-layer sheets and suspended membranes". In: *Applied Physics Letters* 92.13 (2008), p. 133107.

[72] Lu Hua Li et al. "Large-scale mechanical peeling of boron nitride nanosheets by low-energy ball milling". In: *Journal of materials chemistry* 21.32 (2011), pp. 11862–11866.

[73] Chuanhong Jin et al. "Fabrication of a freestanding boron nitride single layer and its defect assignments". In: *Physical review letters* 102.19 (2009), p. 195505.

[74] Ying Ian Chen. *Nanotubes and nanosheets: functionalization and applications of boron nitride and other nanomaterials*. CRC Press, 2015.

[75] Dmitri Golberg et al. "Boron nitride nanotubes and nanosheets". In: *ACS nano* 4.6 (2010), pp. 2979–2993.

[76] Ki Kang Kim, Hyun Seok Lee, and Young Hee Lee. "Synthesis of hexagonal boron nitride heterostructures for 2D van der Waals electronics". In: *Chemical Society Reviews* 47.16 (2018), pp. 6342–6369.

[77] Freddie Withers et al. "Heterostructures produced from nanosheet-based inks". In: *Nano letters* 14.7 (2014), pp. 3987–3992.

[78] Robyn Worsley et al. "All-2D material inkjet-printed capacitors: toward fully printed integrated circuits". In: *Acs Nano* 13.1 (2018), pp. 54–60.

[79] Inanc Meric et al. "Graphene field-effect transistors based on boron–nitride dielectrics". In: *Proceedings of the IEEE* 101.7 (2013), pp. 1609–1619.

[80] Cheol-Hwan Park and Steven G Louie. "Energy gaps and stark effect in boron nitride nanoribbons". In: *Nano letters* 8.8 (2008), pp. 2200–2203.

[81] Kenji Watanabe et al. "Far-ultraviolet plane-emission handheld device based on hexagonal boron nitride". In: *Nature photonics* 3.10 (2009), pp. 591–594.

[82] Kenji Watanabe, Takashi Taniguchi, and Hisao Kanda. "Direct-bandgap properties and evidence for ultraviolet lasing of hexagonal boron nitride single crystal". In: *Nature materials* 3.6 (2004), pp. 404–409.

[83] D Golberg et al. "Synthesis and characterization of ropes made of BN multiwalled nanotubes". In: *Scripta Materialia* 44.8-9 (2001), pp. 1561–1565.

[84] Angshuman Nag et al. "Graphene analogues of BN: novel synthesis and properties". In: *ACS nano* 4.3 (2010), pp. 1539–1544.

[85] Nasim Alem et al. "Atomically thin hexagonal boron nitride probed by ultrahigh-resolution transmission electron microscopy". In: *Physical Review B* 80.15 (2009), p. 155425.

[86] Yingchun Zhu et al. "Field nanoemitters: ultrathin BN nanosheets protruding from Si3N4 nanowires". In: *Nano letters* 6.12 (2006), pp. 2982–2986.

[87] Nasreen G Chopra and A Zettl. "Measurement of the elastic modulus of a multi-wall boron nitride nanotube". In: *Solid State Communications* 105.5 (1998), pp. 297–300.

[88] Takeshi Terao et al. "Thermal conductivity improvement of polymer films by catechin-modified boron nitride nanotubes". In: *The Journal of Physical Chemistry C* 113.31 (2009), pp. 13605–13609.

[89] Takashi Sugino and Tomoyoshi Tai. "Dielectric constant of boron nitride films synthesized by plasma-assisted chemical vapor deposition". In: *Japanese Journal of Applied Physics* 39.11A (2000), p. L1101.

[90] Zhao Ran et al. "Bismuth and antimony-based oxyhalides and chalcohalides as potential optoelectronic materials". In: *npj Computational Materials* 4.1 (2018), pp. 1–7.

[91] Zhou Song et al. "Improved photocatalytic degradation of perfluorooctanoic acid on oxygen vacancies-tunable bismuth oxychloride nanosheets prepared by a facile hydrolysis". In: *Journal of hazardous materials* 377 (2019), pp. 371–380.

[92] Haijun Zhang, Lu Liu, and Zhen Zhou. "Towards better photocatalysts: first-principles studies of the alloying effects on the photocatalytic activities of bismuth oxyhalides under visible light". In: *Physical Chemistry Chemical Physics* 14.3 (2012), pp. 1286–1292.

[93] Wenjuan Yang et al. "Study of structural, electronic and optical properties of tungsten doped bismuth oxychloride by DFT calculations". In: *Physical Chemistry Chemical Physics* 16.39 (2014), pp. 21349–21355.

[94] Xue Zhang et al. "The stabilities and electronic structures of single-layer bismuth oxyhalides for photocatalytic water splitting". In: *Physical Chemistry Chemical Physics* 16.47 (2014), pp. 25854–25861.

[95] Hui Li et al. "Facet-dependent nonlinear optical properties of bismuth oxychloride single-crystal nanosheets". In: *Journal of Materials Chemistry C* 6.32 (2018), pp. 8709–8716.

[96] Tao Jing et al. "The photocatalytic properties of ultrathin bismuth oxychloride nanosheets: a first principles study". In: *Physical Chemistry Chemical Physics* 18.10 (2016), pp. 7261–7268.

[97] Meili Guan et al. "Vacancy associates promoting solar-driven photocatalytic activity of ultrathin bismuth oxychloride nanosheets". In: *Journal of the American Chemical Society* 135.28 (2013), pp. 10411–10417.

[98] Andrew J Mannix et al. "Synthesis and chemistry of elemental 2D materials". In: *Nature Reviews Chemistry* 1.2 (2017), pp. 1–14.

[99] Konstantin S Novoselov et al. "A roadmap for graphene". In: *nature* 490.7419 (2012), pp. 192–200.

[100] L Ng et al. *Printing of Graphene and Related 2D Materials*. Springer, 2018.

[101] Yagang Yao et al. "Large-scale production of two-dimensional nanosheets". In: *Journal of Materials Chemistry* 22.27 (2012), pp. 13494–13499.

[102] MS Dresselhaus and G Dresselhaus. "Intercalation compounds of graphite". In: *Advances in Physics* 30.2 (1981), pp. 139–326.

[103] Xiaolin Li et al. "Highly conducting graphene sheets and Langmuir–Blodgett films". In: *Nature nanotechnology* 3.9 (2008), pp. 538–542.

[104] Cristina Vallés et al. "Solutions of negatively charged graphene sheets and ribbons". In: *Journal of the american chemical society* 130.47 (2008), pp. 15802–15804.

[105] Zhiyuan Zeng et al. "An effective method for the fabrication of few-layer-thick inorganic nanosheets". In: *Angewandte Chemie International Edition* 51.36 (2012), pp. 9052–9056.

[106] Jian Zheng et al. "High yield exfoliation of two-dimensional chalcogenides using sodium naphthalenide". In: *Nature communications* 5.1 (2014), pp. 1–7.

[107] Goki Eda et al. "Photoluminescence from chemically exfoliated MoS2". In: *Nano letters* 11.12 (2011), pp. 5111–5116.

[108] Keith R Paton et al. "Scalable production of large quantities of defect-free few-layer graphene by shear exfoliation in liquids". In: *Nature materials* 13.6 (2014), pp. 624–630.

[109] Eswaraiah Varrla et al. "Large-scale production of size-controlled MoS2 nanosheets by shear exfoliation". In: *Chemistry of Materials* 27.3 (2015), pp. 1129–1139.

[110] Likai Li et al. "Black phosphorus field-effect transistors". In: *Nature nanotechnology* 9.5 (2014), pp. 372–377.

[111] Catharina Knieke et al. "Scalable production of graphene sheets by mechanical delamination". In: *Carbon* 48.11 (2010), pp. 3196–3204.

[112] Min Yi and Zhigang Shen. "A review on mechanical exfoliation for the scalable production of graphene". In: *Journal of Materials Chemistry A* 3.22 (2015), pp. 11700–11715.

[113] Veronica Leon et al. "Few-layer graphenes from ball-milling of graphite with melamine". In: *Chemical Communications* 47.39 (2011), pp. 10936–10938.

[114] Alessandra Fabbro et al. "Graphene-based interfaces do not alter target nerve cells". In: *ACS nano* 10.1 (2016), pp. 615–623.

[115] Weifeng Zhao et al. "Preparation of graphene by exfoliation of graphite using wet ball milling". In: *Journal of materials chemistry* 20.28 (2010), pp. 5817–5819.

[116] Cornelia Damm, Thomas J Nacken, and Wolfgang Peukert. "Quantitative evaluation of delamination of graphite by wet media milling". In: *Carbon* 81 (2015), pp. 284–294.

[117] Thomas J Nacken et al. "Determination of quantitative structure-property and structure-process relationships for graphene production in water". In: *Nano Research* 8.6 (2015), pp. 1865–1881.

[118] Claudia Backes et al. "Guidelines for exfoliation, characterization and processing of layered materials produced by liquid exfoliation". In: *Chemistry of materials* 29.1 (2017), pp. 243–255.

[119] Guohua Hu et al. "Functional inks and printing of two-dimensional materials". In: *Chemical Society Reviews* 47.9 (2018), pp. 3265–3300.

[120] Umar Khan et al. "Solvent-exfoliated graphene at extremely high concentration". In: *Langmuir* 27.15 (2011), pp. 9077–9082.

[121] Zheling Li et al. "Mechanisms of liquid-phase exfoliation for the production of graphene". In: *ACS nano* 14.9 (2020), pp. 10976–10985.

[122] Claudia Backes et al. "Production of highly monolayer enriched dispersions of liquid-exfoliated nanosheets by liquid cascade centrifugation". In: *ACS nano* 10.1 (2016), pp. 1589–1601.

[123] J Marguerite Hughes, Damian Aherne, and Jonathan N Coleman. "Generalizing solubility parameter theory to apply to one-and two-dimensional solutes and to incorporate dipolar interactions". In: *Journal of Applied Polymer Science* 127.6 (2013), pp. 4483–4491.

[124] Joel Henry Hildebrand, John M Prausnitz, and Robert Lane Scott. *Regular and related solutions: the solubility of gases, liquids, and solids*. Van Nostrand Reinhold Company, 1970.

[125] Michael Rubinstein, Ralph H Colby, et al. *Polymer physics*. Vol. 23. Oxford university press New York, 2003.

[126] Beth A Miller-Chou and Jack L Koenig. "A review of polymer dissolution". In: *Progress in Polymer Science* 28.8 (2003), pp. 1223–1270.

[127] Yenny Hernandez et al. "Measurement of multicomponent solubility parameters for graphene facilitates solvent discovery". In: *Langmuir* 26.5 (2010), pp. 3208–3213.

[128] Jonathan N Coleman et al. "Two-dimensional nanosheets produced by liquid exfoliation of layered materials". In: *Science* 331.6017 (2011), pp. 568–571.

[129] Andrea Capasso et al. "Ink-jet printing of graphene for flexible electronics: an environmentally-friendly approach". In: *Solid State Communications* 224 (2015), pp. 53–63.

[130] William M Haynes. *CRC handbook of chemistry and physics*. CRC press, 2014.

[131] Francesco Bonaccorso et al. "2D-crystal-based functional inks". In: *Advanced Materials* 28.29 (2016), pp. 6136–6166.

[132] Jianfeng Shen et al. "Liquid phase exfoliation of two-dimensional materials by directly probing and matching surface tension components". In: *Nano letters* 15.8 (2015), pp. 5449–5454.

[133] Yenny Hernandez et al. "High-yield production of graphene by liquid-phase exfoliation of graphite". In: *Nature nanotechnology* 3.9 (2008), pp. 563–568.

[134] Kai-Ge Zhou et al. "A mixed-solvent strategy for efficient exfoliation of inorganic graphene analogues". In: *Angewandte Chemie* 123.46 (2011), pp. 11031–11034.

[135] Udayabagya Halim et al. "A rational design of cosolvent exfoliation of layered materials by directly probing liquid–solid interaction". In: *Nature communications* 4.1 (2013), pp. 1–7.

[136] Francesco Bonaccorso and Zhipei Sun. "Solution processing of graphene, topological insulators and other 2d crystals for ultrafast photonics". In: *Optical Materials Express* 4.1 (2014), pp. 63–78.

[137] Ibrahim Sadek Khattab et al. "Density, viscosity, and surface tension of water+ ethanol mixtures from 293 to 323K". In: *Korean Journal of Chemical Engineering* 29.6 (2012), pp. 812–817.

[138] Xiaoyan Zhang et al. "Dispersion of graphene in ethanol using a simple solvent exchange method". In: *Chemical Communications* 46.40 (2010), pp. 7539–7541.

[139] Win Wenseleers et al. "Efficient isolation and solubilization of pristine single-walled nanotubes in bile salt micelles". In: *Advanced Functional Materials* 14.11 (2004), pp. 1105–1112.

[140] F Bonaccorso et al. "Density gradient ultracentrifugation of nanotubes: Interplay of bundling and surfactants encapsulation". In: *The Journal of Physical Chemistry C* 114.41 (2010), pp. 17267–17285.

[141] David W Johnson, Ben P Dobson, and Karl S Coleman. "A manufacturing perspective on graphene dispersions". In: *Current Opinion in Colloid & Interface Science* 20.5-6 (2015), pp. 367–382.

[142] Robert J Hunter. *Zeta potential in colloid science: principles and applications*. Vol. 2. Academic press, 2013.

[143] GH Findenegg. *JN Israelachvili: Intermolecular and Surface Forces (With Applications to Colloidal and Biological Systems). Academic Press, London, Orlando, San Diego, New York, Toronto, Montreal, Sydney, Tokyo 1985. 296 Seiten, Preis:* 65.00.. 1986.

[144] Jin-Yong Hong et al. "Omnidirectionally stretchable and transparent graphene electrodes". In: *Acs Nano* 10.10 (2016), pp. 9446–9455.

[145] Khushboo Agarwal et al. "Nanoscale thermoelectric properties of Bi2Te3–Graphene nanocomposites: Conducting atomic force, scanning thermal and kelvin probe microscopy studies". In: *Journal of Alloys and Compounds* 681 (2016), pp. 394–401.

[146] Tiina Vuorinen et al. "Inkjet-printed graphene/PEDOT: PSS temperature sensors on a skin-conformable polyurethane substrate". In: *Scientific reports* 6.1 (2016), pp. 1–8.

[147] Tatsuo Sato et al. "Stabilization of colloidal dispersions by polymer adsorption". In: (1980).

[148] Peter May et al. "Role of solubility parameters in understanding the steric stabilization of exfoliated two-dimensional nanosheets by adsorbed polymers". In: *The Journal of Physical Chemistry C* 116.20 (2012), pp. 11393–11400.

[149] Tawfique Hasan et al. "Nanotube–polymer composites for ultrafast photonics". In: *Advanced materials* 21.38-39 (2009), pp. 3874–3899.

[150] Andrea C Ferrari et al. "Science and technology roadmap for graphene, related two-dimensional crystals, and hybrid systems". In: *Nanoscale* 7.11 (2015), pp. 4598–4810.

[151] Victor Vega-Mayoral et al. "Photoluminescence from liquid-exfoliated WS2 monomers in poly (vinyl alcohol) polymer composites". In: *Advanced Functional Materials* 26.7 (2016), pp. 1028–1039.

[152] Theodor Svedberg, Kai Oluf Pedersen, et al. "The ultracentrifuge." In: *The Ultracentrifuge.* (1940).

[153] Ernest W Flick. *Printing ink and overprint varnish formulations*. William Andrew, 1999.

[154] P Beecher et al. "Ink-jet printing of carbon nanotube thin film transistors". In: *Journal of Applied Physics* 102.4 (2007), p. 043710.

[155] Marek Trojanowicz. "Analytical applications of carbon nanotubes: a review". In: *TrAC trends in analytical chemistry* 25.5 (2006), pp. 480–489.

[156] Tiago Almeida Silva et al. "Electrochemical biosensors based on nanostructured carbon black: A review". In: *Journal of Nanomaterials* 2017 (2017).

[157] Z Bao. "Y, Feng, A. Dodabalapur, VR Raju". In: *AJ Lovinger, Chem. Mater* 9 (1997), p. 1299.

[158] Woo Jin Hyun et al. "Screen printing of highly loaded silver inks on plastic substrates using silicon stencils". In: *ACS applied materials & interfaces* 7.23 (2015), pp. 12619–12624.

[159] Dino A Pardo, Ghassan E Jabbour, and Nasser Peyghambarian. "Application of screen printing in the fabrication of organic light-emitting devices". In: *Advanced Materials* 12.17 (2000), pp. 1249–1252.

[160] Michel Andre Aegerter and Martin Mennig. *Sol-gel technologies for glass producers and users*. Springer Science & Business Media, 2013.

[161] D Argent et al. "Flexography: Principles & Practices". In: *Foundation of Flexograpic* (1999).

[162] Se Hyun Ahn and L Jay Guo. "High-speed roll-to-roll nanoimprint lithography on flexible plastic substrates". In: *Advanced materials* 20.11 (2008), pp. 2044–2049.

[163] Arne Schleunitz et al. "Hybrid working stamps for high speed roll-to-roll nanoreplication with molded sol–gel relief on a metal backbone". In: *Microelectronic engineering* 88.8 (2011), pp. 2113–2116.

[164] Tapio Mäkelä et al. "Continuous roll to roll nanoimprinting of inherently conducting polyaniline". In: *Microelectronic engineering* 84.5-8 (2007), pp. 877–879.

[165] Richard Zallen and Michael Slade. "Rigid-layer modes in chalcogenide crystals". In: *Physical Review B* 9.4 (1974), p. 1627.

[166] Pierre L Fauchais, Joachim VR Heberlein, and Maher I Boulos. "Overview of thermal spray". In: *Thermal spray fundamentals*. Springer, 2014, pp. 17–72.

[167] Brian Derby and Nuno Reis. "Inkjet printing of highly loaded particulate suspensions". In: *MRS bulletin* 28.11 (2003), pp. 815–818.

[168] B-J De Gans, Paul C Duineveld, and Ulrich S Schubert. "Inkjet printing of polymers: state of the art and future developments". In: *Advanced materials* 16.3 (2004), pp. 203–213.

[169] Ethan B Secor. "Principles of aerosol jet printing". In: *Flexible and Printed Electronics* 3.3 (2018), p. 035002.

[170] Ankit Mahajan, C Daniel Frisbie, and Lorraine F Francis. "Optimization of aerosol jet printing for high-resolution, high-aspect ratio silver lines". In: *ACS applied materials & interfaces* 5.11 (2013), pp. 4856–4864.

[171] NJ Wilkinson et al. "A review of aerosol jet printing—a non-traditional hybrid process for micro-manufacturing". In: *The International Journal of Advanced Manufacturing Technology* 105.11 (2019), pp. 4599–4619.

[172] Yashaswi Nalawade et al. "All-Printed Dielectric Capacitors from High-Permittivity, Liquid-Exfoliated BiOCl Nanosheets". In: *ACS Applied Electronic Materials* 2.10 (2020), pp. 3233–3241.

[173] Felice Torrisi et al. "Inkjet-printed graphene electronics". In: *ACS nano* 6.4 (2012), pp. 2992–3006.

[174] Shuai Wang et al. "High mobility, printable, and solution-processed graphene electronics". In: *Nano letters* 10.1 (2010), pp. 92–98.

[175] Norman A Luechinger, Evagelos K Athanassiou, and Wendelin J Stark. "Graphene-stabilized copper nanoparticles as an air-stable substitute for silver and gold in low-cost ink-jet printable electronics". In: *Nanotechnology* 19.44 (2008), p. 445201.

[176] YH Yoon et al. "JH Y, HY Lee Sci". In: *Rep* 5 (2015), p. 14177.

[177] Chien-Liang Lee, Chih-Hao Chen, and Chin-Wei Chen. "Graphene nanosheets as ink particles for inkjet printing on flexible board". In: *Chemical engineering journal* 230 (2013), pp. 296–302.

[178] Jiantong Li et al. "Inkjet printing of MoS2". In: *Advanced Functional Materials* 24.41 (2014), pp. 6524–6531.

[179] David J Finn et al. "Inkjet deposition of liquid-exfoliated graphene and MoS 2 nanosheets for printed device applications". In: *Journal of Materials Chemistry C* 2.5 (2014), pp. 925–932.

[180] Daryl McManus et al. "Water-based and biocompatible 2D crystal inks for all-inkjet-printed heterostructures". In: *Nature nanotechnology* 12.4 (2017), pp. 343–350.

[181] Guohua Hu et al. "Black phosphorus ink formulation for inkjet printing of optoelectronics and photonics". In: *Nature communications* 8.1 (2017), pp. 1–10.

[182] Robert Leach. *The printing ink manual*. Springer Science & Business Media, 2012.

[183] Artur Goldschmidt and Hans-Joachim Streitberger. "Basics of coating technology". In: *Vincentz: Hannover, Germany* (2007).

[184] Arthur A Tracton. *Coatings technology handbook*. CRC press, 2005.

[185] Ian M Hutchings and Graham D Martin. *Inkjet technology for digital fabrication*. John Wiley & Sons, 2012.

[186] Hugo Lievens. "Wide web coating of complex materials". In: *Surface and Coatings Technology* 76 (1995), pp. 744–753.

[187] Tony Smith. "Flexographic inks". In: *Pigment & Resin Technology* (1986).

[188] Ulrich Bröckel, Willi Meier, and Gerhard Wagner. *Product design and engineering: formulation of gels and pastes*. John Wiley & Sons, 2013.

[189] Paul C Hiemenz and Raj Rajagopalan. *Principles of Colloid and Surface Chemistry, revised and expanded*. CRC press, 2016.

[190] Vineet Dua et al. "All-organic vapor sensor using inkjet-printed reduced graphene oxide". In: *Angewandte Chemie International Edition* 49.12 (2010), pp. 2154–2157.

[191] HC Burstyn, JV Sengers, and P Esfandiari. "Stokes-Einstein diffusion of critical fluctuations in a fluid". In: *Physical Review A* 22.1 (1980), p. 282.

[192] S Mueller, EW Llewellin, and HM Mader. "The rheology of suspensions of solid particles". In: *Proceedings of the Royal Society A: Mathematical, Physical and Engineering Sciences* 466.2116 (2010), pp. 1201–1228.

[193] D Quemada. "Rheology of concentrated disperse systems and minimum energy dissipation principle". In: *Rheologica Acta* 16.1 (1977), pp. 82–94.

[194] SR Williams and AP Philipse. "Random packings of spheres and spherocylinders simulated by mechanical contraction". In: *Physical Review E* 67.5 (2003), p. 051301.

[195] Mingle Gan et al. "Predicting packing characteristics of particles of arbitrary shapes". In: *KONA Powder and Particle Journal* 22 (2004), pp. 82–93.

[196] Aleksandar Donev et al. "Improving the density of jammed disordered packings using ellipsoids". In: *Science* 303.5660 (2004), pp. 990–993.

[197] Elena V Timofeeva, Jules L Routbort, and Dileep Singh. "Particle shape effects on thermophysical properties of alumina nanofluids". In: *Journal of applied physics* 106.1 (2009), p. 014304.

[198] J Garg et al. "Enhanced thermal conductivity and viscosity of copper nanoparticles in ethylene glycol nanofluid". In: *Journal of Applied Physics* 103.7 (2008), p. 074301.

[199] IM Mahbubul, Rahman Saidur, and MA Amalina. "Latest developments on the viscosity of nanofluids". In: *International Journal of Heat and Mass Transfer* 55.4 (2012), pp. 874–885.

[200] Purna Chandra Mishra et al. "A brief review on viscosity of nanofluids". In: *International nano letters* 4.4 (2014), pp. 109–120.

[201] A Ya Malkin, AI Isayev, et al. "Concepts, Methods and Applications". In: *Applied Rheology* 16.5 (2006).

[202] Jungho Park and Jooho Moon. "Control of colloidal particle deposit patterns within picoliter droplets ejected by ink-jet printing". In: *Langmuir* 22.8 (2006), pp. 3506–3513.

[203] Richard CT Howe et al. "Functional inks of graphene, metal dichalcogenides and black phosphorus for photonics and (opto) electronics". In: *Low-Dimensional Materials and Devices*. Vol. 9553. International Society for Optics and Photonics. 2015, 95530R.

[204] Jayoung Kim et al. "Advanced materials for printed wearable electrochemical devices: A review". In: *Advanced Electronic Materials* 3.1 (2017), p. 1600260.

[205] Ethan B Secor et al. "Combustion-assisted photonic annealing of printable graphene inks via exothermic binders". In: *ACS applied materials & interfaces* 9.35 (2017), pp. 29418–29423.

[206] Ethan B Secor et al. "Enhanced conductivity, adhesion, and environmental stability of printed graphene inks with nitrocellulose". In: *Chemistry of Materials* 29.5 (2017), pp. 2332–2340.

[207] Line Kyhl et al. "Graphene as an anti-corrosion coating layer". In: *Faraday discussions* 180 (2015), pp. 495–509.

[208] Yuan-Hsiang Yu et al. "High-performance polystyrene/graphene-based nanocomposites with excellent anti-corrosion properties". In: *Polymer Chemistry* 5.2 (2014), pp. 535–550.

[209] Xiaoyu Sui et al. "Additive manufacturing and applications of nanomaterial-based sensors". In: *Materials Today* (2021).

[210] Joanna Izdebska-Podsiadly and Sabu Thomas. *Printing on polymers: fundamentals and applications*. William Andrew, 2015.

[211] Osman Simseker, Batuhan Kurt, and Emine Arman. "Effects of different solvents to printability in gravure printing". In: *Asian Journal of Chemistry* 24.11 (2012), pp. 5253–5256.

[212] Barna Szabo. "Applications for Printing Inks". In: *Polymer dispersions and their industrial applications* 5 (2002), p. 180.

[213] Xiao-Fei Zhang et al. "Dielectric evaluation of electrically tunable Ba0. 6Sr0. 4TiO3 thick films prepared by screen printing". In: *Ceramics International* 38.4 (2012), pp. 3465–3472.

[214] José Restolho, José L Mata, and Benilde Saramago. "On the interfacial behavior of ionic liquids: Surface tensions and contact angles". In: *Journal of colloid and interface science* 340.1 (2009), pp. 82–86.

[215] FB Sprow and JM Prausnitz. "Surface tensions of simple liquids". In: *Transactions of the Faraday Society* 62 (1966), pp. 1097–1104.

[216] Pavel Diviš et al. "Determination of tin, chromium, cadmium and lead in canned fruits from the czech market". In: *Potravinarstvo Slovak Journal of Food Sciences* 11.1 (2017), pp. 564–570.

[217] S Santra et al. "CMOS integration of inkjet-printed graphene for humidity sensing". In: *Scientific reports* 5.1 (2015), pp. 1–12.

[218] David Dodoo-Arhin et al. "Inkjet-printed graphene electrodes for dye-sensitized solar cells". In: *Carbon* 105 (2016), pp. 33–41.

[219] Robert D Deegan et al. "Capillary flow as the cause of ring stains from dried liquid drops". In: *Nature* 389.6653 (1997), pp. 827–829.

[220] Guohua Hu et al. "A general ink formulation of 2D crystals for wafer-scale inkjet printing". In: *Science advances* 6.33 (2020), eaba5029.

[221] Haruya Okimoto et al. "Tunable carbon nanotube thin-film transistors produced exclusively via inkjet printing". In: *Advanced materials* 22.36 (2010), pp. 3981–3986.

[222] Katsuaki Suganuma. *Introduction to printed electronics*. Vol. 74. Springer Science & Business Media, 2014.

[223] Tian Carey et al. "Fully inkjet-printed two-dimensional material field-effect heterojunctions for wearable and textile electronics". In: *Nature communications* 8.1 (2017), pp. 1–11.

[224] H Rupprecht, R Rikkola, and I Hernberg. "Research, development and commercialisation highlights in Printed Intelligence: 2011-2012". In: *VTT Technical Research Centre of Finland* (2012).

[225] K Xerxes Steirer et al. "Ultrasonic spray deposition for production of organic solar cells". In: *Solar Energy Materials and Solar Cells* 93.4 (2009), pp. 447–453.

[226] Yifan Zheng et al. "Spray-coated nanoscale conductive patterns based on in situ sintered silver nanoparticle inks". In: *Nanoscale research letters* 9.1 (2014), pp. 1–7.

[227] Xinge Yu et al. "Flexible spray-coated TIPS-pentacene organic thin-film transistors as ammonia gas sensors". In: *Journal of Materials Chemistry C* 1.40 (2013), pp. 6532–6535.

[228] Anthony P Taylor and Luis F Velásquez-Garcıa. "Electrospray-printed nanostructured graphene oxide gas sensors". In: *Nanotechnology* 26.50 (2015), p. 505301.

[229] Chuen-Ming Gee et al. "Flexible transparent electrodes made of electrochemically exfoliated graphene sheets from low-cost graphite pieces". In: *Displays* 34.4 (2013), pp. 315–319.

[230] Stephen W Morton et al. "Scalable manufacture of built-to-order nanomedicine: spray-assisted layer-by-layer functionalization of PRINT nanoparticles". In: *Advanced Materials* 25.34 (2013), pp. 4707–4713.

[231] Rogério Gaspar and Ruth Duncan. "Polymeric carriers: preclinical safety and the regulatory implications for design and development of polymer therapeutics". In: *Advanced drug delivery reviews* 61.13 (2009), pp. 1220–1231.

[232] Ruth Duncan and Rogerio Gaspar. "Nanomedicine (s) under the microscope". In: *Molecular pharmaceutics* 8.6 (2011), pp. 2101–2141.

[233] Simone Casaluci et al. "Graphene-based large area dye-sensitized solar cell modules". In: *Nanoscale* 8.9 (2016), pp. 5368–5378.

[234] Samanta Witomska et al. "Article type:((Review))". In: ().

[235] Jack W Owen et al. "Effect of processing parameters on performance of spray-deposited organic thin-film transistors". In: *Journal of Nanotechnology* 2011 (2011).

[236] J Edward Glass et al. "Technology for waterborne coatings". In: (1997).

[237] G Perfetti et al. "Relation between surface roughness of free films and process parameters in spray coating". In: *European Journal of Pharmaceutical Sciences* 42.3 (2011), pp. 262–272.

[238] Sanjukta Bose et al. "Process optimization of ultrasonic spray coating of polymer films". In: *Langmuir* 29.23 (2013), pp. 6911–6919.

[239] Byung-Kwan Yu et al. "Factors to be considered in bulk heterojunction polymer solar cells fabricated by the spray process". In: *IEEE Journal of Selected Topics in Quantum Electronics* 16.6 (2010), pp. 1838–1846.

[240] GR Chegini and B Ghobadian. "Effect of spray-drying conditions on physical properties of orange juice powder". In: *Drying technology* 23.3 (2005), pp. 657–668.

[241] Christian Goth, Sonja Putzo, and Joerg Franke. "Aerosol Jet printing on rapid prototyping materials for fine pitch electronic applications". In: *2011 IEEE 61st electronic components and technology conference (ECTC)*. IEEE. 2011, pp. 1211–1216.

[242] Tobias Seifert et al. "Additive manufacturing technologies compared: morphology of deposits of silver ink using inkjet and aerosol jet printing". In: *Industrial & Engineering Chemistry Research* 54.2 (2015), pp. 769–779.

[243] Jeevan Manikyarao Meruga et al. "Red-green-blue printing using luminescence-upconversion inks". In: *Journal of Materials Chemistry C* 2.12 (2014), pp. 2221–2227.

[244] Se Hyun Kim et al. "Performance and stability of aerosol-jet-printed electrolyte-gated transistors based on poly (3-hexylthiophene)". In: *ACS applied materials & interfaces* 5.14 (2013), pp. 6580–6585.

[245] Ethan B Secor and Mark C Hersam. "Emerging carbon and post-carbon nanomaterial inks for printed electronics". In: *The journal of physical chemistry letters* 6.4 (2015), pp. 620–626.

[246] Kotaro Obata et al. "Hybrid Micro-stereo-lithography by Means of Aerosol Jet Printing Technology". In: *Journal of Laser Micro Nanoengineering* 9.3 (2014), p. 242.

[247] Kotaro Obata et al. "Hybrid 2D patterning using UV laser direct writing and aerosol jet printing of UV curable polydimethylsiloxane". In: *Applied Physics Letters* 111.12 (2017), p. 121903.

[248] Mohammad Sadeq Saleh, Chunshan Hu, and Rahul Panat. "Three-dimensional microarchitected materials and devices using nanoparticle assembly by pointwise spatial printing". In: *Science advances* 3.3 (2017), e1601986.

[249] Jason A Paulsen et al. "Printing conformal electronics on 3D structures with Aerosol Jet technology". In: *2012 Future of Instrumentation International Workshop (FIIW) Proceedings*. IEEE. 2012, pp. 1–4.

[250] Michael Maher, Adrien Smith, and Jesse Margiotta. "A synopsis of the Defense Advanced Research Projects Agency (DARPA) investment in additive manufacture and what challenges remain". In: *Laser 3D Manufacturing*. Vol. 8970. International Society for Optics and Photonics. 2014, p. 897002.

[251] Gregory J Marquez, Michael J Renn, and W Doyle Miller. "Aerosol-based direct-write of biological materials for biomedical applications". In: *MRS Online Proceedings Library (OPL)* 698 (2001).

[252] Roozbeh Salary et al. "A Sparse Representation Classification Approach for Near Real-Time, Physics-Based Functional Monitoring of Aerosol Jet-Fabricated Electronics". In: *Journal of Manufacturing Science and Engineering* 142.8 (2020), p. 081007.

[253] Yuan Gu et al. "Inkwells for on-demand deposition rate measurement in aerosol-jet based 3D printing". In: *Journal of Micromechanics and Microengineering* 27.9 (2017), p. 097001.

[254] James Q Feng and Michael J Renn. "Aerosol jet® direct-write for microscale additive manufacturing". In: *Journal of Micro and Nano-Manufacturing* 7.1 (2019).

[255] Justin M Hoey et al. "A review on aerosol-based direct-write and its applications for microelectronics". In: *Journal of Nanotechnology* 2012 (2012).

[256] IS Akhatov et al. "Aerosol focusing in micro-capillaries: Theory and experiment". In: *Journal of aerosol science* 39.8 (2008), pp. 691–709.

[257] S Binder. "GlatthaarMand Rädlein E 2014". In: *Aerosol Sci. Technol.* 48 (), p. 924.

[258] Michael Smith et al. "Controlling and assessing the quality of aerosol jet printed features for large area and flexible electronics". In: *Flexible and Printed Electronics* 2.1 (2017), p. 015004.

[259] Robert J Lang. "Ultrasonic atomization of liquids". In: *The journal of the acoustical society of America* 34.1 (1962), pp. 6–8.

[260] Richard L Peskin and Roland J Raco. "Ultrasonic atomization of liquids". In: *The Journal of the Acoustical Society of America* 35.9 (1963), pp. 1378–1381.

[261] Qijin Huang and Yong Zhu. "Printing conductive nanomaterials for flexible and stretchable electronics: A review of materials, processes, and applications". In: *Advanced Materials Technologies* 4.5 (2019), p. 1800546.

[262] TC Pluym et al. "Solid silver particle production by spray pyrolysis". In: *Journal of aerosol science* 24.3 (1993), pp. 383–392.

[263] Matthew A Tarr, Guangxuan Zhu, and Richard F Browner. "Fundamental aerosol studies with an ultrasonic nebulizer". In: *Applied spectroscopy* 45.9 (1991), pp. 1424–1432.

[264] Thomas D Donnelly et al. "Using ultrasonic atomization to produce an aerosol of micron-scale particles". In: *Review of scientific instruments* 76.11 (2005), p. 113301.

[265] Ethan B Secor. "Guided ink and process design for aerosol jet printing based on annular drying effects". In: *Flexible and Printed Electronics* 3.3 (2018), p. 035007.

[266] E Periasamy Ravindran and James Davis. "Multicomponent evaporation of single aerosol droplets". In: *Journal of Colloid and Interface Science* 85.1 (1982), pp. 278–288.

[267] JF Widmann and EJ Davis. "Evaporation of multicomponent droplets". In: *Aerosol science and technology* 27.2 (1997), pp. 243–254.

[268] Bryce A Williams et al. "Copper–Zinc–Tin–Sulfide Thin Films via Annealing of Ultrasonic Spray Deposited Nanocrystal Coatings". In: *ACS applied materials & interfaces* 9.22 (2017), pp. 18865–18871.

[269] Pradeep Lall et al. "Process Development for Additive Fabrication of Z-Axis Interconnects In Multilayer Circuits". In: *2020 19th IEEE Intersociety Conference on Thermal and Thermomechanical Phenomena in Electronic Systems (ITherm)*. IEEE. 2020, pp. 796–804.

[270] Sebastian Binder, Markus Glatthaar, and Edda Rädlein. "Analytical investigation of aerosol jet printing". In: *Aerosol Science and Technology* 48.9 (2014), pp. 924–929.

[271] Paul J Ziemann, David B Kittelson, and Peter H McMurry. "Effects of particle shape and chemical composition on the electron impact charging properties of submicron inorganic particles". In: *Journal of aerosol science* 27.4 (1996), pp. 587–606.

[272] L Jay Deiner and Thomas L Reitz. "Inkjet and aerosol jet printing of electrochemical devices for energy conversion and storage". In: *Advanced Engineering Materials* 19.7 (2017), p. 1600878.

[273] Qing Cao et al. "Medium-scale carbon nanotube thin-film integrated circuits on flexible plastic substrates". In: *Nature* 454.7203 (2008), pp. 495–500.

[274] Th Birendra Singh and Niyazi Serdar Sariciftci. "Progress in plastic electronics devices". In: *Annu. Rev. Mater. Res.* 36 (2006), pp. 199–230.

[275] JohnáA Rogers, HowardáE Katz, et al. "Printable organic and polymeric semiconducting materials and devices". In: *Journal of Materials Chemistry* 9.9 (1999), pp. 1895–1904.

[276] HENNING Sirringhaus et al. "High-resolution inkjet printing of all-polymer transistor circuits". In: *Science* 290.5499 (2000), pp. 2123–2126.

[277] Andre K Geim and Irina V Grigorieva. "Van der Waals heterostructures". In: *Nature* 499.7459 (2013), pp. 419–425.

[278] Bettina V Lotsch. "Vertical 2D heterostructures". In: *Annual Review of Materials Research* 45 (2015), pp. 85–109.

[279] Deep Jariwala, Tobin J Marks, and Mark C Hersam. "Mixed-dimensional van der Waals heterostructures". In: *Nature materials* 16.2 (2017), pp. 170–181.

[280] SM Sze and Kwok K Ng. "Physics of Semiconductor Devices. Hoboken, New Jersey: John Wiley & Sons". In: *Inc.–2007* (2006).

[281] Youngki Yoon, Kartik Ganapathi, and Sayeef Salahuddin. "How good can monolayer MoS2 transistors be?" In: *Nano letters* 11.9 (2011), pp. 3768–3773.

[282] Gianluca Fiori et al. "Electronics based on two-dimensional materials". In: *Nature nanotechnology* 9.10 (2014), pp. 768–779.

[283] Michele Buscema et al. "Photocurrent generation with two-dimensional van der Waals semiconductors". In: *Chemical Society Reviews* 44.11 (2015), pp. 3691–3718.

[284] Tejas A Shastry et al. "Mutual photoluminescence quenching and photovoltaic effect in large-area single-layer MoS2–polymer heterojunctions". In: *ACS nano* 10.11 (2016), pp. 10573–10579.

[285] Jinshui Miao et al. "Ultrashort channel length black phosphorus field-effect transistors". In: *ACS nano* 9.9 (2015), pp. 9236–9243.

[286] Shiheng Lu et al. "Flexible, print-in-place 1D–2D thin-film transistors using aerosol jet printing". In: *ACS nano* 13.10 (2019), pp. 11263–11272.

[287] Yang Wang et al. "Tunable capacitance in all-inkjet-printed nanosheet heterostructures". In: *Energy Storage Materials* 36 (2021), pp. 318–325.

[288] Panagiotis G Karagiannidis et al. "Microfluidization of graphite and formulation of graphene-based conductive inks". In: *ACS nano* 11.3 (2017), pp. 2742–2755.

[289] Kirill Arapov et al. "Conductive screen printing inks by gelation of graphene dispersions". In: *Advanced Functional Materials* 26.4 (2016), pp. 586–593.

[290] Quanhong Chang et al. "Water-Soluble Hybrid Graphene Ink for Gravure-Printed Planar Supercapacitors". In: *Advanced Electronic Materials* 4.8 (2018), p. 1800059.

[291] Sebastian Barwich et al. "On the relationship between morphology and conductivity in nanosheet networks". In: *Carbon* 171 (2021), pp. 306–319.

[292] Min Pack et al. "Colloidal drop deposition on porous substrates: competition among particle motion, evaporation, and infiltration". In: *Langmuir* 31.29 (2015), pp. 7953–7961.

[293] Zhaoyang Lin et al. "Solution-processable 2D semiconductors for high-performance large-area electronics". In: *Nature* 562.7726 (2018), pp. 254–258.

[294] Graeme Cunningham et al. "Large variations in both dark-and photoconductivity in nanosheet networks as nanomaterial is varied from MoS 2 to WTe 2". In: *Nanoscale* 7.1 (2015), pp. 198–208.

[295] Yanfei Xu et al. "Screen-printable thin film supercapacitor device utilizing graphene/polyaniline inks". In: *Advanced Energy Materials* 3.8 (2013), pp. 1035–1040.

[296] Ting Leng et al. "Graphene nanoflakes printed flexible meandered-line dipole antenna on paper substrate for low-cost RFID and sensing applications". In: *IEEE Antennas and Wireless Propagation Letters* 15 (2016), pp. 1565–1568.

[297] Bin Shen, Wentao Zhai, and Wenge Zheng. "Ultrathin flexible graphene film: an excellent thermal conducting material with efficient EMI shielding". In: *Advanced Functional Materials* 24.28 (2014), pp. 4542–4548.

[298] Sowmya Sankaran et al. "Recent advances in electromagnetic interference shielding properties of metal and carbon filler reinforced flexible polymer composites: a review". In: *Composites Part A: Applied Science and Manufacturing* 114 (2018), pp. 49–71.

[299] Guijun Li et al. "3D printed graphene/nickel electrodes for high areal capacitance electrochemical storage". In: *Journal of Materials Chemistry A* 7.8 (2019), pp. 4055–4062.

[300] Matthew H Ervin, Linh T Le, and Woo Y Lee. "Inkjet-printed flexible graphene-based supercapacitor". In: *Electrochimica Acta* 147 (2014), pp. 610–616.

[301] Ke Xu et al. "Nanomaterial-based gas sensors: A review". In: *Instrumentation Science & Technology* 46.2 (2018), pp. 115–145.

[302] Jiantong Li et al. "Efficient inkjet printing of graphene". In: *Advanced materials* 25.29 (2013), pp. 3985–3992.

[303] Junyeong Yun et al. "Stretchable patterned graphene gas sensor driven by integrated micro-supercapacitor array". In: *Nano Energy* 19 (2016), pp. 401–414.

[304] Yotsarayuth Seekaew and Chatchawal Wongchoosuk. "A novel graphene-based electroluminescent gas sensor for carbon dioxide detection". In: *Applied Surface Science* 479 (2019), pp. 525–531.

[305] Prinjaporn Teengam et al. "Electrochemical paper-based peptide nucleic acid biosensor for detecting human papillomavirus". In: *Analytica chimica acta* 952 (2017), pp. 32–40.

[306] Georgia-Paraskevi Nikoleli et al. "Structural characterization of graphene nanosheets for miniaturization of potentiometric urea lipid film based biosensors". In: *Electroanalysis* 24.6 (2012), pp. 1285–1295.

[307] Ying Wang et al. "Nitrogen-doped graphene and its application in electrochemical biosensing". In: *ACS nano* 4.4 (2010), pp. 1790–1798.

[308] Mitra Akbari et al. "Fabrication and characterization of graphene antenna for low-cost and environmentally friendly RFID tags". In: *IEEE Antennas and Wireless Propagation Letters* 15 (2015), pp. 1569–1572.

[309] D Marchand et al. "Surface structure and electrical conductivity of natural and artificial graphites". In: *Carbon* 22.6 (1984), pp. 497–506.

[310] Yijin Zhang et al. "Ambipolar MoS2 thin flake transistors". In: *Nano letters* 12.3 (2012), pp. 1136–1140.

[311] Elahe Jabari and Ehsan Toyserkani. "Micro-scale aerosol-jet printing of graphene interconnects". In: *Carbon* 91 (2015), pp. 321–329.

[312] Matilde Eredia et al. "Morphology and electronic properties of electrochemically exfoliated graphene". In: *The journal of physical chemistry letters* 8.14 (2017), pp. 3347–3355.

[313] Xiaona Xia et al. "Aligning graphene sheets in PDMS for improving output performance of triboelectric nanogenerator". In: *Carbon* 111 (2017), pp. 569–576.

[314] Twinkle Pandhi et al. "Electrical transport and power dissipation in aerosol-jet-printed graphene interconnects". In: *Scientific reports* 8.1 (2018), pp. 1–10.

[315] Khaled Parvez et al. "Water-based and inkjet printable inks made by electrochemically exfoliated graphene". In: *Carbon* 149 (2019), pp. 213–221.

[316] Kewen Pan et al. "Sustainable production of highly conductive multilayer graphene ink for wireless connectivity and IoT applications". In: *Nature communications* 9.1 (2018), pp. 1–10.

[317] Kirill Arapov, Robert Abbel, Heiner Friedrich, et al. "Inkjet printing of graphene". In: *Faraday discussions* 173 (2014), pp. 323–336.

[318] Xiuyi Lin et al. "Fabrication of highly-aligned, conductive, and strong graphene papers using ultralarge graphene oxide sheets". In: *ACS nano* 6.12 (2012), pp. 10708–10719.

[319] Goki Eda, Giovanni Fanchini, and Manish Chhowalla. "Large-area ultrathin films of reduced graphene oxide as a transparent and flexible electronic material". In: *Nature nanotechnology* 3.5 (2008), pp. 270–274.

[320] Matthew J Large et al. "Large-Scale Surfactant Exfoliation of Graphene and Conductivity-Optimized Graphite Enabling Wireless Connectivity". In: *Advanced Materials Technologies* 5.7 (2020), p. 2000284.

[321] Yuki Kuwahara et al. "Length dependent performance of single-wall carbon nanotube thin film transistors". In: *Carbon* 91 (2015), pp. 370–377.

[322] Gabriele Calabrese et al. "Inkjet-printed graphene Hall mobility measurements and low-frequency noise characterization". In: *Nanoscale* 12.12 (2020), pp. 6708–6716.

[323] Sukanta De and Jonathan N Coleman. "Are there fundamental limitations on the sheet resistance and transmittance of thin graphene films?" In: *ACS nano* 4.5 (2010), pp. 2713–2720.

[324] HSJ Bratschitsch. "van der Zant, and A. Castellanos-Gomez". In: *Nano Letters* 14 (2014).

[325] Richard Zallen. *The physics of amorphous solids*. John Wiley & Sons, 2008.

[326] Shanshan Liu et al. "Improved properties of barium strontium titanate thin films grown on copper foils by pulsed laser deposition using a self-buffered layer". In: *Journal of Physics D: Applied Physics* 45.17 (2012), p. 175304.

[327] Yoshihiko Imanaka. "Decoupling capacitor with low inductance for high-frequency digital applications". In: *Fujitsu Sci. Tech. J.* 38.1 (2002), pp. 22–30.

[328] Rong-Fuh Louh and Yu-Hsiu Hsu. "Fabrication of barium titanate ferroelectric layers by electrophoretic deposition technique". In: *Materials chemistry and physics* 79.2-3 (2003), pp. 226–229.

[329] Yoshihiko Imanaka, Hideyuki Amada, and Fumiaki Kumasaka. "Dielectric and insulating properties of embedded capacitor for flexible electronics prepared by aerosol-type nanoparticle deposition". In: *Japanese Journal of Applied Physics* 52.5S1 (2013), 05DA02.

[330] Minoru Osada et al. "High-κ dielectric nanofilms fabricated from titania nanosheets". In: *Advanced Materials* 18.8 (2006), pp. 1023–1027.

[331] Ana CM de Moraes et al. "Ion-Conductive, Viscosity-Tunable Hexagonal Boron Nitride Nanosheet Inks". In: *Advanced Functional Materials* 29.39 (2019), p. 1902245.

[332] Xiaoxi Zhu et al. "Hexagonal Boron Nitride–Enhanced Optically Transparent Polymer Dielectric Inks for Printable Electronics". In: *Advanced functional materials* 30.31 (2020), p. 2002339.

[333] Bikesh Gupta and HSS Ramakrishna Matte. "Solution-Processed Layered Hexagonal Boron Nitride Dielectrics: A Route toward Fabrication of High Performance Flexible Devices". In: *ACS Applied Electronic Materials* 1.10 (2019), pp. 2130–2139.

[334] Hua Hu and Ronald G Larson. "Marangoni effect reverses coffee-ring depositions". In: *The Journal of Physical Chemistry B* 110.14 (2006), pp. 7090–7094.

[335] X Shen. "Ho., C.-M.; Wong, T.-S". In: *J. Phys. Chem. B* 114.16 (2010), pp. 5269–5274.

[336] Saad A Hasan et al. "Electrophoretic deposition of CdSe nanocrystal films onto dielectric polymer thin films". In: *Thin Solid Films* 517.8 (2009), pp. 2665–2669.

[337] Katsuhiko Ariga et al. "Forming nanomaterials as layered functional structures toward materials nanoarchitectonics". In: *NPG Asia Materials* 4.5 (2012), e17–e17.

[338] Yonggang Huang, J Wu, and Keh-Chih Hwang. "Thickness of graphene and single-wall carbon nanotubes". In: *Physical review B* 74.24 (2006), p. 245413.

[339] Qiang Lu, Marino Arroyo, and Rui Huang. "Elastic bending modulus of monolayer graphene". In: *Journal of Physics D: Applied Physics* 42.10 (2009), p. 102002.

[340] D-B Zhang, E Akatyeva, and T Dumitrică. "Bending ultrathin graphene at the margins of continuum mechanics". In: *Physical review letters* 106.25 (2011), p. 255503.

[341] Claudia Backes et al. "Equipartition of energy defines the size–thickness relationship in liquid-exfoliated nanosheets". In: *ACS nano* 13.6 (2019), pp. 7050–7061.

[342] Pei He et al. "Screen-printing of a highly conductive graphene ink for flexible printed electronics". In: *ACS applied materials & interfaces* 11.35 (2019), pp. 32225–32234.

[343] Xianjun Huang et al. "Binder-free highly conductive graphene laminate for low cost printed radio frequency applications". In: *Applied Physics Letters* 106.20 (2015), p. 203105.

[344] Sarah-Jane Potts et al. "Effect of photonic flash annealing with subsequent compression rolling on the topography, microstructure and electrical performance of carbon-based inks". In: *Journal of Materials Science* 54.11 (2019), pp. 8163–8176.

[345] Pei-Yan Zhai et al. "Calendering of free-standing electrode for lithium-sulfur batteries with high volumetric energy density". In: *Carbon* 111 (2017), pp. 493–501.

[346] Peng Luo et al. "Doping engineering and functionalization of two-dimensional metal chalcogenides". In: *Nanoscale Horizons* 4.1 (2019), pp. 26–51.

[347] Dong-Ho Kang et al. "High-performance transition metal dichalcogenide photodetectors enhanced by self-assembled monolayer doping". In: *Advanced Functional Materials* 25.27 (2015), pp. 4219–4227.

[348] Joseph Halim et al. "Variable range hopping and thermally activated transport in molybdenum-based MXenes". In: *Physical Review B* 98.10 (2018), p. 104202.

[349] Owen C Compton and SonBinh T Nguyen. "Graphene oxide, highly reduced graphene oxide, and graphene: versatile building blocks for carbon-based materials". In: *small* 6.6 (2010), pp. 711–723.

[350] Kirill Arapov et al. "Graphene screen-printed radio-frequency identification devices on flexible substrates". In: *physica status solidi (RRL)–Rapid Research Letters* 10.11 (2016), pp. 812–818.

[351] Taneli Juntunen et al. "Inkjet printed large-area flexible few-layer graphene thermoelectrics". In: *Advanced Functional Materials* 28.22 (2018), p. 1800480.

[352] Geoffrey William Arnold Dummer. *Electronic inventions and discoveries*. Elsevier, 1978.

[353] I Bernard Cohen. "Dictionary of Scientific Biography, Vol. 11". In: *New York: Charles Scribner's Sons* (1970), p. 43.

[354] Vadim F Lvovich. *Impedance spectroscopy: applications to electrochemical and dielectric phenomena*. John Wiley & Sons, 2012.

[355] Ali Javey et al. "High-κ dielectrics for advanced carbon-nanotube transistors and logic gates". In: *Nature materials* 1.4 (2002), pp. 241–246.

[356] SJ Wind et al. "Vertical scaling of carbon nanotube field-effect transistors using top gate electrodes". In: *Applied Physics Letters* 80.20 (2002), pp. 3817–3819.

[357] Geoff L Brennecka et al. "Processing technologies for high-permittivity thin films in capacitor applications". In: *Journal of the American Ceramic Society* 93.12 (2010), pp. 3935–3954.

[358] Yanfeng Gao, Yoshitake Masuda, and Kunihito Koumoto. "Light-excited superhydrophilicity of amorphous TiO2 thin films deposited in an aqueous peroxotitanate solution". In: *Langmuir* 20.8 (2004), pp. 3188–3194.

[359] Lei Liao et al. "High-κ oxide nanoribbons as gate dielectrics for high mobility top-gated graphene transistors". In: *Proceedings of the national academy of sciences* 107.15 (2010), pp. 6711–6715.

[360] Yoshitaka Aoki, Toyoki Kunitake, and Aiko Nakao. "Sol- gel fabrication of dielectric HfO2 nano-films; formation of uniform, void-free layers and their superior electrical properties". In: *Chemistry of materials* 17.2 (2005), pp. 450–458.

[361] D Dimos and CH Mueller. "Perovskite thin films for high-frequency capacitor applications". In: *Annual Review of Materials Science* 28.1 (1998), pp. 397–419.

[362] SR Summerfelt et al. "Demonstration of scaled (0.12 μ m 2) Pb (Zr, Ti) O 3 capacitors on W plugs with Al interconnect". In: *Applied physics letters* 79.24 (2001), pp. 4004–4006.

[363] Orlando Auciello, James F Scott, Ramamoorthy Ramesh, et al. "The physics of ferroelectric memories". In: *Physics today* 51.7 (1998), pp. 22–27.

[364] Angus I Kingon, Jon-Paul Maria, and SK Streiffer. "Alternative dielectrics to silicon dioxide for memory and logic devices". In: *Nature* 406.6799 (2000), pp. 1032–1038.

[365] Seungbeom Choi et al. "High-mobility inkjet-printed indium-gallium-zinc-oxide thin-film transistors using sr-doped Al2O3 gate dielectric". In: *Materials* 12.6 (2019), p. 852.

[366] Sung-Gap Lee, Chang-Il Kim, and Byung-Chul Kim. "Dielectric properties of screen-printed (Ba, Sr, Ca) TiO3 thick films modified with Al2O3 for microwave device applications". In: *Journal of the European Ceramic Society* 24.1 (2004), pp. 157–162.

[367] G Vescio et al. "Inkjet printed HfO 2-based ReRAMs: First demonstration and performance characterization". In: *IEEE Electron Device Letters* 38.4 (2017), pp. 457–460.

[368] BS Richards. "Comparison of TiO2 and other dielectric coatings for buried-contact solar cells: a review". In: *Progress in photovoltaics: research and applications* 12.4 (2004), pp. 253–281.

[369] Carl W Wilmsen. "Oxide/III-V compound semiconductor interfaces". In: *Physics and Chemistry of III-V Compound Semiconductor Interfaces*. Springer, 1985, pp. 403–462.

[370] Marius D Stamate. "Dielectric properties of TiO2 thin films deposited by a DC magnetron sputtering system". In: *Thin Solid Films* 372.1-2 (2000), pp. 246–249.

[371] Bongki Lee et al. "Conformal Al 2 O 3 dielectric layer deposited by atomic layer deposition for graphene-based nanoelectronics". In: *Applied Physics Letters* 92.20 (2008), p. 203102.

[372] Xinran Wang, Scott M Tabakman, and Hongjie Dai. "Atomic layer deposition of metal oxides on pristine and functionalized graphene". In: *Journal of the American Chemical Society* 130.26 (2008), pp. 8152–8153.

[373] HM Wang et al. "Electronic transport and layer engineering in multilayer graphene structures". In: *Applied Physics Letters* 92.5 (2008), p. 053504.

[374] Max C Lemme et al. "A graphene field-effect device". In: *IEEE Electron Device Letters* 28.4 (2007), pp. 282–284.

[375] Jon-Paul Maria et al. "Lead zirconate titanate thin films on base-metal foils: an approach for embedded high-permittivity passive components". In: *Journal of the American Ceramic Society* 84.10 (2001), pp. 2436–2438.

[376] U Balachandran et al. "Development of PLZT dielectrics on base metal foils for embedded capacitors". In: *Journal of the European Ceramic Society* 30.2 (2010), pp. 365–368.

[377] DK Das-Gupta and K Doughty. "Polymer-ceramic composite materials with high dielectric constants". In: *Thin Solid Films* 158.1 (1988), pp. 93–105.

[378] Shengxia Li et al. "Cross-linked polymer-blend gate dielectrics through thermal click chemistry". In: *Chemistry–A European Journal* 21.49 (2015), pp. 17762–17768.

[379] Jong-Myung Won et al. "Photo-patternable polyimide gate insulator with fluorine groups for improving performance of 2, 7-didecyl [1] benzothieno [3, 2-b][1] benzothiopene (C10-BTBT) thin-film transistors". In: *Organic Electronics* 14.7 (2013), pp. 1777–1786.

[380] Jagan Singh Meena et al. "Novel chemical route to prepare a new polymer blend gate dielectric for flexible low-voltage organic thin-film transistor". In: *ACS applied materials & interfaces* 4.6 (2012), pp. 3261–3269.

[381] Lei Zhu. "Exploring strategies for high dielectric constant and low loss polymer dielectrics". In: *The journal of physical chemistry letters* 5.21 (2014), pp. 3677–3687.

[382] James E Mark et al. *Physical properties of polymers handbook*. Vol. 1076. Springer, 2007.

[383] Zhongbo Zhang et al. "High-κ polymers of intrinsic microporosity: a new class of high temperature and low loss dielectrics for printed electronics". In: *Materials Horizons* 7.2 (2020), pp. 592–597.

[384] Yi Li et al. "An all-inkjet printed flexible capacitor on a textile using a new poly (4-vinylphenol) dielectric ink for wearable applications". In: *SENSORS, 2012 IEEE*. IEEE. 2012, pp. 1–4.

[385] Benjamin S Cook, James R Cooper, and Manos M Tentzeris. "Multi-layer RF capacitors on flexible substrates utilizing inkjet printed dielectric polymers". In: *IEEE Microwave and Wireless Components Letters* 23.7 (2013), pp. 353–355.

[386] Qin Chen et al. "Polymer-based dielectrics with high energy storage density". In: *Annual review of materials research* 45 (2015), pp. 433–458.

[387] Henning Sirringhaus. "Reliability of organic field-effect transistors". In: *Advanced Materials* 21.38-39 (2009), pp. 3859–3873.

[388] Jinhua Li, Zhenhua Sun, and Feng Yan. "Solution processable low-voltage organic thin film transistors with high-k relaxor ferroelectric polymer as gate insulator". In: *Advanced Materials* 24.1 (2012), pp. 88–93.

[389] Ana Claudia Arias et al. "Materials and applications for large area electronics: solution-based approaches". In: *Chemical reviews* 110.1 (2010), pp. 3–24.

[390] Jinhua Li et al. "Solution-processable organic and hybrid gate dielectrics for printed electronics". In: *Materials Science and Engineering: R: Reports* 127 (2018), pp. 1–36.

[391] Liam Britnell et al. "Electron tunneling through ultrathin boron nitride crystalline barriers". In: *Nano letters* 12.3 (2012), pp. 1707–1710.

[392] Lei Wang et al. "One-dimensional electrical contact to a two-dimensional material". In: *Science* 342.6158 (2013), pp. 614–617.

[393] Freddie Withers et al. "Light-emitting diodes by band-structure engineering in van der Waals heterostructures". In: *Nature materials* 14.3 (2015), pp. 301–306.

[394] Felice Torrisi and Tian Carey. "Graphene, related two-dimensional crystals and hybrid systems for printed and wearable electronics". In: *Nano Today* 23 (2018), pp. 73–96.

[395] Yifei Wang et al. "High-temperature dielectric polymer nanocomposites with interposed montmorillonite nanosheets". In: *Chemical Engineering Journal* 401 (2020), p. 126093.

[396] Yuan Ma et al. "Montmorillonite/PVDF-HFP-based energy conversion and storage films with enhanced piezoelectric and dielectric properties". In: *Composites Science and Technology* 168 (2018), pp. 397–403.

[397] H Bidadi, PA Schroeder, and Thomas J Pinnavaia. "Dielectric properties of montmorillonite clay films: Effects of water and layer charge reduction". In: *Journal of Physics and Chemistry of Solids* 49.12 (1988), pp. 1435–1440.

[398] Bo Li et al. "Effect of crystal orientation and nanofiller alignment on dielectric breakdown of polyethylene/montmorillonite nanocomposites". In: *Applied Physics Letters* 111.8 (2017), p. 082906.

[399] Davoud Dastan and Arun Banpurkar. "Solution processable sol–gel derived titania gate dielectric for organic field effect transistors". In: *Journal of Materials Science: Materials in Electronics* 28.4 (2017), pp. 3851–3859.

[400] Saira Ishaq et al. "Dielectric and impedance spectroscopic studies of three phase graphene/titania/poly (vinyl alcohol) nanocomposite films". In: *Results in Physics* 11 (2018), pp. 540–548.

[401] Biplab K Roy et al. "Developments of Low-Temperature Solution Processing for Nanostructured Titania Dielectric Films". In: *Science of Advanced Materials* 2.1 (2010), pp. 90–101.

[402] Kosho Akatsuka et al. "Construction of highly ordered lamellar nanostructures through Langmuir- Blodgett deposition of molecularly thin titania nanosheets tens of micrometers wide and their excellent dielectric properties". In: *ACS nano* 3.5 (2009), pp. 1097–1106.

[403] Claudia Backes et al. "Edge and confinement effects allow in situ measurement of size and thickness of liquid-exfoliated nanosheets". In: *Nature communications* 5.1 (2014), pp. 1–10.

[404] Claudia Backes et al. "Spectroscopic metrics allow in situ measurement of mean size and thickness of liquid-exfoliated few-layer graphene nanosheets". In: *Nanoscale* 8.7 (2016), pp. 4311–4323.

[405] Zicheng Ding et al. "Patterning of pinhole free small molecular organic light-emitting films by ink-jet printing". In: *Organic Electronics* 12.4 (2011), pp. 703–709.

[406] Binghao Wang et al. "High-k gate dielectrics for emerging flexible and stretchable electronics". In: *Chemical reviews* 118.11 (2018), pp. 5690–5754.

[407] Mao-Hua Du and David J Singh. "Enhanced Born charges in III-VII, IV-VII 2, and V-VII 3 compounds". In: *Physical Review B* 82.4 (2010), p. 045203.

[408] Jiating Lu et al. "Electronic structures and lattice dynamics of layered BiOCl single crystals". In: *The journal of physical chemistry letters* 11.3 (2020), pp. 1038–1044.

[409] John B Boland et al. "Liquid phase exfoliation of MoO 2 nanosheets for lithium ion battery applications". In: *Nanoscale Advances* 1.4 (2019), pp. 1560–1570.

[410] John B Boland et al. "Liquid phase exfoliation of GeS nanosheets in ambient conditions for lithium ion battery applications". In: *2D Materials* 7.3 (2020), p. 035015.

[411] Andrew Harvey et al. "Non-resonant light scattering in dispersions of 2D nanosheets". In: *Nature communications* 9.1 (2018), pp. 1–11.

[412] Ling Zhang et al. "Solar-light-driven pure water splitting with ultrathin BiOCl nanosheets". In: *Chemistry–A European Journal* 21.50 (2015), pp. 18089–18094.

[413] Freskida Goni, Angela Chemelli, and Frank Uhlig. "High-Yield Production of Selected 2D Materials by Understanding Their Sonication-Assisted Liquid-Phase Exfoliation". In: *Nanomaterials* 11.12 (2021), p. 3253.

[414] Xianglu Yin et al. "Preparation of two-dimensional molybdenum disulfide nanosheets by high-gravity technology". In: *Industrial & Engineering Chemistry Research* 56.16 (2017), pp. 4736–4742.

[415] Sean P Ogilvie et al. "Considerations for spectroscopy of liquid-exfoliated 2D materials: emerging photoluminescence of N-methyl-2-pyrrolidone". In: *Scientific reports* 7.1 (2017), pp. 1–7.

[416] Yoon Myung et al. "Electrical conductivity of p-type BiOCl nanosheets". In: *Chemical Communications* 51.13 (2015), pp. 2629–2632.

[417] Sujuan Wu et al. "Surface reorganization leads to enhanced photocatalytic activity in defective BiOCl". In: *Chemistry of Materials* 30.15 (2018), pp. 5128–5136.

[418] Siyu Qiang et al. "Wearable solid-state capacitors based on two-dimensional material all-textile heterostructures". In: *Nanoscale* 11.20 (2019), pp. 9912–9919.

[419] Matthew P Garrett et al. "Separation of junction and bundle resistance in single wall carbon nanotube percolation networks by impedance spectroscopy". In: *Applied Physics Letters* 97.16 (2010), p. 163105.

[420] Li-Mo Wang. "Relationship between intrinsic breakdown field and bandgap of materials". In: *2006 25th International Conference on Microelectronics*. IEEE. 2006, pp. 576–579.

[421] Jonathan N Coleman, Umar Khan, and Yurii K Gun'ko. "Mechanical reinforcement of polymers using carbon nanotubes". In: *Advanced materials* 18.6 (2006), pp. 689–706.

[422] Ye Hou et al. "Functionalized few-walled carbon nanotubes for mechanical reinforcement of polymeric composites". In: *ACS nano* 3.5 (2009), pp. 1057–1062.

[423] Yan Wang, ZiXing Shi, and Jie Yin. "Unzipped multiwalled carbon nanotubes for mechanical reinforcement of polymer composites". In: *The Journal of Physical Chemistry C* 114.46 (2010), pp. 19621–19628.

[424] Metal-Filled Polymers—Properties. *Applications; Bhattacharya, S. K, Ed*. 1986.

[425] Shoko Yoshikawa et al. "Piezoresistivity in Polymer-Ceramic Composites". In: *Journal of the American Ceramic Society* 73.2 (1990), pp. 263–267.

[426] D Stauffer and A Aharony. "Introduction to Percolation Theory. London: Taylor & Francis". In: (1992).

[427] Ce-Wen Nan. "Physics of inhomogeneous inorganic materials". In: *Progress in materials science* 37.1 (1993), pp. 1–116.

[428] Andriy V Kyrylyuk et al. "Controlling electrical percolation in multicomponent carbon nanotube dispersions". In: *Nature nanotechnology* 6.6 (2011), pp. 364–369.

[429] C-W Nan, Yang Shen, and Jing Ma. "Physical properties of composites near percolation". In: *Annual Review of Materials Research* 40 (2010), pp. 131–151.

[430] Vishal Singh, AR Kulkarni, and TR Rama Mohan. "Dielectric properties of aluminum–epoxy composites". In: *Journal of applied polymer science* 90.13 (2003), pp. 3602–3608.

[431] Biao Zhao et al. "A versatile foaming platform to fabricate polymer/carbon composites with high dielectric permittivity and ultra-low dielectric loss". In: *Journal of Materials Chemistry A* 7.1 (2019), pp. 133–140.

[432] Zhi-Min Dang et al. "Fundamentals, processes and applications of high-permittivity polymer–matrix composites". In: *Progress in materials science* 57.4 (2012), pp. 660–723.

[433] B Vigolo et al. "An experimental approach to the percolation of sticky nanotubes". In: *Science* 309.5736 (2005), pp. 920–923.

[434] AL Efros and Boris I Shklovskii. "Critical behaviour of conductivity and dielectric constant near the metal-non-metal transition threshold". In: *Physica status solidi (b)* 76.2 (1976), pp. 475–485.

[435] Haiwei Du et al. "Colossal permittivity in percolative ceramic/metal dielectric composites". In: *Journal of Alloys and Compounds* 663 (2016), pp. 848–861.

[436] Jinkai Yuan et al. "Graphene liquid crystal retarded percolation for new high-k materials". In: *Nature communications* 6.1 (2015), pp. 1–8.

[437] Alan Luna et al. "Giant permittivity polymer nanocomposites obtained by curing a direct emulsion". In: *Langmuir* 31.44 (2015), pp. 12231–12239.

[438] Hari Singh Nalwa. *Handbook of low and high dielectric constant materials and their applications, two-volume set*. Elsevier, 1999.

[439] Tetsuya Osaka and Madhav Datta. *Energy storage systems in electronics*. CRC Press, 2000.

[440] Zhen Su et al. "Microstructural transitions and dielectric properties of boron-doped amorphous alumina thin film". In: *Journal of Materials Science* 52.16 (2017), pp. 9314–9323.

[441] Peter Barber et al. "Polymer composite and nanocomposite dielectric materials for pulse power energy storage". In: *Materials* 2.4 (2009), pp. 1697–1733.

[442] Graeme Cunningham et al. "Percolation scaling in composites of exfoliated MoS 2 filled with nanotubes and graphene". In: *Nanoscale* 4.20 (2012), pp. 6260–6264.

[443] Adam G Kelly et al. "Tuneable photoconductivity and mobility enhancement in printed MoS2/graphene composites". In: *2D Materials* 4.4 (2017), p. 041006.

[444] Cian Gabbett et al. "The effect of network formation on the mechanical properties of 1D: 2D nano: nano composites". In: *Chemistry of Materials* 30.15 (2018), pp. 5245–5255.

[445] Domhnall O'Suilleabhain et al. "Percolation effects in electrolytically gated WS2/graphene nano: nano composites". In: *ACS applied materials & interfaces* 11.8 (2019), pp. 8545–8555.

[446] Nen-Wen Pu et al. "Dispersion of graphene in aqueous solutions with different types of surfactants and the production of graphene films by spray or drop coating". In: *Journal of the Taiwan Institute of Chemical Engineers* 43.1 (2012), pp. 140–146.

[447] Mohammad Akbari Garakani et al. "Scalable spray-coated graphene-based electrodes for high-power electrochemical double-layer capacitors operating over a wide range of temperature". In: *Energy Storage Materials* 34 (2021), pp. 1–11.

[448] Viet Hung Pham et al. "Fast and simple fabrication of a large transparent chemically-converted graphene film by spray-coating". In: *Carbon* 48.7 (2010), pp. 1945–1951.

[449] Dietrich Stauffer and Ammon Aharony. *Introduction to percolation theory*. CRC press, 2018.

[450] Huan Pang et al. "An electrically conducting polymer/graphene composite with a very low percolation threshold". In: *Materials Letters* 64.20 (2010), pp. 2226–2229.

[451] Sasha Stankovich et al. "Graphene-based composite materials". In: *nature* 442.7100 (2006), pp. 282–286.

[452] D Stauffer and A Aharony. *Introduction to Percolation Theory. Taylor and Fransis*. 1985.

[453] Junjie Wu and DS McLachlan. "Percolation exponents and thresholds obtained from the nearly ideal continuum percolation system graphite-boron nitride". In: *Physical review B* 56.3 (1997), p. 1236.

[454] Qiang Zhang et al. "The road for nanomaterials industry: A review of carbon nanotube production, post-treatment, and bulk applications for composites and energy storage". In: *Small* 9.8 (2013), pp. 1237–1265.

[455] W Wang et al. "Effective reinforcement in carbon nanotube–polymer composites". In: *Philosophical Transactions of the Royal Society A: Mathematical, Physical and Engineering Sciences* 366.1870 (2008), pp. 1613–1626.

[456] Xiao Huang et al. "Graphene-based composites". In: *Chemical Society Reviews* 41.2 (2012), pp. 666–686.

[457] Robert J Young et al. "The mechanics of graphene nanocomposites: a review". In: *Composites Science and Technology* 72.12 (2012), pp. 1459–1476.

[458] Ronald HJ Otten and Paul van der Schoot. "Connectivity percolation of polydisperse anisotropic nanofillers". In: *The Journal of chemical physics* 134.9 (2011), p. 094902.

[459] David J Bergman and Yoseph Imry. "Critical behavior of the complex dielectric constant near the percolation threshold of a heterogeneous material". In: *Physical Review Letters* 39.19 (1977), p. 1222.

[460] Carlos Pecharroman et al. "New percolative BaTiO3–Ni composites with a high and frequency-independent dielectric constant (r 80000)". In: *Advanced Materials* 13.20 (2001), pp. 1541–1544.

[461] Carlos Pecharromán and José S Moya. "Experimental evidence of a giant capacitance in insulator–conductor composites at the percolation threshold". In: *Advanced Materials* 12.4 (2000), pp. 294–297.

[462] Z-M Dang, Y-H Lin, and C-W Nan. "Novel ferroelectric polymer composites with high dielectric constants". In: *Advanced Materials* 15.19 (2003), pp. 1625–1629.

[463] Z-M Dang, Y Shen, and C-W Nan. "Dielectric behavior of three-phase percolative Ni–BaTiO 3/polyvinylidene fluoride composites". In: *Applied Physics Letters* 81.25 (2002), pp. 4814–4816.

[464] Cheng Huang and Qiming Zhang. "Enhanced dielectric and electromechanical responses in high dielectric constant all-polymer percolative composites". In: *Advanced Functional Materials* 14.5 (2004), pp. 501–506.

[465] Qun Li et al. "Large dielectric constant of the chemically functionalized carbon nanotube/polymer composites". In: *Composites Science and Technology* 68.10-11 (2008), pp. 2290–2296.

[466] G Sui et al. "Dielectric properties and conductivity of carbon nanofiber/semicrystalline polymer composites". In: *Acta Materialia* 56.10 (2008), pp. 2381–2388.

[467] John B Goodenough, Héctor D Abruna, and Michelle V Buchanan. *Basic research needs for electrical energy storage. report of the basic energy sciences workshop on electrical energy storage, april 2-4, 2007*. Tech. rep. DOESC (USDOE Office of Science (SC)), 2007.

[468] Eli Harari. "Dielectric breakdown in electrically stressed thin films of thermal SiO2". In: *Journal of Applied Physics* 49.4 (1978), pp. 2478–2489.

[469] Greg C Stone et al. *Electrical insulation for rotating machines: design, evaluation, aging, testing, and repair*. Vol. 21. John Wiley & Sons, 2004.

[470] J Han and R Garrett. "Overview of polymer nanocomposites as dielectrics and electrical insulation materials for large high voltage rotating machines". In: *NSTI-Nanotech*. Vol. 2. 2008, pp. 727–732.

[471] Baojin Chu et al. "A dielectric polymer with high electric energy density and fast discharge speed". In: *Science* 313.5785 (2006), pp. 334–336.

[472] Ralph Taylor et al. "Development, Test and Demonstration of a Cost-Effective, Compact, Light-Weight, and Scalable High Temperature Inverter for HEVs, PHEVs, and FCVs". In: *2012 Annual Progress Report 2012* (2012).

[473] Rongmei Wen et al. "Nanocomposite capacitors with significantly enhanced energy density and breakdown strength utilizing a small loading of monolayer titania". In: *Advanced Materials Interfaces* 5.3 (2018), p. 1701088.

[474] Daniel Q Tan. "The search for enhanced dielectric strength of polymer-based dielectrics: a focused review on polymer nanocomposites". In: *Journal of Applied Polymer Science* 137.33 (2020), p. 49379.

[475] Zhengdong Wang et al. "Alignment of boron nitride nanofibers in epoxy composite films for thermal conductivity and dielectric breakdown strength improvement". In: *Nanomaterials* 8.4 (2018), p. 242.

[476] Jianwen Chen et al. "High dielectric constant and low dielectric loss poly (vinylidene fluoride) nanocomposites via a small loading of two-dimensional Bi 2 Te 3@ Al 2 O 3 hexagonal nanoplates". In: *Journal of Materials Chemistry C* 6.2 (2018), pp. 271–279.

[477] Xingyi Huang, Pingkai Jiang, and Toshikatsu Tanaka. "A review of dielectric polymer composites with high thermal conductivity". In: *IEEE Electrical Insulation Magazine* 27.4 (2011), pp. 8–16.

[478] Aideen Griffin et al. "Spectroscopic size and thickness metrics for liquid-exfoliated h-BN". In: *Chemistry of Materials* 30.6 (2018), pp. 1998–2005.

[479] Dan Yang et al. "Enhanced dielectric properties and actuated strain of elastomer composites with dopamine-induced surface functionalization". In: *Journal of Materials Chemistry A* 1.39 (2013), pp. 12276–12284.

[480] Xin Zhang et al. "Ultrahigh energy density of polymer nanocomposites containing BaTiO3@ TiO2 nanofibers by atomic-scale interface engineering". In: *Advanced materials* 27.5 (2015), pp. 819–824.

[481] TJ Lewis. "Nanometric dielectrics". In: *IEEE Transactions on Dielectrics and Electrical Insulation* 1.5 (1994), pp. 812–825.

[482] Mariem Samet et al. "Electrode polarization vs. Maxwell-Wagner-Sillars interfacial polarization in dielectric spectra of materials: Characteristic frequencies and scaling laws". In: *The Journal of chemical physics* 142.19 (2015), p. 194703.

[483] J Sune, M Nafria, and X Aymerich. "Reversible dielectric breakdown of thin gate oxides in MOS devices". In: *Microelectronics Reliability* 33.7 (1993), pp. 1031–1039.

[484] Dierk Bolten, U Böttger, and R Waser. "Reversible and irreversible polarization processes in ferroelectric ceramics and thin films". In: *Journal of applied physics* 93.3 (2003), pp. 1735–1742.

[485] Takane Usui et al. "Approaching the limits of dielectric breakdown for SiO2 films deposited by plasma-enhanced atomic layer deposition". In: *Acta materialia* 61.20 (2013), pp. 7660–7670.

[486] John J O'Dwyer. "Theory of dielectric breakdown in solids". In: *Journal of the Electrochemical Society* 116.2 (1969), p. 239.

[487] VK Agarwal and VK Srivastava. "Thickness dependence of breakdown field in thin films". In: *Thin solid films* 8.5 (1971), pp. 377–381.

[488] Qi Li et al. "Solution-processed ferroelectric terpolymer nanocomposites with high breakdown strength and energy density utilizing boron nitride nanosheets". In: *Energy & Environmental Science* 8.3 (2015), pp. 922–931.

[489] Frederick Seitz, Norman G Einspruch, and Norman G Einspruch. *Electronic genie: The tangled history of silicon*. University of Illinois Press, 1998.